

Synthesis and Density Functional Calculations of the New Molecule-Based Magnet Precursor $[\text{Fe}(\text{H}_2\text{opba-i})(\text{dmsO})_2]\text{Cl}$

Gilmar P. Souza,^a Cibele Konzen,^b José D. Ardisson,^b Heitor A. De Abreu,^a Hélió A. Duarte,^a
 Antônio F. C. Alcântara,^a Wallace C. Nunes,^c Waldemar A. A. Macedo,^b Marcelo Knobel^c
 and Humberto O. Stumpf^{*,a}

^aDepartamento de Química, ICEx, Universidade Federal de Minas Gerais,
 31270-901 Belo Horizonte – MG, Brazil

^bLaboratório de Física Aplicada, Centro de Desenvolvimento da Tecnologia Nuclear-CDTN, CP 941,
 30123-970 Belo Horizonte – MG, Brazil

^cInstituto de Física Gleb Wataghin, Universidade Estadual de Campinas, CP 6165,
 13083-970 Campinas – SP, Brazil

Um precursor inédito de sistemas magnéticos moleculares, $[\text{Fe}(\text{H}_2\text{opba-i})(\text{dmsO})_2]\text{Cl}$ (**1**), onde opba = *orto*-fenilenobis(oxamato) na forma tautomérica iminoálcool, foi obtido como produto da reação entre H_4opba e FeCl_3 . Os dados de análise elementar, espectroscopias de absorção no infravermelho e Mössbauer e medidas magnéticas indicam que este precursor é constituído por uma mistura de isômeros *trans* (83%) e *cis* (17%). O valor de $\chi_{\text{M}}T$ a 298 K (2,1 emu K mol⁻¹) corresponde ao Fe^{III} com estado de spin (S) entre 3/2 e 5/2. Cálculos teóricos (PBE/DZVP2) de *trans*- e *cis*- $[\text{Fe}(\text{H}_2\text{opba-i})(\text{dmsO})_2]^+$ mostram que ambos os isômeros têm spin S = 1/2 no estado fundamental e S = 3/2 para o *trans* e S = 5/2 para o *cis* no primeiro estado excitado. A combinação destes resultados leva a valores de $\chi_{\text{M}}T$ de 0,375 emu K mol⁻¹ e 2,3 emu K mol⁻¹ a baixas e altas temperaturas, respectivamente, os quais são concordantes com os dados experimentais para **1**.

A new precursor of molecule-based magnetic systems, $[\text{Fe}(\text{H}_2\text{opba-i})(\text{dmsO})_2]\text{Cl}$ (**1**), with opba = *ortho*-phenylenebis(oxamato) in an iminoalcohol tautomeric form, was obtained as a product from the reaction between H_4opba and FeCl_3 . Data from elemental analysis, IR and Mössbauer spectroscopies and magnetic measurements indicate that this precursor is composed of a mixture of *trans* (83%) and *cis* (17%) isomers. The $\chi_{\text{M}}T$ value at 298K (2.1 emu K mol⁻¹) corresponds to Fe^{III} with spin state (S) between 3/2 and 5/2. Theoretical calculations (PBE/DZVP2) of *trans*- and *cis*- $[\text{Fe}(\text{H}_2\text{opba-i})(\text{dmsO})_2]^+$ show that both isomers have spin S = 1/2 in the ground state and S = 3/2 for the *trans* and S = 5/2 for the *cis* in the first excited state. The combination of these results leads to $\chi_{\text{M}}T$ values of 0.375 and 2.3 emu K mol⁻¹, at low and high temperature respectively, which are in accordance with the experimental data for **1**.

Keywords: molecule-based magnet, oxamate, iron(III), PBE/DZVP theoretical calculations, *cis/trans* isomerism

Introduction

The oxamato-based ligands have an important role in molecular magnetism. In the seventies, the proligand 1,3-propylenebis(oxamato), pba, was synthesized, and some years later it was used in the preparation of molecule-based magnets.¹ In 1993, the new precursor $[\text{Bu}_4\text{N}]_2[\text{Cu}(\text{opba})]$,

opba = *ortho*-phenylenebis(oxamato), was synthesized and largely used as a building block, due to its high solubility in common organic solvents.²

The majority of the work done with oxamato-based building blocks is with Cu^{II}, most probably due to the stability of the compounds with this metal ion. Another reason for employing this metal ion resides on the ferrimagnetic strategy, which consists in the use of two metal ions with large difference in spin states and with

*e-mail: stumpf@dedalus.lcc.ufmg.br

antiferromagnetic coupling. In this approach, copper complexes can bridge several metal ions resulting in extended molecular systems (chains, two- and three-dimensional networks) and clusters.²⁻⁸ Such systems are recognized by their potential applications in recording/reading magnetic systems on the molecular scale.

The opba ligand has been used for stabilization of high oxidation states of transition metal ions such as Mn^{III} and Fe^{III} due to the high donor capacity of the deprotonated-amide group.⁹ Biomimetic systems such as the dimanganese(III) complex [PPh₄]₂[Mn₂(opba)₂(H₂O)₃].3H₂O.MeCN and the oxo-bridged diiron(III) complex [NEt₄]₄[Fe₂O(opba)₂].3H₂O are interesting models of biological catalytic oxidations.¹⁰⁻¹²

Unlike the usual *trans* geometry for the [Mⁿ(opba)]^(x-4) complexes, in which two deprotonated-amide nitrogen and two carboxylate oxygen atoms of the ligand form a plane, in 1997 an iron(III)-carbonate monomeric complex with a *cis*-β geometry was described. This compound, [NMe₄]₃[Fe(opba)(CO₃)]·5H₂O, has been shown to be a moderately efficient catalyst for the aerobic epoxidation of alkenes with co-oxidation of pivalaldehyde.¹³

There is no record in the literature on extended molecular systems or clusters built with precursors containing Fe^{III} and oxamato ligands. Furthermore, few examples of Fe^{III} compounds coordinated simultaneously by amide nitrogen atoms and carboxylate oxygen atoms of oxamato-based ligands have been reported.^{11,13} The present work reports the synthesis and characterization of a new Fe^{III} complex, [Fe(H₂opba-i)(dmsO)₂]Cl (**1**), with opba = *ortho*-phenylenebis(oxamato) in an iminoalcohol tautomeric form.

Experimental

The proligand H₄opba was prepared using an adaptation of a method described elsewhere.² All reagents were used as purchased without further purification. Elemental analyses (C, H, N) were performed on a 2400 CHN-Perkin Elmer instrument. Iron content was determined on a Z-8200 Hitachi atomic absorption spectrophotometer. Infrared spectra (IR) were recorded on a Perkin-Elmer Spectrum GX FTIR spectrophotometer, using KBr discs. Mössbauer spectra were measured in the transmission geometry on a constant-acceleration conventional spectrometer by using a ⁵⁷Co/Rh source and a closed cycle He cryostat. Mössbauer isomer shifts are quoted relatively to the α-Fe at room temperature. The magnetic measurements were performed with a Quantum Design SQUID MPMS XL7 instrument. The diamagnetic correction of the sample was calculated through the constants of Pascal's constants.¹⁴

Synthesis

A solution of FeCl₃·6H₂O (81.1 mg, 0.30 mmol) in DMSO (2 mL) was added to a solution of H₄opba (75.6 mg, 0.3 mmol) in DMSO (2 mL). The resulting mixture was stirred at 60 °C for 1 h and then allowed to stand at room temperature. A methanolic solution (10 mL) of KOH (50.5 mg, 0.9 mmol) was then added dropwise under stirring. The solid formed was dissolved in DMSO (8 mL) at 60 °C. The intensely brown colored solution was filtered and concentrated under reduced pressure to 4 mL. The brown precipitate was filtered off and washed with methanol. The product was dried under reduced pressure for 4 h (79.1 mg, yield: 53%). IR (KBr) ν_{max} /cm⁻¹: 3430(OH), 3127(C-H), 2900(CH₃, DMSO), 1695(amide I band), 1640(C=O), 1343(CH₃, DMSO), 1013(S=O, DMSO); Anal. Calc. for C₁₄H₁₈ClFeN₂O₈S₂ (MM = 497.73 g mol⁻¹): C, 33.8; H, 3.7; N, 5.6; Fe, 11.2%. Found: C, 33.2; H, 3.4; N, 5.8; Fe, 12.3%.

Theoretical calculations

All calculations were performed using the linear combination of Gaussian-type orbitals-Kohn-Sham density functional (LCGTO-KS-DFT) method implemented in the deMon program package.¹⁵ The exchange-correlation (XC) functional PBE was used to treat the systems; this XC functional uses the Perdew, Burke and Ernzerhof expression for exchange and correlation.¹⁶ We have used the DZVP basis set optimized explicitly for DFT by Godbout *et al.*¹⁷ Automatically generated auxiliary basis sets (A2) have been used for fitting the charge density. An adaptive grid with a tolerance of 10⁻⁶ for the numerical integration of the exchange-correlation and potential energy was used.^{18,19} All structures have been fully optimized without symmetry constraint using the standard Broyden-Fletcher-Goldfarb-Shanno (BFGS) method. Nonspecific solvent effects have been estimated using the united atoms Hartree-Fock/polarizable continuum model (UAHF/PCM).²⁰⁻²⁶ The solvation energies have been estimated using the Gaussian 98 program package.²⁷ As described by Saracino *et al.*²⁸ and Barone *et al.*,²⁹ we have used for all calculations the UAHF radii obtained by single point calculations at the HF/6-31G(d,p) level of theory using DFT optimized structures in gas phase. In the UAHF/PCM approach, the solute is placed in a polarizable cavity formed of spheres centered in the atomic groups. Inside the cavity, the dielectric constant is the same as in vacuum, and outside it takes the solvent value (ε = 46.7 for DMSO).

Results and Discussion

The elemental analysis data of the product from the reaction between H_4opba and ferric chloride in KOH solution corresponded to the formulation $[Fe(H_2opba-i)(dms)_2]Cl$. This complex presents deprotonation of both O-carboxylic atoms as in the similar reaction of H_4pba with KOH.³⁰ In the literature, there are several examples of deprotonation of both oxygen and nitrogen atoms of H_4opba with copper(II), nickel(II) and manganese(II), resulting in the respective $M^x(opba)^{(x-4)}$ compounds.³¹ In case of coordination with palladium(II), which affords the compound $Na[Pd(Hpba)] \cdot 2H_2O$, the deprotonation of two O-carboxylic and only one nitrogen atom of H_4pba has been observed.³⁰ In fact, the present work is the first synthesis description using H_4opba that has resulted in the formation of a complex of the type $M^x(H_2opba)^{(x-2)}$.

The IR data of **1** show intense absorptions at 1693 and 1640 cm^{-1} , that can be attributed to the amide I band of secondary amides and C=O of carboxylate groups, respectively.^{32,33} The frequency shifts in relation to the proligand (registered in 1775 and 1672 cm^{-1}) indicate the coordination of the two nitrogen and the two O-carboxylic atoms to the Fe^{III} .³⁴ The absorptions at 2913, 1013 and 1343 cm^{-1} (attributed to aliphatic C-H stretching, S=O stretching and methyl group vibrations, respectively) indicate the presence of DMSO molecules within the compound, as suggested by elemental analysis.

Figure 1 shows the ^{57}Fe Mössbauer spectrum of **1** at 70 K, least square fitted with two doublets (Lorentzian lines). One doublet (line 1, Figure 1) presents isomer shift $\delta_1 = 0.54(\pm 0.05)$ $mm\ s^{-1}$ and quadrupole splitting $\Delta_1 = 1.33(\pm 0.04)$ $mm\ s^{-1}$; the other doublet (line 2, Figure 1) presents isomer shift $\delta_2 = 0.52(\pm 0.05)$ $mm\ s^{-1}$ and quadrupole splitting $\Delta_2 = 0.66(\pm 0.04)$ $mm\ s^{-1}$. The obtained Mössbauer parameters indicate the existence of two Fe^{III} species within the product of the reaction, in similar chemical environments.^{35,36} The presence of iron oxide or hydroxide in the sample is ruled out. These parameters, in addition to the IR and elemental analysis results, suggest that Fe^{III} is in an octahedral geometry coordinated to the nitrogen and oxygen atoms of the ligand $H_2opba-i$. The other two coordination sites are filled with DMSO molecules. Indeed, the Mössbauer spectroscopy analysis indicates that the product of the reaction is composed of a mixture of two isomers.

According to the literature, Mössbauer spectra of octahedral complexes with *trans* isomers show quadrupole splittings twice as big as the ones given by complexes in the *cis* configuration.^{37,38} From these results, it can be proposed that the doublet 1 of Figure 1 ($\Delta_1 = 1.33$ mm

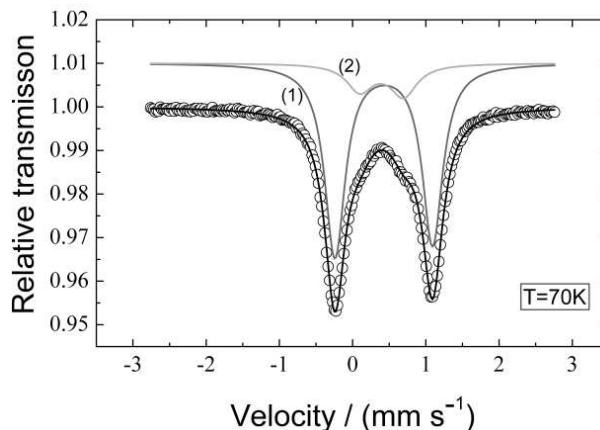


Figure 1. ^{57}Fe Mössbauer spectrum of **1** at 70 K. Doublets 1 (solid gray line, δ_1 , Δ_1) and 2 (light gray line, δ_2 , Δ_2) correspond to the best fits to the experimental data (see text).

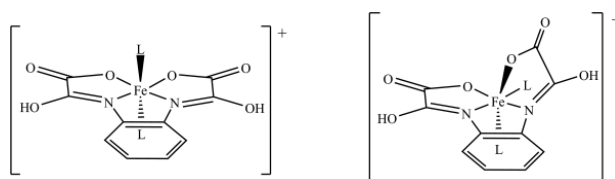


Figure 2. The *trans* and *cis* isomers of **1**.

s^{-1}) corresponds to the complex **1** in *trans* configuration, and the doublet 2 ($\Delta_2 = 0.66$ $mm\ s^{-1}$) corresponds to the same complex, but in *cis* configuration. Moreover, from the spectral areas, it can be proposed that the reaction product contains 83% of the *trans* and 17% of the *cis* isomers of **1** shown in Figure 2.

The magnetic properties of **1** have been investigated in the 2 - 300 K temperature range using a polycrystalline powder. The temperature dependence of the dc magnetic susceptibility is shown in Figure 3 with a $\chi_M T$ versus T plot, χ_M being the molar magnetic susceptibility (diamagnetic correction from Pascal's constants: $-80.0 \cdot 10^{-6}$ $emu\ mol^{-1}$). At room temperature $\chi_M T$ is equal to 2.1 $emu\ K\ mol^{-1}$. Using the *spin only* equation, which does not take into account either interactions among the spins or orbital contribution, the expected value of $\chi_M T$ for a Fe^{III} ion with a low spin state ($S = 1/2$), at room temperature, is equal to 0.375 $emu\ K\ mol^{-1}$.¹⁴ For the intermediate ($S = 3/2$) and high spin ($S = 5/2$) states, the values of $\chi_M T$ are equal to 1.875 and 4.375 $emu\ K\ mol^{-1}$, respectively. Even though the isomeric shift values obtained by Mössbauer spectroscopy do not allow the determination of the spin multiplicity of **1**, the experimental value of $\chi_M T$ suggests that this compound presents an Fe^{III} spin state intermediate between $S = 3/2$ and $S = 5/2$. $\chi_M T$ decreases slowly as T is lowered until 15 K, and then it decreases more rapidly as T is further

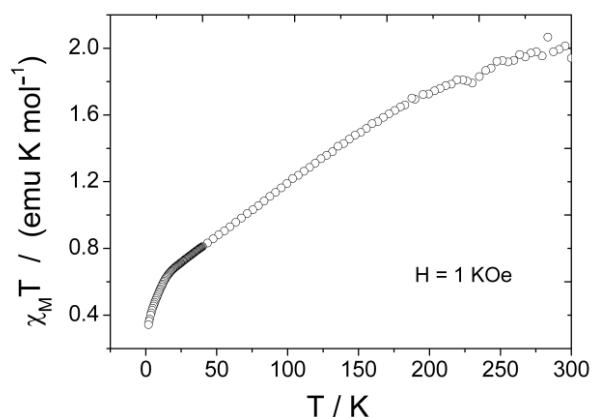


Figure 3. Temperature dependence of the product $\chi_M T$ versus temperature for **1**.

lowered, reaching $0.34 \text{ emu K mol}^{-1}$ at 2 K, the lowest available temperature. This value is approximately the one expected for a Fe^{III} ion in a state of spin $S = 1/2$. The slight difference in the $\chi_M T$ value and the slope change below 15 K can be explained by intermolecular antiferromagnetic interactions.

DFT calculations have been performed aiming to provide information about the electronic structure of the isomers of **1**. The functional PBE was employed since it has been successfully applied in describing transition metal systems, mainly Fe^{III} .^{39–41} Conformational analysis of the isolated H_4opba proligand was performed considering the two tautomers H_4opba (amide) and $\text{H}_4\text{opba-i}$ (iminoalcohol) shown in Figure 4. The H_4opba tautomer is about $31.4 \text{ kcal mol}^{-1}$ more stable than the $\text{H}_4\text{opba-i}$ tautomer according to the DFT results. The calculated C-2,C-1,N-1',C-2' and C-1,C-2,N-1'',C-2'' dihedral angles are 15.2 degrees in the H_4opba tautomer. However, these dihedral angles decrease by about 6.6 degrees with the deprotonation of the carboxylic groups leading to $\text{H}_2\text{opba}^{2-}$ species. This indicates larger electronic π -delocalization in the oxamate groups, as expected.

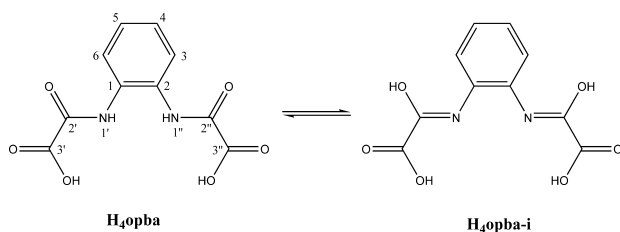


Figure 4. Amide-iminoalcohol tautomeric equilibrium involving H_4opba and $\text{H}_4\text{opba-i}$.

Figure 5 shows the optimized geometry for the $[\text{Fe}(\text{H}_2\text{opba-i})]^+$ complex, which presents the iminoalcohol tautomer as a ligand. The $[\text{Fe}(\text{H}_2\text{opba-i})]^+$ complex has C_{2v} symmetry with Fe-O and Fe-N bond distances of 1.831

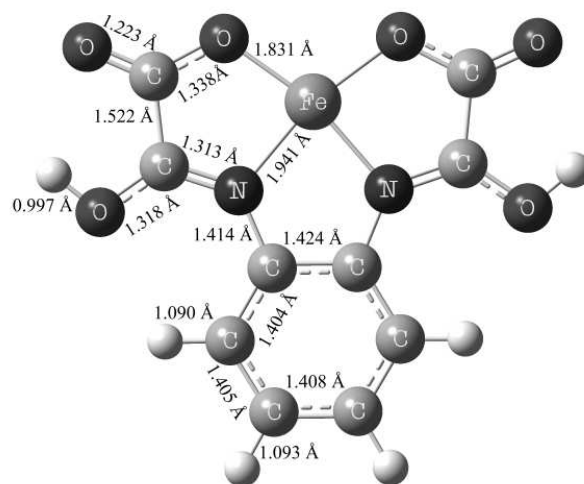


Figure 5. PBE/DZVP2 optimized geometry of $[\text{Fe}(\text{H}_2\text{opba-i})]^+$ in the gas phase.

and 1.941 Å with a quadratic planar arrangement around the iron center. Calculations showed that the amide tautomer was not a minimum in the potential energy surface, leading to the intramolecular hydrogen transfer to the O-amide. The occurrence of this type of transfer was also verified for similar systems such as $\text{Na}[\text{Pd}(\text{Hpba})]\cdot 2\text{H}_2\text{O}$ complex.³⁰

According to DFT results, the ground state of $[\text{Fe}(\text{H}_2\text{opba-i})]^+$ is a quartet ($S = 3/2$) and the doublet ($S = 1/2$) and sextet ($S = 5/2$) lie 17.1 and 15.0 kcal mol^{-1} higher in energy, respectively. These results indicate that the Fe^{III} ion coordinated to $\text{H}_2\text{opba-i}$ in the absence of dmso presents intermediary crystal-field strength with a ground state of $S = 3/2$.

The effect of the solvent can lead to important changes in the geometry and electronic structure of metal complexes. The DMSO molecules can coordinate to the vacant sites of the iron center in the $[\text{Fe}(\text{H}_2\text{opba-i})]^+$ to form an octahedral complex. Figure 6 shows the optimized geometries of the *cis*- $[\text{Fe}(\text{H}_2\text{opba-i})(\text{dmsO})_2]^+$ and *trans*- $[\text{Fe}(\text{H}_2\text{opba-i})(\text{dmsO})_2]^+$ isomers. The optimized geometry of *trans*- $[\text{Fe}(\text{H}_2\text{opba-i})(\text{dmsO})_2]^+$ shows an octahedral surrounding containing oxamate groups in equatorial positions and the oxygen atoms of two dmso molecules in apical positions. In the case of *cis*- $[\text{Fe}(\text{H}_2\text{opba-i})(\text{dmsO})_2]^+$, a distorted octahedral geometry with

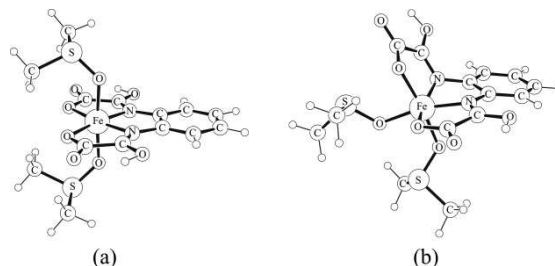


Figure 6. DFT optimized geometry for gas phase structures: (a) *trans*- $[\text{Fe}(\text{H}_2\text{opba-i})(\text{dmsO})_2]^+$ and (b) *cis*- $[\text{Fe}(\text{H}_2\text{opba-i})(\text{dmsO})_2]^+$.

the metal ion lying out of the $H_2opba-i$ plane is observed. A similar geometry was also described for the $[NMe_4]_3[Fe(opba)(CO_3)] \cdot 5H_2O$ complex.¹³ It is important to note that for these two species we have not performed vibrational frequency calculations due to difficulties caused by the size and complexity of the system.

For the optimized geometry of the *trans*- $[Fe(H_2opba-i)(dmsO)_2]^+$ configuration (Figure 6), the spin states $S = 1/2$, $3/2$, and $5/2$ were considered. The calculated ground state is the doublet ($S = 1/2$); the quartet ($S = 3/2$) and sextet ($S = 5/2$) states lie 7.5 and 10.7 kcal mol⁻¹ higher in energy, respectively. For *cis*- $[Fe(H_2opba-i)(dmsO)_2]^+$, the quartet ($S = 3/2$) and sextet ($S = 5/2$) lie 7.8 and 5.2 kcal mol⁻¹ higher in energy, respectively, showing inversion of the relative stability of the quartet and sextet states compared to *trans*- $[Fe(H_2opba-i)(dmsO)_2]^+$. These results are in accordance with the low temperature magnetic properties and $\chi_M T$ value of 0.34 emu K mol⁻¹, corresponding to a $S = 1/2$ ground state. The *cis*- $[Fe(H_2opba-i)(dmsO)_2]^+$ is the most stable and *trans*- $[Fe(H_2opba-i)(dmsO)_2]^+$ is about 5.7 kcal mol⁻¹ higher in energy.

One could argue that the magnetic property observed for this system is the average of the $\chi_M T$ of the two distinct complexes observed in the Mössbauer data. In order to test this hypothesis, it was assumed that, at room temperature, the low lying states $S = 3/2$ for *trans*- $[Fe(H_2opba-i)(dmsO)_2]^+$ (calculated $\chi_M T$ equal to 1.875 emu K mol⁻¹) and $S = 5/2$ for *cis*- $[Fe(H_2opba-i)(dmsO)_2]^+$ (calculated $\chi_M T$ equal to 4.375 emu K mol⁻¹) were populated. Combining these values with the Mössbauer data, which indicates an 83% occurrence of the *trans* isomer and 17% of the *cis* isomer, a $\chi_M T$ value can be proposed as a weighted average as follows: $\chi_M T = (0.83 \times 1.875 + 0.17 \times 4.375) = 2.3$ emu K mol⁻¹. This value decreases if it is admitted that the $S = 3/2$ state is also populated for the *cis* isomer. This value of the product $\chi_M T$ is close to that measured at room temperature for the compound **1**.

Conclusions

We have shown an efficient methodology for the preparation of a new precursor of a molecule-based magnet containing Fe^{III}, $[Fe(H_2opba)(dmsO)_2]Cl$ (**1**). The investigation of its physical and chemical properties was carried out by analysis of experimental data (elemental analysis, Mössbauer spectroscopy and magnetic susceptibility measurements) combined with results obtained by theoretical calculations. These results indicate that the reaction product presents a mixture of *trans* and *cis* isomers in relation to the two DMSO

molecules. DFT conformational analysis was performed on the proligand and the complex with iron(III), providing information about *cis/trans* isomerism, tautomerism, coordination site preference and spin states. The ground state found in the calculations for the two isomers was $S = 1/2$, in agreement with the magnetic properties at low temperatures. The calculations, Mössbauer and magnetic studies of **1** led to the interpretation of its magnetic properties based on a conversion of spin. Another natural hypothesis for the decreasing of $\chi_M T$ from the room temperature value is the establishment of antiferromagnetic interactions. However, this is less probable, since such interactions should be very strong at room temperature where a value of 4.375 emu K mol⁻¹ would be expected (considering $S = 5/2$). In the other extreme, we can suppose a spin state of $S = 1/2$ with orbital contribution for the magnetic moment and a vanishing of this later with the temperature, but in this case an overestimated orbital contribution should be adopted.

Finally, it is worth emphasizing that **1** is soluble in DMSO and DMF, which is an important property for reactions with other metal ions in the preparation of clusters or extended molecule-based magnets.

Acknowledgments

The authors would like to thank the support of Conselho Nacional de Desenvolvimento Científico e Tecnológico (CNPq), Coordenação de Aperfeiçoamento de Pessoal de Nível Superior (CAPES), Fundação de Amparo à Pesquisa do Estado de Minas Gerais (FAPEMIG) and Fundação de Amparo à Pesquisa do Estado de São Paulo (FAPESP).

References

1. Nonoyama, K.; Ojima, H.; Nonoyama, M.; *Inorg. Chim. Acta* **1976**, 20, 12.
2. Stumpf, H. O.; Pei, Y.; Kahn, O.; Sletten, J.; Renard, J. P.; *J. Am. Chem. Soc.* **1993**, 115, 6738.
3. Kahn, O.; Pei, Y.; Sletten, J.; *J. Am. Chem. Soc.* **1986**, 108, 3143.
4. Pereira, C. L. M.; Pedroso, E. F.; Stumpf, H. O.; Novak, M. A.; Ricard, L.; Ruiz-Garcia, R.; Riviere, E.; Journaux, Y.; *Angew. Chem., Int. Ed.* **2004**, 43, 956.
5. Vaz, M. G. F.; Knobel, M.; Speziali, N. L.; Moreira, A. M.; Alcântara, A. F. C.; Stumpf, H. O.; *J. Braz. Chem. Soc.* **2002**, 13, 183.
6. Cador, O.; Vaz, M. G. F.; Stumpf, H. O.; Mathonière, C.; Kahn, O.; *Synth. Met.* **2001**, 122, 559.

7. Sessoli, R.; Gatteschi, D.; Caneschi, A.; Novak, M. A.; *Nature* **1993**, 365, 141.
8. Pardo, E.; Morales-Osorio, I.; Julve, M.; Lloret, F.; Cano, J.; Ruiz-García, R.; Pasán, J.; Ruiz-Pérez, C.; Ottenwaelde, X.; Journaux, Y.; *Inorg. Chem.* **2004**, 43, 7594.
9. Ruiz, R.; Surville-Barland, C.; Aukauloo, A.; Anxolabehere-Mallart, E.; Journaux, Y.; Cano, J.; Muñoz, M. C.; *J. Chem. Soc., Dalton Trans.* **1997**, 745.
10. Blay, G.; Fernández, I.; Giménez, T.; Pedro, J. R.; Ruiz, R.; Pardo, E.; Lloret, F.; Muñoz, M. C.; *Chem. Commun.* **2001**, 2102.
11. Pardo, E.; Lloret, F.; Carrasco, R.; Muñoz, M. C.; Temporal-Sánchez, T.; Ruiz-García, R.; *Inorg. Chim. Acta* **2004**, 357, 2713.
12. Lippard, S. J.; *Angew. Chem., Int. Ed.* **1988**, 27, 344.
13. Ruiz, R.; Triannidis, M.; Aukauloo, A.; Journaux, Y.; Fernández, I.; Pedro, J. R.; Cervera, B.; Castro, I.; Muñoz, M. C.; *Chem. Commun.* **1997**, 2283.
14. Earnshaw, A.; *Introduction to Magnetochemistry*; Academic Press: New York, 1968.
15. Koester, A. M.; Flores, R.; Geudtner, G.; Goursot, A.; Heine, T.; Patchkovskii, A. M.; Reveles, J. U.; Vela, A.; Salahub, D.; *Program deMon*, version 1.1.0; NRC: Ottawa, Canada, 2004.
16. Perdew, J. P.; Burke, K.; Ernzerhof, M.; *Phys. Rev. Lett.* **1996**, 77, 3865.
17. Godbout, N.; Salahub, D. R.; Andzelm, J.; Wimmer, E.; *Can. J. Chem. Rev.* **1992**, 70, 560.
18. Krack, M.; Koster, A. M.; *J. Chem. Phys.* **1998**, 108, 3226.
19. Koster, A. M.; Flores-Moreno, R.; Reveles, J. U.; *J. Chem. Phys.* **2004**, 121, 681.
20. Fletcher, R.; *Comput. J.* **1970**, 13, 317.
21. Broyden, C. G.; *J. Inst. Math. Appl.* **1970**, 6, 76.
22. Goldfarb, D.; *Math. Comp.* **1970**, 24, 23.
23. Shanno, D. F.; *Math. Comp.* **1970**, 24, 647.
24. Broyden, C. G.; *J. Inst. Math. Appl.* **1970**, 6, 222.
25. Cossi, M.; Barone, V.; Cammi, R.; Tomasi, J.; *J. Chem. Phys. Lett.* **1996**, 255, 327.
26. Tomasi, J.; Persico, M.; *Chem. Rev.* **1994**, 94, 2027.
27. Frisch, M. J.; Trucks, G. W.; Schlegel, H. B.; Scuseria, G. E.; Robb, M. A.; Cheeseman, J. R.; Zakrzewski, V. G.; Montgomery, J.; Stratmann, R. E.; Burant, J. C.; Dapprich, S.; Millam, J. M.; Daniels, A. D.; Kudin, K. N.; Strain, M. C.; Farkar, O.; Tomasi, J.; Barone, V.; Cossi, M.; Cammi, R.; Mennucci, B.; Pomelli, C.; Adamo, C.; Clifford, S.; Ochterski, J.; Petersson, G. A.; Ayala, P. Y.; Cui, Q.; Morokuma, K.; Malick, D. K.; Rabuck, A. D.; Raghavachari, K.; Foresman, J. B.; Cioslowski, J.; Ortiz, J. V.; Stefanov, B. B.; Liu, G.; Liashenko, A.; Piskorz, P.; Komaromi, I.; Gomperts, R.; Martin, R. L.; Fox, D. J.; Keith, T.; Al-Laham, M. A.; Peng, C. Y.; Nanayakkara, A.; Gonzalez, C.; Challacombe, M.; Gill, P. M. W.; Johnson, B.; Chen, W.; Wong, M. W.; Andres, J. L.; Gonzalez, C.; Head-Gordon, M.; Replogle, E. S.; Pople, J. A.; *Gaussian*; Gaussian, Inc.: Pittsburgh PA, 1998.
28. Saracino, G. A. A.; Improta, R.; Barone, V.; *Chem. Phys. Lett.* **2003**, 373, 411.
29. Barone, V.; Cossi, M.; Tomasi, J.; *J. Chem. Phys.* **1997**, 107, 3210.
30. Kivekas, R.; Pajunem, A.; Navarrete, A.; Colacio, E.; *Inorg. Chim. Acta* **1999**, 284, 292.
31. Fettouhi, M.; Ouahab, L.; Boukhari, A.; Cador, O.; Mathonière, C.; Kahn, O.; *Inorg. Chem.* **1996**, 35, 4932.
32. Nakamoto, K.; *Infrared Spectra of Inorganic and Coordination Compounds*, John Wiley: New York, 1963.
33. Colthup, N. B.; Daly, L. H.; Wiberley, S. E.; *Introduction to Infrared and Raman Spectroscopy*, Academic Press: New York, 1964.
34. Nonoyama, M.; Ojima, H.; Ohki, K.; Nonoyama, K.; *Inorg. Chim. Acta* **1980**, 41, 155.
35. Greenwood, N. N.; Gibb, T. C.; *Mössbauer Spectroscopy*, Chapman and Hall: London, 1971.
36. Bancroft, G. M.; *Mössbauer Spectroscopy: An Introduction for Inorganic Chemists and Geochemists*, McGraw-Hill: London, 1973.
37. Berrett, R. R.; Fitzsimmons, B. W.; *Chem. Comm.* **1966**, 91.
38. Berrett, R. R.; Fitzsimmons, B. W.; *J. Chem. Soc.* **1967**, A, 525.
39. De Abreu, H. A.; Guimarães, L.; Duarte, H. A.; *J. Phys. Chem. A* **2006**, 110, 7713.
40. Rotzinger, F. P.; *J. Phys. Chem. B* **2005**, 109, 1510.
41. Cotton, F. A.; Daniels, L. M.; Murillo, C. A.; Quesada, J. F.; *Inorg. Chem.* **1993**, 32, 4861.

Received: June 12, 2006

Published on the web: December 1, 2006

FAPESP helped in meeting the publication costs of this article.

Iron(III) oxamato-catalyzed epoxidation of alkenes by dioxygen and pivalaldehyde

Rafael Ruiz,^a Maria Triannidis,^a Ally Aukauloo,^a Yves Journaux,^{*a} Isabel Fernández,^b José R. Pedro,^{*b} Beatriz Cervera,^c Isabel Castro^c and M. Carmen Muñoz^d

^a Laboratoire de Chimie Inorganique, URA 420, CNRS, Université de Paris-Sud, 91405 Orsay, France

^b Departament de Química Orgànica, Facultat de Química, Universitat de València, 46100 Burjassot, València, Spain

^c Departament de Química Inorgànica, Facultat de Química, Universitat de València, 46100 Burjassot, València, Spain

^d Departamento de Física Aplicada, Universidad Politécnica de València, 46071 València, Spain

A new iron(III)–carbonato monomeric complex of *ortho*-phenylenebis(oxamato) (opba) **1** is synthesized, and spectroscopically and structurally characterized; it is a moderately efficient non-heme catalyst for the aerobic epoxidation of alkenes with co-oxidation of pivalaldehyde.

There has been always a great interest in iron coordination chemistry owing to the relevant role that this transition metal ion plays in biology, particularly as the active metal center embedded in a large number of proteins involved in oxygen activation chemistry.¹ Now, this interest is directed towards mono- and di-nuclear non-heme iron proteins, owing to the surprisingly diverse functional properties exhibited by them.² Amido groups from asparagine or glutamine residues in the polypeptide backbone of some of these mononuclear iron proteins are frequently shown to coordinate to the iron metal center through their oxygen donor atom, like in lipid dioxygenase and isopenicillin *N*-synthase.^{2a} Moreover, amido nitrogen coordination has been invoked in bleomycin, a natural iron-containing glycopeptide with antibiotic and antitumor properties of fundamental importance in medicine.^{2a} That being so, it is evident that knowledge of the chemistry and reactivity properties of iron–amido complexes becomes particularly appropriate in order to understand the key steps of the enzymatic mechanism proposed for this class of non-heme iron proteins and antibiotics. Since the review of Sigel and Martin devoted to the coordinating properties of the amide bond with copper, nickel, cobalt and zinc metal ions,³ a considerable effort has been made in the last fifteen years in order to detect iron ion interactions with the amide group.^{4–6} Recently, we have initiated an investigation program to assess the possible use of bis-*N*-substituted oxamato ligands like *ortho*-phenylenebis(oxamato) (opba) in the stabilization of unusual high oxidation state transition metal ions due to the high donor capacity of the deprotonated-amido group.⁷ We report here on the synthesis and physical characterization,[†] and the crystal and molecular structure[‡] of its corresponding oxamato iron(III) complex of formula [NMe₄]₃[Fe(opba)(CO₃)]·5H₂O **1**, as well as its activity toward alkene epoxidation with dioxygen.

Complex **1** consists of mononuclear [Fe(opba)(CO₃)]^{3–} complex anions (Fig. 1), tetramethylammonium cations and crystallization water molecules. The iron atom is bound to the two deprotonated amido nitrogens and two carboxylate oxygens of the opba ligand and to two oxygen atoms from the carbonate in a rhombically distorted octahedral coordination geometry. The carbonate chelating group is symmetrically bound to the metal (2.034, 2.045 Å for Fe–O) occupying two *cis* positions of the octahedron with a typical small bite angle [63.2° for O(7)–Fe–O(8)]. This imposes a non-planar conformation for the tetradentate opba ligand which is the only compatible with an octahedral environment at the metal ion. In fact, the opba ligand adopts a *cis*-β geometry with the N(1), N(2) and O(2) donor atoms occupying three meridional positions around iron. This

situation contrasts to previous descriptions of mononuclear complexes with this ligand or its derivatives in which all four donor atoms form a plane (*trans* geometry).^{7,8} The distortion from planarity of the opba ligand is accommodated by a disrotatory rotation of the C(3)–N(2) amide bond defined as the angle between the C(6)C(3)N(2) and C(3)N(2)C(4) mean planes [17 *cf.* 2° for the equivalent C(1)–N(1) amide bond], as previously observed in a related cobalt(III) diamido-*N*-dialkoxido complex.⁹ This distortion is also reflected in the metal–ligand bond lengths, with a significant difference between the two Fe–O(carboxylate) bond distances of *ca.* 0.05 Å, the longer Fe–O(5) distance being *trans* to that of the carbonate ligand Fe–O(8) which is the longest bond of the octahedron. The Fe–N(amide) bond distances average 2.05 Å, a value very close to that observed in high-spin iron(III) complexes containing amido nitrogen bonds,⁵ but significantly longer than those of the analogous intermediate^{4b} or low-spin⁶ iron(III)–amide bonds (1.93–1.96 Å).

In order to uncover the potential reactivity of this new iron(III) complex, we have examined its ability to catalyse the epoxidation of some representative disubstituted alkenes using dioxygen as oxidant in the presence of an aldehyde.¹⁰ The

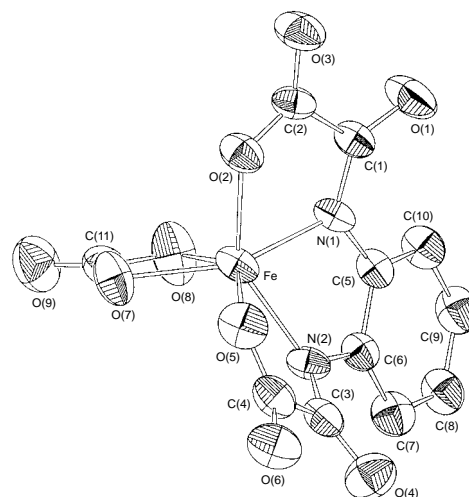


Fig. 1 Perspective view of the anionic mononuclear unit of **1** with the atom numbering scheme (thermal ellipsoids are at the 30% probability level and hydrogen atoms have been omitted for clarity). Selected bond distances (Å) and angles (°) with standard deviations in parentheses: Fe–N(1) 2.048(5), Fe–N(2) 2.045(6), Fe–O(2) 1.986(4), Fe–O(5) 2.035(4), Fe–O(7) 2.034(5), Fe–O(8) 2.045(5); N(1)–Fe–N(2) 75.9(2), N(1)–Fe–O(2) 78.5(2), N(1)–Fe–O(5) 125.5(2), N(1)–Fe–O(7) 147.4(2), N(1)–Fe–O(8) 86.9(2), N(2)–Fe–O(2) 142.8(2), N(2)–Fe–O(5) 77.9(2), N(2)–Fe–O(7) 118.9(2), N(2)–Fe–O(8) 98.9(3), O(2)–Fe–O(5) 96.0(2), O(2)–Fe–O(7) 97.1(2), O(2)–Fe–O(8) 106.2(2), O(5)–Fe–O(7) 86.9(2), O(5)–Fe–O(8) 144.2(2), O(7)–Fe–O(8) 63.2(2).

Table 1 Results for the epoxidation of alkenes by dioxygen and pivalaldehyde catalyzed by **1**^a

Entry	Alkene	t/h	Yield ^{b,c} (%)
1	<i>trans</i> -Stilbene	3	95
2	<i>cis</i> -Stilbene	3 ^d	15
3	Cyclohexene	4	45
4	1,2-Dihydronaphthalene	4	50
5	1,2-Dihydronaphthalene ^e	4	80

^a Reactions were carried out at room temperature by adding a fluorobenzene solution (0.2 ml) of the alkene (0.11 mmol) to a stirred mixture of the metal catalyst (6.5×10^{-3} mmol) and pivalaldehyde (0.33 mmol) in fluorobenzene (0.2 ml) under dioxygen atmosphere. The consumption of the alkene and the formation of the corresponding epoxide during the course of the reaction were monitored by TLC. The obtained epoxide and the unreacted alkene were separated by flash column chromatography on silica gel. ^b Yields refer to isolated and pure compounds (column chromatography on silica gel). All compounds exhibited spectral data consistent with their structures. ^c In the absence of catalyst some extension of epoxidation was observed. ^d With a reaction time of 24 h the final conversion was almost identical (*ca.* 20%). ^e In the presence of *N*-methylimidazole (0.11 mmol).

results are summarized in Table 1. Complex **1** catalyses the epoxidation of *trans*-stilbene by dioxygen plus pivalaldehyde in fluorobenzene solution with yields as high as 95% of the corresponding epoxide, *trans*-stilbene oxide, after 3 h (entry 1). By contrast, the percent conversion in the case of *cis*-stilbene is of only 15–20% even after a total reaction time of 24 h (entry 2), indicating that the catalytic epoxidation is greatly stereodependent. For both *cis*- and *trans*-stilbene, however, epoxides were the only oxidation products as confirmed by ¹H NMR spectroscopy. As a matter of fact, no trace of the corresponding ketone or alcohol were detected for the epoxidation of cyclohexene which is typically regarded as a good substrate to check for competition of alkene epoxidation *vs.* allylic oxidation (entry 3). This observation suggests that typical free radical intermediates are not directly involved as potential epoxidizing agents. On the other hand, it is noteworthy that the amount of epoxide obtained with **1** increases in the presence of *N*-methylimidazole: for instance, almost a twofold yield enhancement was found for the epoxidation of 1,2-dihydronaphthalene, *i.e.* from 50 to 80% after 4 h (entries 4 and 5, respectively). Although it is premature to discuss the precise mechanism at the present stage, *N*-methylimidazole most likely acts as a monodentate donor ligand toward the iron(III) ion by replacement of the bidentate carbonate ligand, and thereby affording a vacant coordination site on the iron center for reaction with the potential oxidant. Furthermore, even if the exact role of the metal complex in the epoxidation of alkenes by dioxygen with co-oxidation of aldehydes is still unclear, recent studies by Valentine and coworkers¹¹ demonstrate that it coordinates to the acylperoxy radicals generated in the auto-oxidation of the aldehyde forming a metal-acylperoxo complex. That being so, iron(IV)-acylperoxo or iron(V)-oxo species derived by oxygen–oxygen bond cleavage of the acylperoxo group, seem to us the more probable candidates to play the role of active epoxidizing agents in our system. In this regard, it is interesting to note that Collins *et al.* have isolated stable iron(IV) complexes with amido-containing ligands which would be a model for the proposed catalytic entities in our oxidation system.^{4a} Attempts to characterize these reactive intermediates species using other transition metal ions with more accessible high-valent oxidation states such as manganese are in progress in our laboratory.

This work was supported by the DGICYT, Ministerio de Educación y Ciencia (Spain) through projects PB94-0985 and PB94-1002. We acknowledge the financial support of the group Rhône-Poulenc. R. R. and B. C. thank the Ministerio de Educación y Ciencia (Spain) and the Conselleria de Educació i Ciència de la Generalitat Valenciana (Spain) for grants. We

would also like to express our gratitude to Dr J. J. Girerd and Dr P. Mialane for fruitful discussions.

Footnotes and References

* E-mail: jour@icmo.u-psud.fr

† *Syntheses and selected data for 1*: A solution of the diethyl ester derivative of opba (1.54 g, 5 mmol) in methanol (100 ml) was charged with a 25% methanol solution of NMe₄OH (10 cm³, 25 mmol) and the resulting mixture was stirred at 60 °C for 15 min in order to facilitate the hydrolysis of the ethyl ester groups. A methanolic solution (50 ml) of iron(III) perchlorate hydrate (1.77 g, 5 mmol) was then added dropwise *via* a dropping funnel under stirring. The resulting intensely red coloured solution was filtered to eliminate the white precipitate of NMe₄ClO₄, and reduced to a final volume of 10 ml on a rotatory evaporator. The concentrated solution was treated successively with diethyl ether and acetone to give a very hygroscopic product (solid or oil) which was recuperated with acetonitrile (300 ml). The suspension obtained was gently heated for 5 h with vigorous stirring and then filtered to eliminate the remainder of the solid particles. Upon standing at room temperature, a first crop of a side product appeared which was also filtered and separated from the mother-liquor. Slow evaporation of the filtered solution in air afforded, after 2 weeks, red needles of **1** in small amounts which were picked by hand, dried on filter paper and stored under vacuum owing to its hygroscopic character. The crystals so obtained were suitable for X-ray diffraction. Satisfactory elemental analyses were obtained (C, H, N, Fe). $\nu_{\text{max}}/\text{cm}^{-1}$ (KBr) 1660s (sh), 1635vs (br) and 1571s (CO) (opba ligand and CO₃²⁻) and 950s (NC) from NMe₄⁺. UV–VIS (MeCN) $\lambda_{\text{max}}/\text{nm}$ [ϵ dm³ mol⁻¹ cm⁻¹] 221 (4.0×10^4), 257 (4.2×10^4), 264 (sh), 308 (3.0×10^4), 408 (2.7×10^3). Magnetic moment (room temp.): 5.9 μ_B . EPR spectrum (X-band, powder sample, liquid-N₂ temperature): a strong feature at $g_{\text{eff}} = 4.3$ which typically arises in a completely rhombic system ($E/D = 1/3$) for $D > 0.23$ cm⁻¹.

‡ *X-Ray crystal structure analysis*: Enraf-Nonius CAD-4 diffractometer, Mo-K α radiation, $\lambda = 0.71069$ Å, graphite monochromator, 293 K. Lorentz and polarization effects but not absorption correction ($\mu = 9.26$ cm⁻¹). Data collection, solution and refinement: ω - θ , standard Patterson methods with subsequent full-matrix least-squares method refinement. SHELX86, SHELX93.¹² C₂₃H₅₀FeN₅O₁₄, monoclinic, space group *P*2₁/*a*, $a = 11.441(2)$, $b = 17.496(2)$, $c = 17.047(2)$ Å, $\beta = 104.52(2)^\circ$, $U = 3303(1)$ Å³, $Z = 4$, $D_c = 1.36$ g cm⁻³, $1 \leq \theta \leq 25^\circ$, crystal size $0.15 \times 0.10 \times 0.05$ mm. 4456 unique reflections with 3362 assumed as observed with $I \geq 2\sigma(I)$. The hydrogen atoms were located from a difference synthesis and refined with an overall isotropic thermal parameter. Refinement on F^2 of 390 variables with anisotropic thermal parameters for all non-hydrogen atoms gave $R = 0.079$ and $R_w = 0.108$ with $S = 1.8$ (observed data). CCDC 182/628.

- 1 *Active Oxygen in Biochemistry*, ed. J. S. Valentine, C. S. Foote, A. Greenberg and J. F. Liebman, Chapman and Hall, London, 1995.
- 2 (a) A. L. Nivorozhkin and J. J. Girerd, *Angew. Chem., Int. Ed. Engl.*, 1996, **35**, 609 and references therein; (b) L. Que, Jr. and Y. Dong, *Acc. Chem. Res.*, 1996, **29**, 190.
- 3 H. Sigel and R. B. Martin, *Chem. Rev.*, 1982, **82**, 385.
- 4 (a) T. J. Collins, K. L. Kostka, E. Münck and E. Uffelman, *J. Am. Chem. Soc.*, 1990, **112**, 5637; (b) K. L. Kostka, B. G. Fox, M. P. Hendrich, T. J. Collins, C. E. F. Rickard, L. J. Wright, E. Münck, *J. Am. Chem. Soc.*, 1993, **115**, 6746.
- 5 Y. Yang, F. Diederich and J. S. Valentine, *J. Am. Chem. Soc.*, 1991, **113**, 7195.
- 6 X. Tao, D. W. Stephan and P. K. Mascharak, *Inorg. Chem.*, 1987, **26**, 754.
- 7 R. Ruiz, C. Surville-Barland, A. Aukauloo, E. Anxolabehere-Mallart, Y. Journaux, J. Cano and M. C. Muñoz, *J. Chem. Soc., Dalton Trans.*, 1997, 745.
- 8 M. Tettouhi, L. Ouahab, A. Boukhari, O. Cador, C. Mathoniere and O. Kahn, *Inorg. Chem.*, 1996, **35**, 4932.
- 9 T. J. Collins and J. M. Workman, *Angew. Chem., Int. Ed. Engl.*, 1989, **28**, 912.
- 10 J. Estrada, I. Fernandez, J. R. Pedro, X. Ottenwaelde, R. Ruiz and Y. Journaux, *Tetrahedron Lett.*, 1997, **38**, 2377.
- 11 W. Nam, H. J. Kim, S. H. Kim, R. Y. N. Ho and J. S. Valentine, *Inorg. Chem.*, 1996, **35**, 1045 and references therein.
- 12 G. M. Sheldrick, SHELX. A Program for Crystal Structure Determination, University of Göttingen, DFR, 1986; G. M. Sheldrick, SHELXL93. Program for the Refinement of Crystal Structures, University of Göttingen, 1993.

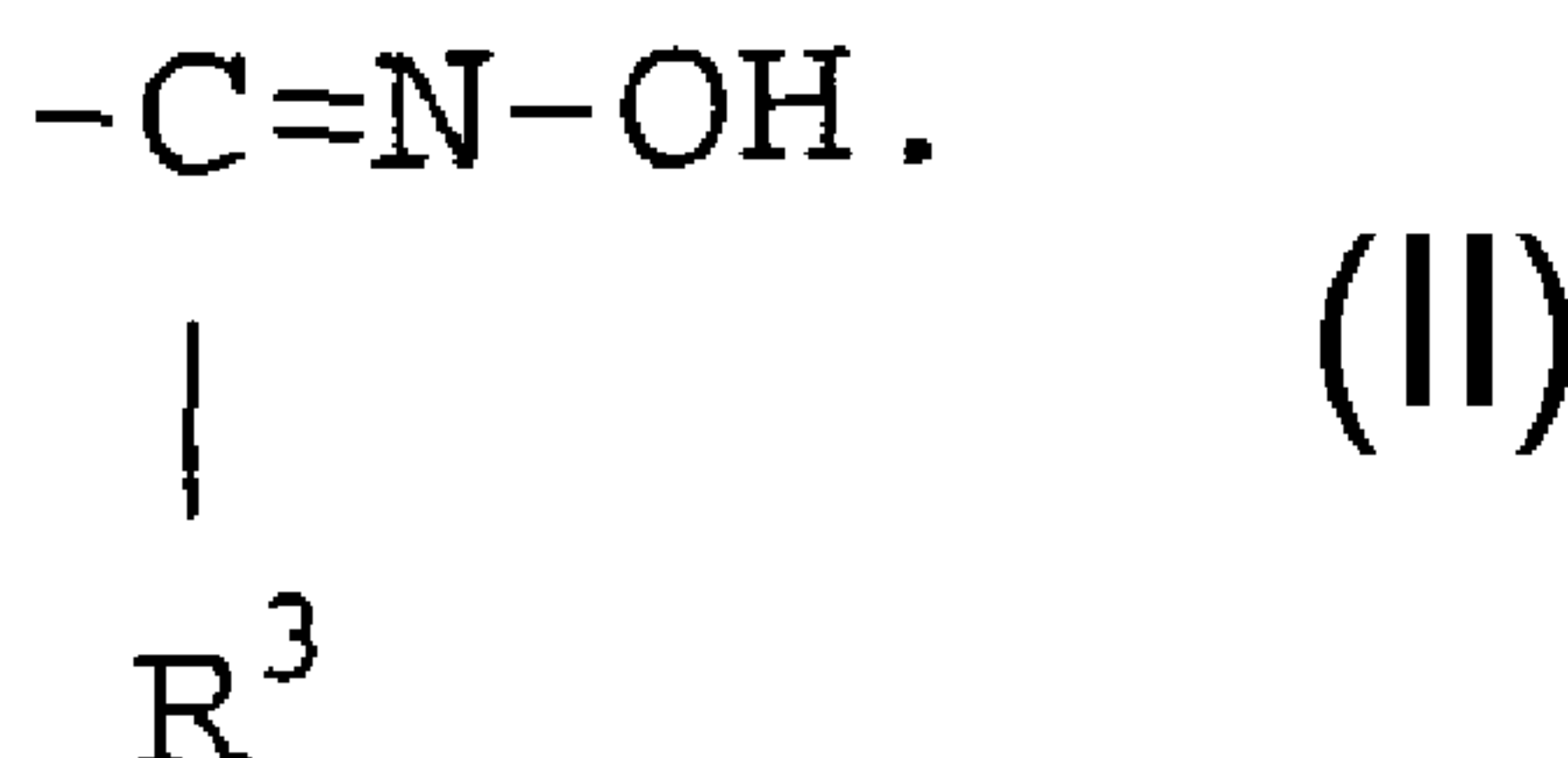
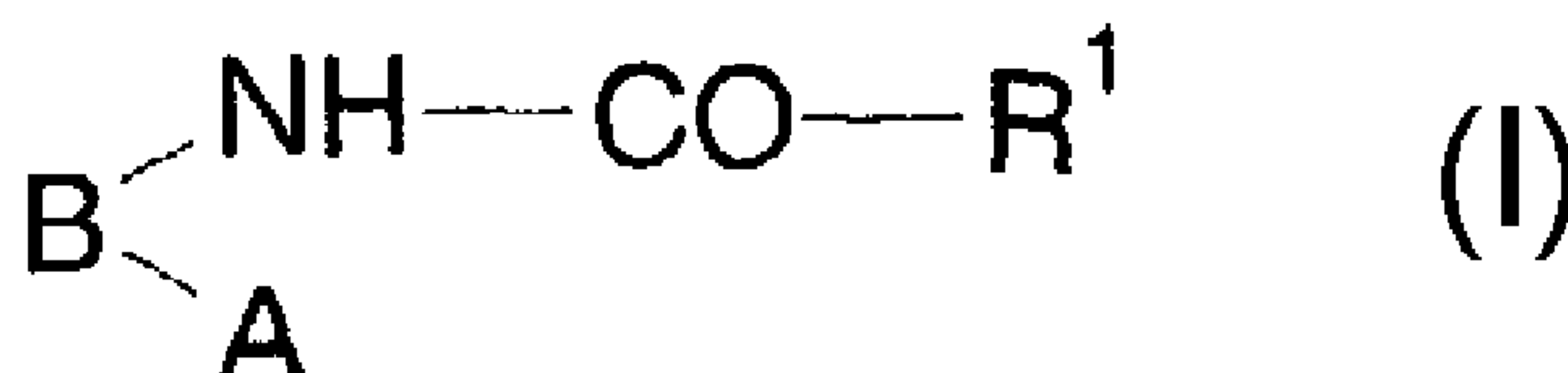
Received in Basel, Switzerland, 7th August 1997; 7/05787C



(86) Date de dépôt PCT/PCT Filing Date: 2003/05/30
(87) Date publication PCT/PCT Publication Date: 2003/12/31
(85) Entrée phase nationale/National Entry: 2004/12/20
(86) N° demande PCT/PCT Application No.: EP 2003/005674
(87) N° publication PCT/PCT Publication No.: 2004/000986
(30) Priorité/Priority: 2002/06/21 (102 27 774.5) DE

(51) Cl.Int.⁷/Int.Cl.⁷ C11D 3/39
(71) Demandeur/Applicant:
DEGUSSA AG, DE
(72) Inventeurs/Inventors:
KUNZ, ULRIKE, DE;
JAKOB, HARALD, DE;
DEL GROSSO, MICHAEL, SG;
DORFER, ASTRID, DE
(74) Agent: MARKS & CLERK

(54) Titre : CATALYSEURS DE BLANCHIMENT ET COMPOSITIONS D'AGENTS DE BLANCHIMENT A BASE DE COMPLEXES DE METAUX DE TRANSITION A LIGANDS POLYDENTES AZOTES
(54) Title: USE OF TRANSITION METAL COMPLEXES WITH NITROGEN-CONTAINING POLYDENTATE LIGANDS AS A BLEACHING CATALYST AND BLEACHING AGENT COMPOSITION



(57) **Abrégé/Abstract:**

Transition metal complexes are used as bleaching catalysts for peroxy compounds. Transition metal complexes to be used according to the invention contain a ligand of the general formula (I) wherein B is a bridge member, such as o-phenylene or pyridine-2,6-diyl, and A represents the group -NH-CO-R₁ or formula (II).



(12) INTERNATIONAL APPLICATION PUBLISHED UNDER THE PATENT COOPERATION TREATY (PCT)

(19) World Intellectual Property
Organization
International Bureau



(43) International Publication Date
31 December 2003 (31.12.2003)

PCT

(10) International Publication Number
WO 2004/000986 A1

(51) International Patent Classification⁷: **C11D 3/39**

(21) International Application Number:
PCT/EP2003/005674

(22) International Filing Date: 30 May 2003 (30.05.2003)

(25) Filing Language: English

(26) Publication Language: English

(30) Priority Data:
102 27 774.5 21 June 2002 (21.06.2002) DE

(71) Applicant: **DEGUSSA AG** [DE/DE]; Bennigsenplatz 1,
40474 Düsseldorf (DE).

(72) Inventors: **KUNZ, Ulrike**; Kapellenweg 61, 63571
Gelnhausen (DE). **JAKOB, Harald**; Meerholzer Strasse
1, 63594 Hasselroth (DE). **DEL GROSSO, Michael**;
16 Balmoral Crescent, 04-02 Balmoral Resid., 259910
Singapur (SG). **DORFER, Astrid**; John-Wesley-Strasse
13, 63584 Gründau (DE).

(81) Designated States (*national*): AE, AG, AL, AM, AT, AU,
AZ, BA, BB, BG, BR, BY, BZ, CA, CH, CN, CO, CR, CU,
CZ, DE, DK, DM, DZ, EC, EE, ES, FI, GB, GD, GE, GH,
GM, HR, HU, ID, IL, IN, IS, JP, KE, KG, KP, KR, KZ, LC,
LK, LR, LS, LT, LU, LV, MA, MD, MG, MK, MN, MW,
MX, MZ, NI, NO, NZ, OM, PH, PL, PT, RO, RU, SC, SD,
SE, SG, SK, SL, TJ, TM, TN, TR, TT, TZ, UA, UG, UZ,
VC, VN, YU, ZA, ZM, ZW.

(84) Designated States (*regional*): ARIPO patent (GH, GM,
KE, LS, MW, MZ, SD, SL, SZ, TZ, UG, ZM, ZW),
Eurasian patent (AM, AZ, BY, KG, KZ, MD, RU, TJ, TM),
European patent (AT, BE, BG, CH, CY, CZ, DE, DK, EE,
ES, FI, FR, GB, GR, HU, IE, IT, LU, MC, NL, PT, RO,
SE, SI, SK, TR), OAPI patent (BF, BJ, CF, CG, CI, CM,
GA, GN, GQ, GW, ML, MR, NE, SN, TD, TG).

Declaration under Rule 4.17:

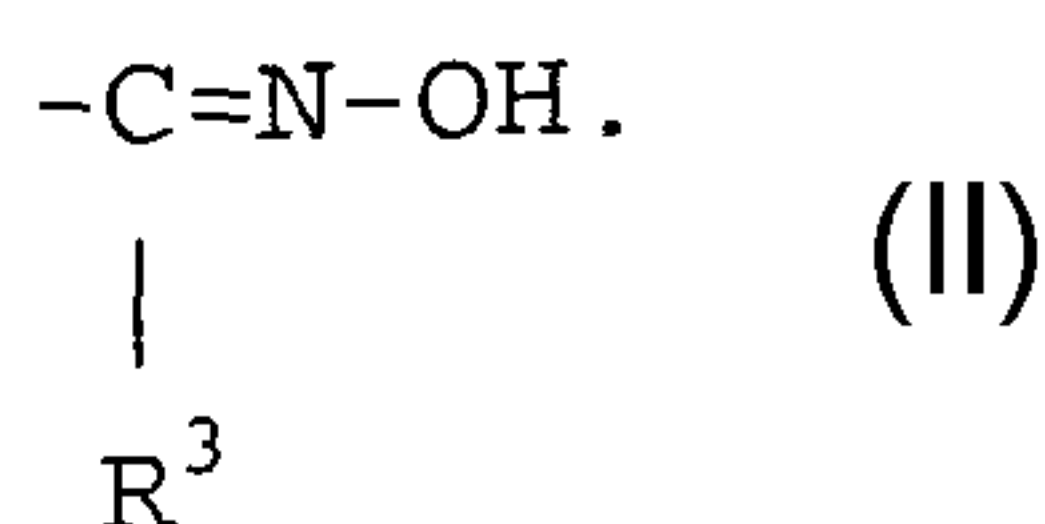
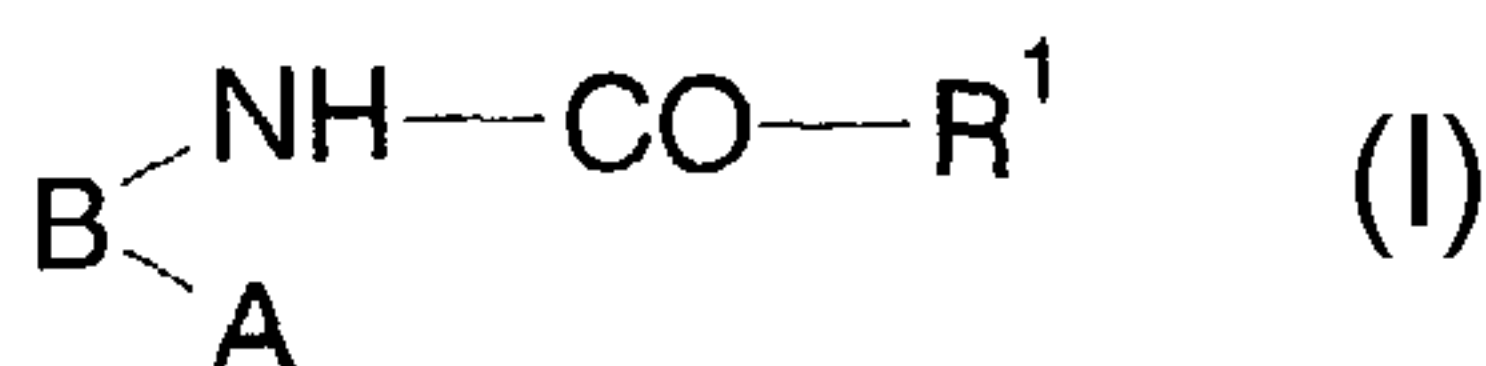
— *as to applicant's entitlement to apply for and be granted
a patent (Rule 4.17(ii)) for the following designations AE,
AG, AL, AM, AT, AU, AZ, BA, BB, BG, BR, BY, BZ, CA, CH,
CN, CO, CR, CU, CZ, DE, DK, DM, DZ, EC, EE, ES, FI,
GB, GD, GE, GH, GM, HR, HU, ID, IL, IN, IS, JP, KE, KG,
KP, KR, KZ, LC, LK, LR, LS, LT, LU, LV, MA, MD, MG, MK,
MN, MW, MX, MZ, NI, NO, NZ, OM, PH, PL, PT, RO, RU,
SC, SD, SE, SG, SK, SL, TJ, TM, TN, TR, TT, TZ, UA, UG,
UZ, VC, VN, YU, ZA, ZM, ZW, ARIPO patent (GH, GM,
KE, LS, MW, MZ, SD, SL, SZ, TZ, UG, ZM, ZW), Eurasian
patent (AM, AZ, BY, KG, KZ, MD, RU, TJ, TM), European
patent (AT, BE, BG, CH, CY, CZ, DE, DK, EE, ES, FI, FR,
GB, GR, HU, IE, IT, LU, MC, NL, PT, RO, SE, SI, SK, TR),
OAPI patent (BF, BJ, CF, CG, CI, CM, GA, GN, GQ, GW,
ML, MR, NE, SN, TD, TG)*

Published:

— *with international search report*

*For two-letter codes and other abbreviations, refer to the "Guid-
ance Notes on Codes and Abbreviations" appearing at the begin-
ning of each regular issue of the PCT Gazette.*

(54) Title: USE OF TRANSITION METAL COMPLEXES WITH NITROGEN-CONTAINING POLYDENTATE LIGANDS AS
A BLEACHING CATALYST AND BLEACHING AGENT COMPOSITION



(57) Abstract: Transition metal complexes are used as bleaching catalysts for peroxy compounds. Transition metal complexes to be used according to the invention contain a ligand of the general formula (I) wherein B is a bridge member, such as o-phenylene or pyridine-2,6-diyl, and A represents the group -NH-CO-R₁ or formula (II).



WO 2004/000986 A1

**Use of transition metal complexes with nitrogen-containing
polydentate ligands as a bleaching catalyst and bleaching
agent composition**

Description

5 The invention relates to the use of transition metal
complexes with nitrogen-containing polydentate ligands as a
bleaching catalyst and to bleaching agent compositions
comprising such a bleaching catalyst. The activity of
peroxy compounds in washing, bleaching and cleaning
10 processes at low temperature is increased by the transition
metal complexes to be used according to the invention.

Inorganic peroxy compounds, in particular hydrogen peroxide
and compounds which liberate hydrogen peroxide, such as
sodium perborate monohydrate, sodium perborate tetrahydrate
15 and sodium percarbonate, have been employed for a long
times as oxidizing agents in bleaching, washing and
cleaning processes. Sufficiently rapid bleaching of soiled
textiles requires a temperature of at least 80°C.

The oxidizing action of inorganic peroxygen compounds at
20 reduced temperature can be improved by co-using so-called
bleaching activators. Bleaching activators are, in
particular, N- and O-acyl compounds, for example
polyacylated alkylenediamines, such as
tetraacetylenethylenediamine (TAED), acetylated glycolurils,
25 N-acetylated hydantoins, diketopiperazines, carboxylic acid
anhydrides, carboxylic acid esters, such as, in particular,
sodium nonanoyloxy-benzenesulfonate (NOBS), and acylated
sugar derivatives.

By using a combination of a peroxy compound and an
30 activator, bleaching can be carried out at about 60°C
instead of above 80°C without a loss in activity.

In efforts to be able to carry out washing and bleaching below 60°C, the use of transition metal complexes, in particular complexes of manganese, iron, cobalt and copper with at least one polydentate organic ligand, in particular
5 nitrogen-containing ligands, has been described in many documents.

Reference is made by way of example to the complexes described in the following documents: EP 0 544 490, WO 98/54282, WO 00/12808, WO 00/60043, WO 00/52124, EP 0 392
10 592, WO 99/64156 and WO 00/12667.

Although numerous different transition metal complexes are thus known for the use aimed for, they only partly meet some of the expectations imposed on them.

Thus, if the reactivity is too high there is the risk of a
15 change in colour of dyed textiles, and in the extreme case oxidative damage to the fibres. Furthermore, some complexes decompose the peroxygen compound without a bleaching action, are insufficiently stable to hydrolysis or are susceptible to oxidation.

20 The doctrine of WO 00/32731 is bleaching catalysts with di(2-pyridyl)methylamine organic nitrogen-containing ligand. This catalyst is suitable for increasing the oxidizing and bleaching action of hydrogen peroxide. A further increase is achieved by combination of such a
25 bleaching catalyst with a so-called activator which can form a peroxycarboxylic acid in the presence of a source of hydrogen peroxide. As has been shown in practice, different property profiles of bleaching catalysts which the products known to date do not achieve in all points are required in
30 washing, bleaching and cleaning compositions.

The international application WO 98/03263 discloses homogeneous oxidation catalysts, these being transition metal complexes with a macrocyclic ligand. The ligand

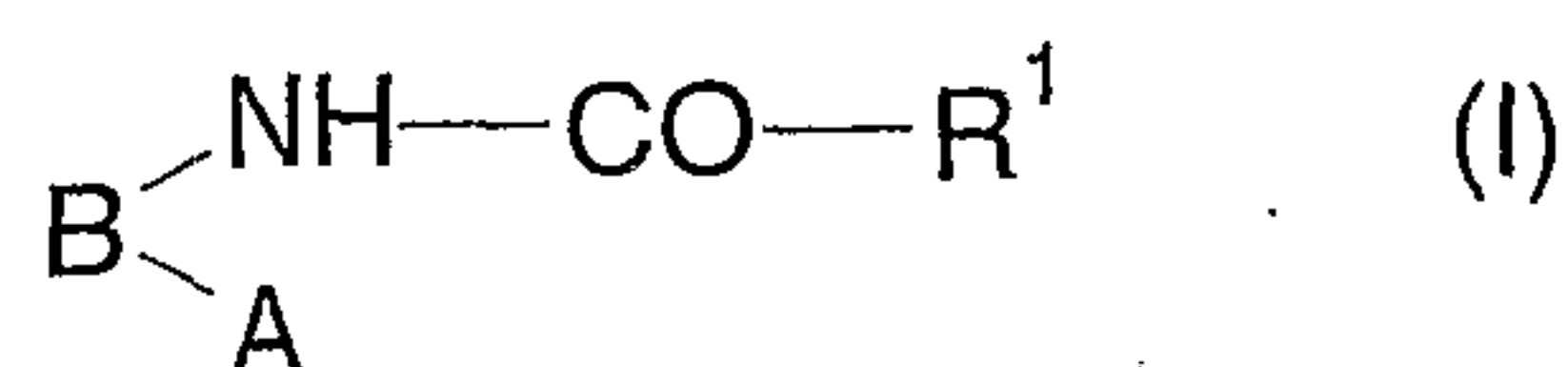
includes four donor atoms, such as nitrogen, usually in the form of amides, so that the ligand is a tetraamide. Further similar macrocyclic ligands and chelate complexes are the doctrine of WO 99/64156, where the ligand can contain four
 5 amidic or also two aminic and two amidic nitrogen atoms. Such ligands are indeed stable to oxidation, but the activity as a bleaching catalyst leaves something to be desired.

The object of the present invention is accordingly to
 10 provide further transition metal complexes with at least one nitrogen-containing polydentate ligand which are suitable as a bleaching catalyst for activation of a peroxy compound and preferably also oxygen.

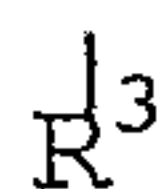
It has been found that transition metal complexes with a
 15 transition metal from the series consisting of manganese, iron, cobalt or copper are very active and gentle bleaching catalysts if these contain at least one nitrogen-containing polydentate ligand of the general formula (I) according to the claims.

20

The invention thus provides the use of a transition metal complex with at least one nitrogen-containing polydentate ligand as a bleaching catalyst for activation of a peroxy compound or of oxygen, wherein
 25 the complex is mono- or polynuclear, the transition metal (M) is manganese, iron, cobalt or copper and the nitrogen-containing polydentate ligand (L), at least one of which is present, has the general formula (I)

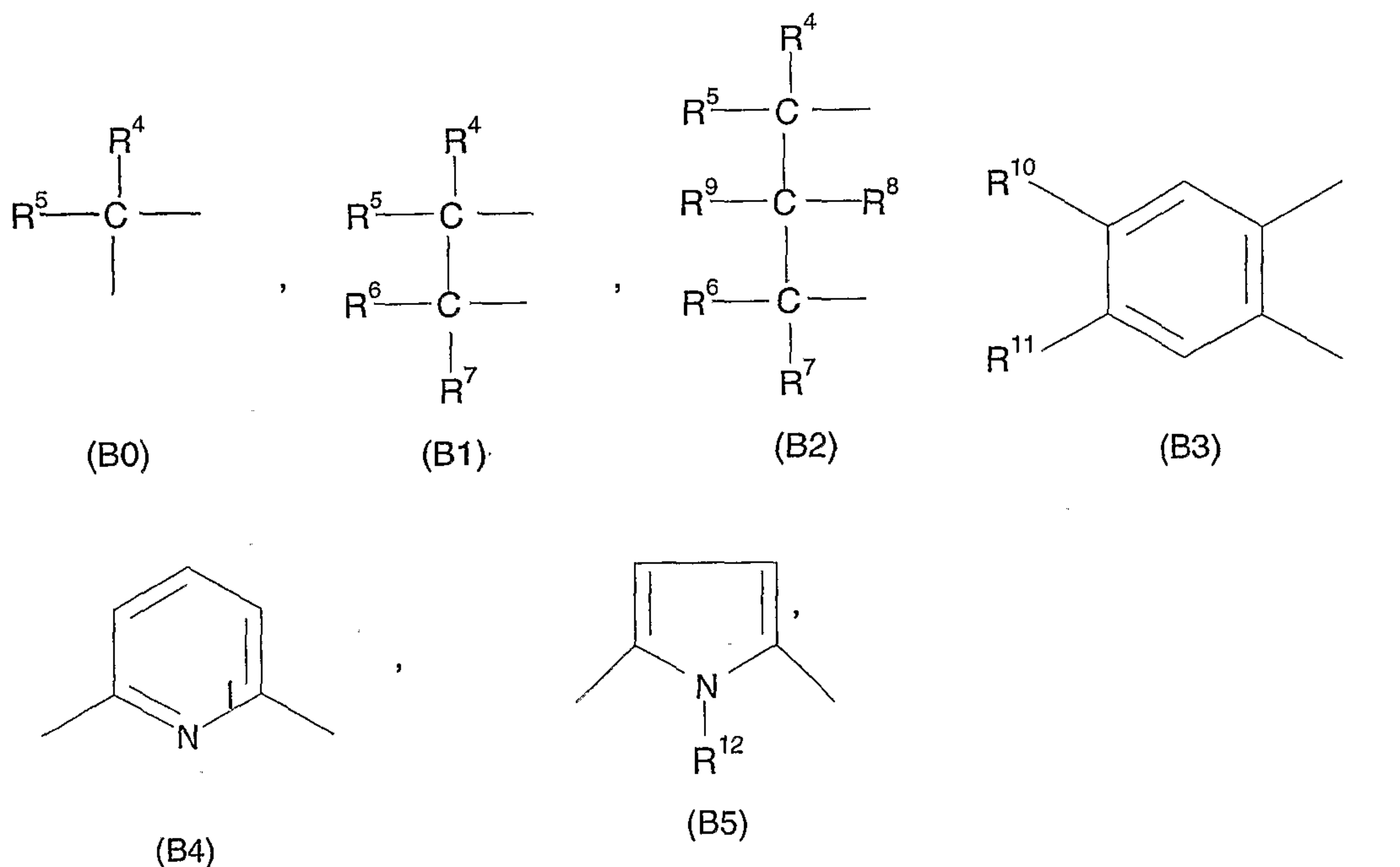


wherein A represents either the group $-\text{NH}-\text{CO}-\text{R}^2$ or the group $-\text{C}=\text{N}-\text{OZ}$,



the bridge member B is chosen from the series consisting of

5



wherein R^4 to R^7 independently of one another represent a radical from the series consisting of H, arylalkyl, aryl, heteroaryl,

10

wherein R^4 with R^5 or/and R^6 with R^7 or R^4 with R^6 together with the atom(s) carrying them can form a five- to seven-membered, in particular five- or six-membered cycloaliphatic or O- or N-heterocyclic ring, which can also contain a double bond,

15

and wherein the structural elements of the general formulae (B0) to (B5) have a total of 2 to 20 C atoms, R^8 and R^9 independently of one another can represent a radical from the series consisting of H, methyl or together can represent carbonyl oxygen,

20

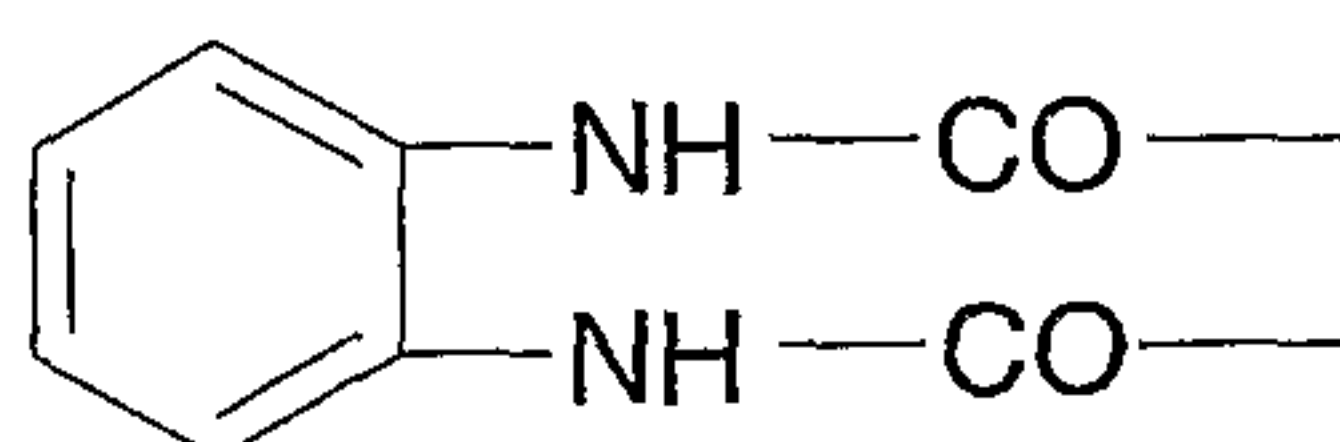
R^{10} and R^{11} independently of one another can represent a radical from the series consisting of H, (C_1-C_4) alkyl,

halogen or together can represent a fused-on aromatic ring

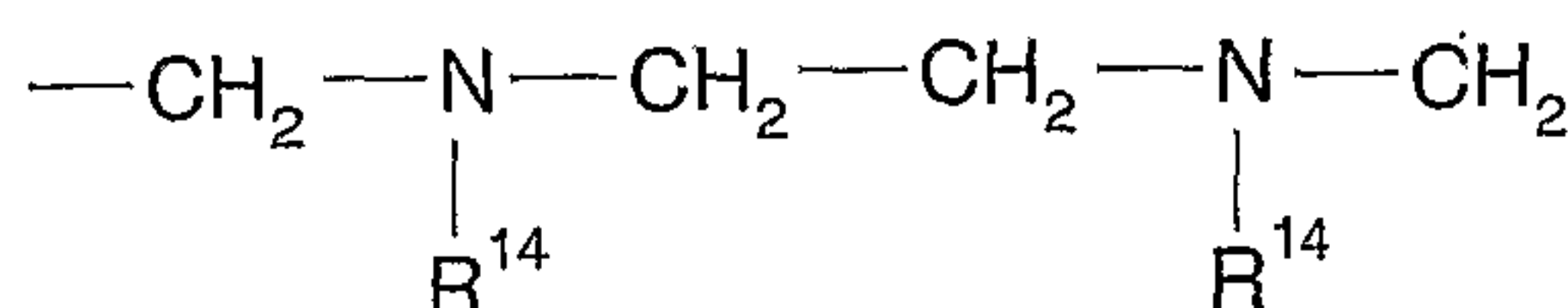
and R^{12} can represent H or methyl,

the radicals R^1 and R^2 independently of one another can

5 represent a radical from the series consisting of $-\text{COOH}$, $-\text{CONH}_2$, $-\text{CONHR}^{13}$, $\text{C}(\text{CH}_3)_2\text{OH}$, 2-pyridyl, 1,3-oxazolin-2-yl, imidazol-2-yl or R^1-R^2 together can represent the radical



or

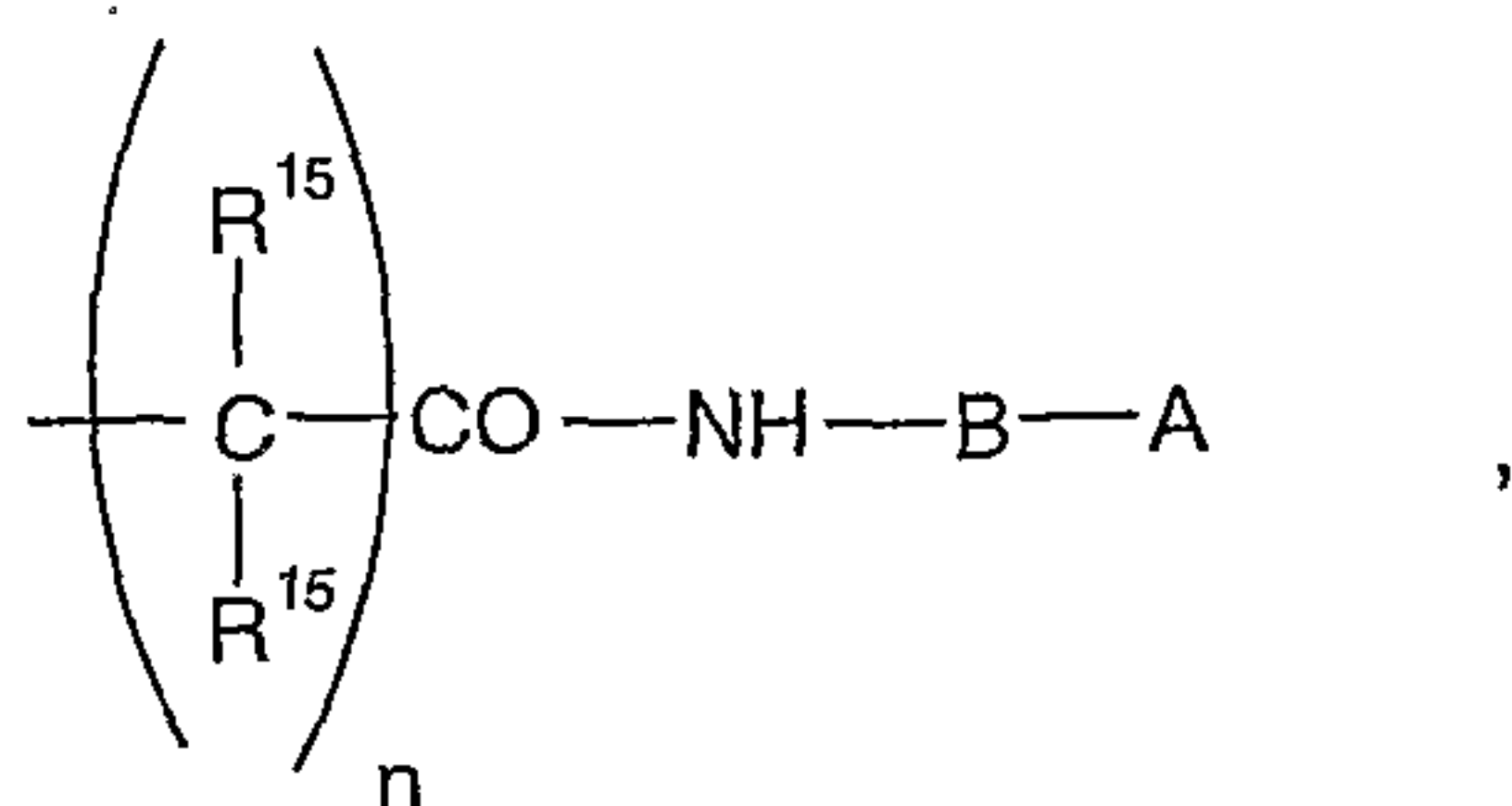


10

wherein R^{13} can be chosen from the series consisting of linear, branched or cyclic alkyl, aryl, heteroaryl, in particular 2-pyridyl, 1,3-oxazolin-2-yl and imidazol-2-yl and heteroalkylmethyl,

15 R^{14} can be chosen from the series consisting of substituted or unsubstituted, linear, branched or cyclic alkyl, benzyl, aryl, heteroaryl, heteroarylmethyl, and R^3 represents a radical from the series consisting of alkyl, aryl, heteroaryl, arylalkyl, heteroarylalkyl and
20 Z represents H, alkyl, aryl, dialkylaminoethyl, heteroaryl,

and in the case of the oximes R^1 additionally can represent the radical

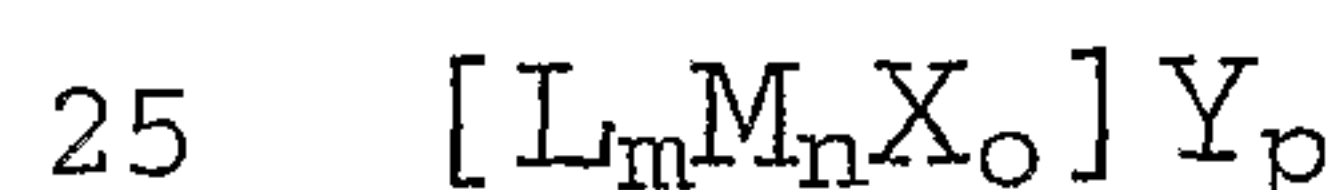


wherein n is 0 or 1, R^{15} H or alkyl, and the group $R^{15}-C-R^{15}$ can be cycloalkyl.

- 5 The subclaims relate to preferred embodiments of the use according to the invention.

The present invention also provides the bleaching agent composition defined in the claims, which comprises a peroxy compound, in particular a source of hydrogen peroxide, and
 10 a transition metal complex to be used according to the invention in an amount effective for activation. The subclaims of the bleaching agent composition relate to preferred embodiments thereof.

The transition metal complex to be used according to the
 15 invention can be mono- or polynuclear and contains as the transition metal one from the series consisting of manganese in the valency level II to IV, iron in the valency level II or III, cobalt in the valency level II or III and copper in the valency level I or II. Depending on
 20 the number of heteroatoms capable of ligand formation and their steric alignment in the ligand L, the complex can contain one or more transition metal atoms, preferably one or two metal atoms of the same type. In general the complex has the general formula



In this formula, L denotes the ligand to be used according to the invention, M denotes a transition metal atom from the abovementioned series, X denotes a coordinating neutral or mono- or polyvalent ligand for saturation of the ligand sphere and Y denotes a non-coordinating counter-ion, which can be anionic or, if the sum of anionic ligands X and ionic substituents in the ligand L exceeds the sum of the valency of the metal atoms M, can also be cationic. The index m represents an integer in the range from 1 to 4, in particular 1 or 2, the index n represents an integer, preferably 1 or 2, the index o represents zero or an integer in the range from 1 to 8 and the index p represents zero or an integer in order to achieve a complete charge compensation. Y can also be a substituent, such as carboxylate or sulfonate, in the ligand.

The polydentate ligand L to be used according to the invention has the structure according to the general formula (I) already shown. According to a preferred embodiment, the complexes are cobalt complexes with the ligand $B(NH-CO-R^1)_2$, wherein, particularly preferably, B represents optionally substituted ortho-phenylene and/or R^1 represents a radical from the series consisting of COOH, CONHR', $C(CH_3)_2OH$ where R' is H, (C_1-C_4) -alkyl or substituted alkyl and 2-pyridyl.

The bleaching activators to be used according to the invention can in some cases also be macrocyclic, but the ligands differ from the ligands according to WO 98/03263 and WO 99/64156 by at least one feature.

Ligands of preferred bleaching activators are open-chain, that is to say not macrocyclic. Several of these substances are more easily obtainable than the macrocyclic ligands which are already known. Surprisingly, the substances of sometimes simple structure with oxamic acid or oxamide structural elements show a surprisingly good bleaching-activating action. Apart from on the ligand structure and

on the metal atom of the complex, the action also depends in part on the coloured substance to be bleached.

A new genus of active transition metal complexes contain a chelate ligand with four nitrogen donor atoms, two of which have an amide structure and two N atoms of which are the constituent of an N-heterocyclic ring.

Finally, ligands with two amide groups and two oxime groups are interesting compounds for complexing of Mn, Fe, Co and Cu for the purpose of obtaining active bleaching activators.

The cyclic bridge members B can also have functional or non-functional substituents, for example OH, NH₂, COOH, SO₃H, COOMe, SO₃Me, wherein Me represents an alkali metal, N⁺(C₁-C₄-alkyl)₄, F, Cl, alkoxy, in particular (C₁-C₄)alkoxy, alkyl, in particular (C₁-C₄)alkyl, phenyl, benzyl, pyridyl, 2-pyridylmethyl.

The radicals R¹ and R² in the ligand L can be identical or different and represent H, linear, cyclic or branched alkyl or heteroalkyl, aryl, heteroaryl, arylalkyl and heteroarylalkyl. Examples are methyl, ethyl, i-propyl, tert-butyl, benzyl, phenyl, pyridyl, in particular 2-pyridyl, 1,3-oxazolin-2-yl, 1,3-oxazolin-2-methyl and 2-pyridylmethyl.

The radical R³ in the ligand L can be aryl, heteroaryl, alkoxy, aryloxy, heteroaryl, alkyl and arylalkyl. The examples mentioned above for R¹ and R² also apply here. If R³ represents alkoxy or aryloxy, it is preferably methoxy,

ethoxy, 2-hydroxyethoxy, 2-aminoethoxy, 2-N,N-di(C₁-C₄)alkylaminoethoxy and phenoxy.

Both the radicals R¹ to R³ and bridge members (B1 to B5)
5 can have one or more functional or non-functional
substituents. These are those substituents such as have
already been disclosed in connection with the description
of the bridge member B. According to particularly preferred
embodiments, the heterocyclic or heteroaromatic ring
10 systems bonded to the bridge member B contain one or more
linear or branched (C₁-C₄)alkyl groups, in particular
methyl, isopropyl and tert-butyl, and furthermore phenyl,
benzyl, 2-pyridylmethyl or -ethyl or 4-imidazolylmethyl or
-ethyl.

15

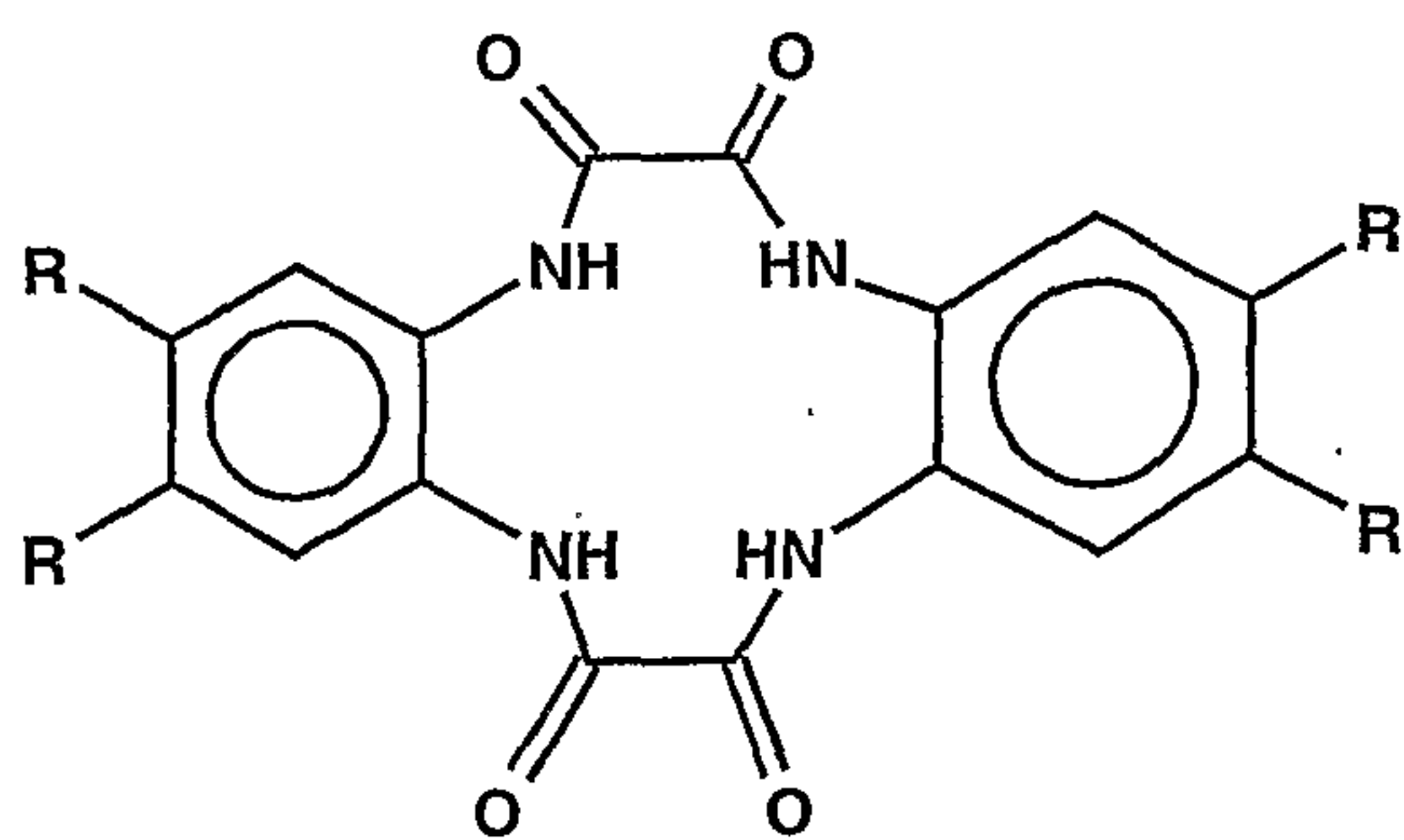
According to a further preferred embodiment, one or more
radicals from the series consisting of R¹ to R¹⁵ or the
nitrogen-containing ring systems formed therefrom contain
hydrophilic substituents in order to increase the
20 solubility of the complex. Examples of these are salt-
forming functional substituents and hydroxyalkoxy
groupings, which additionally can also contain one or more
ether bridges.

25 The chemical name for some examples of suitable ligands and
the formulae of some complexes containing them follow
below:

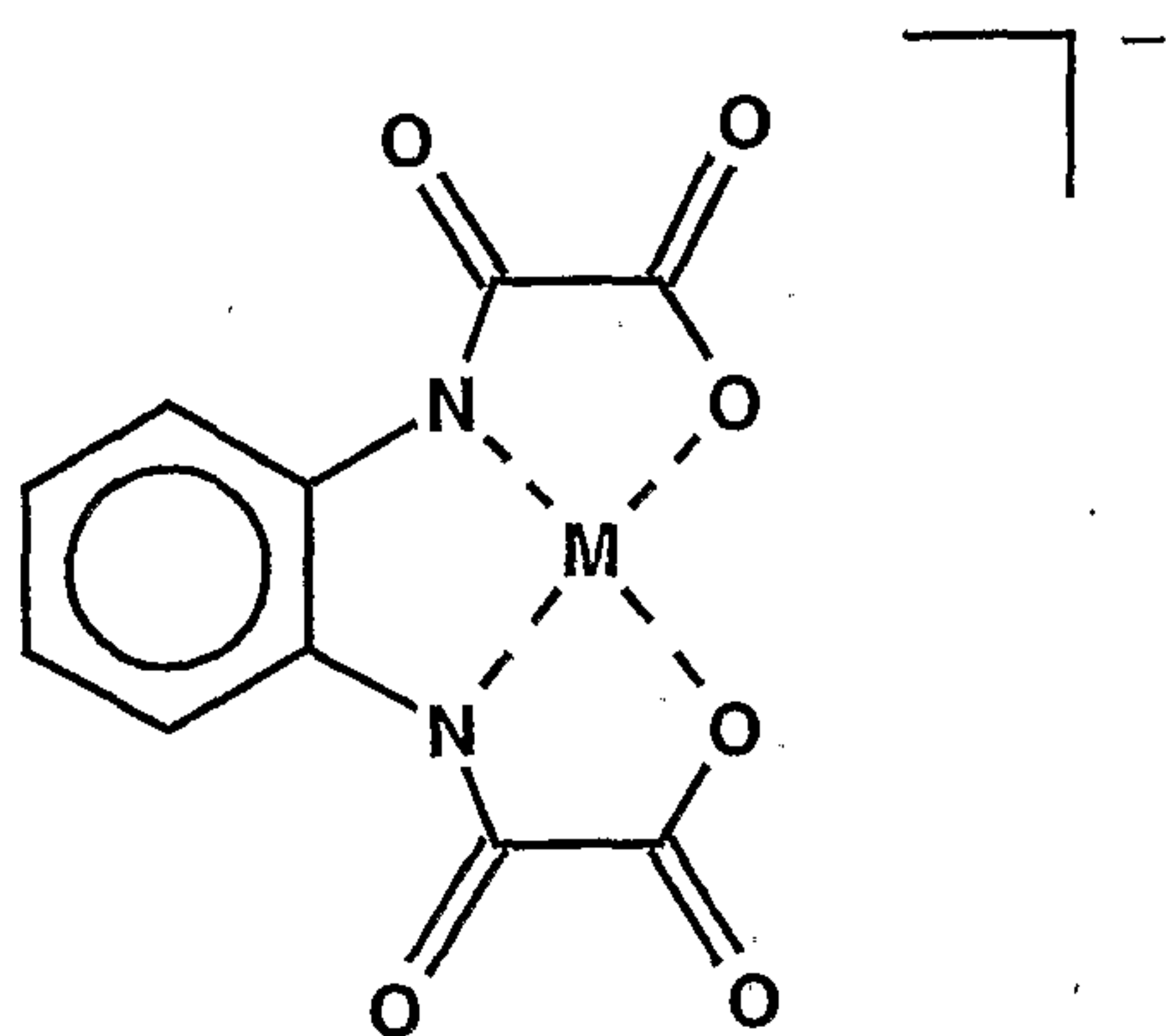
5,8,13,16-tetrahydro-5,8,13,16-tetraaza-
dibenzo[a,g]cyclododecene-6,7,14,15-tetraone (TTBP)

30

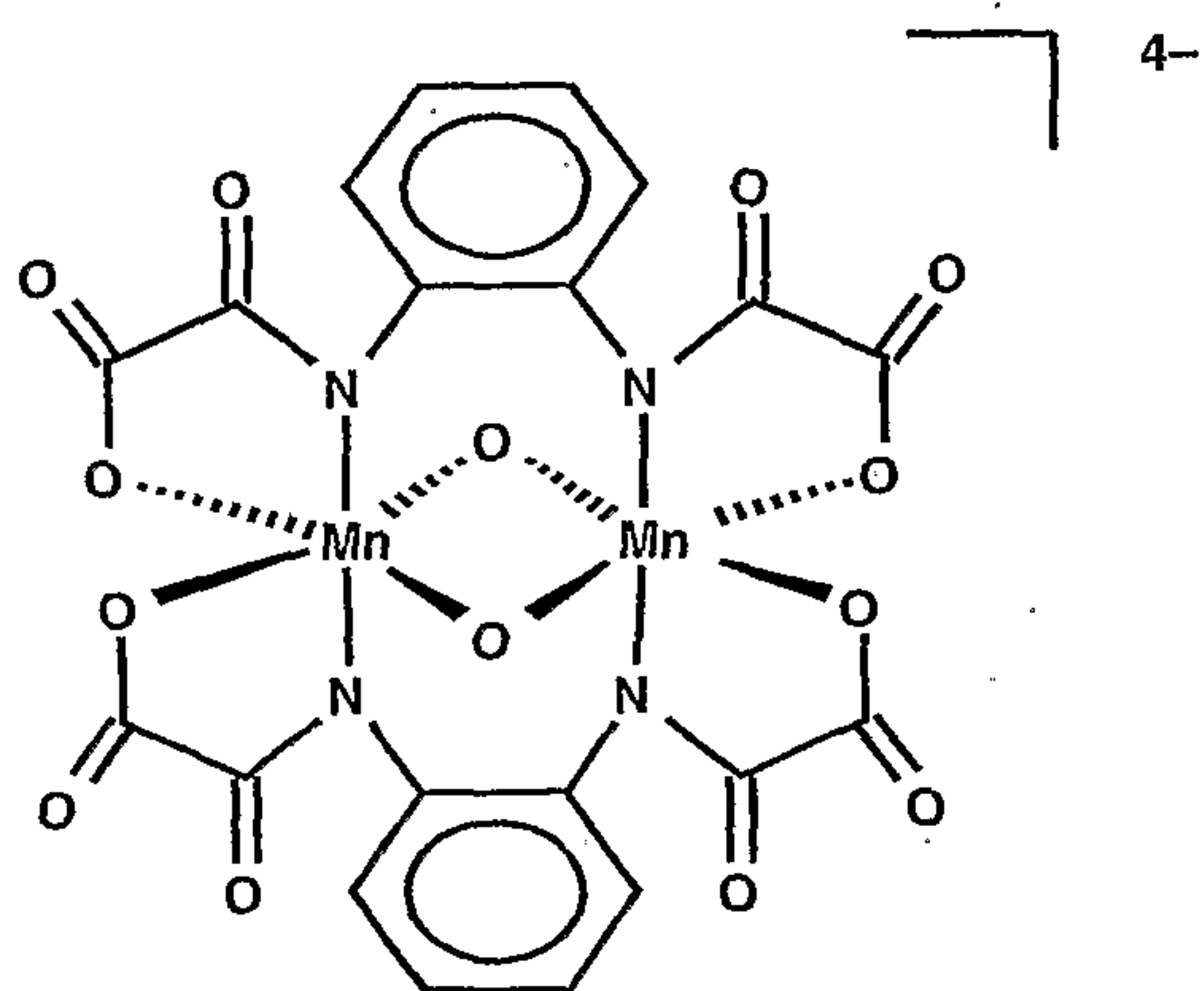
10



1,2-phenylene-bisoxamic acid (OPBA)



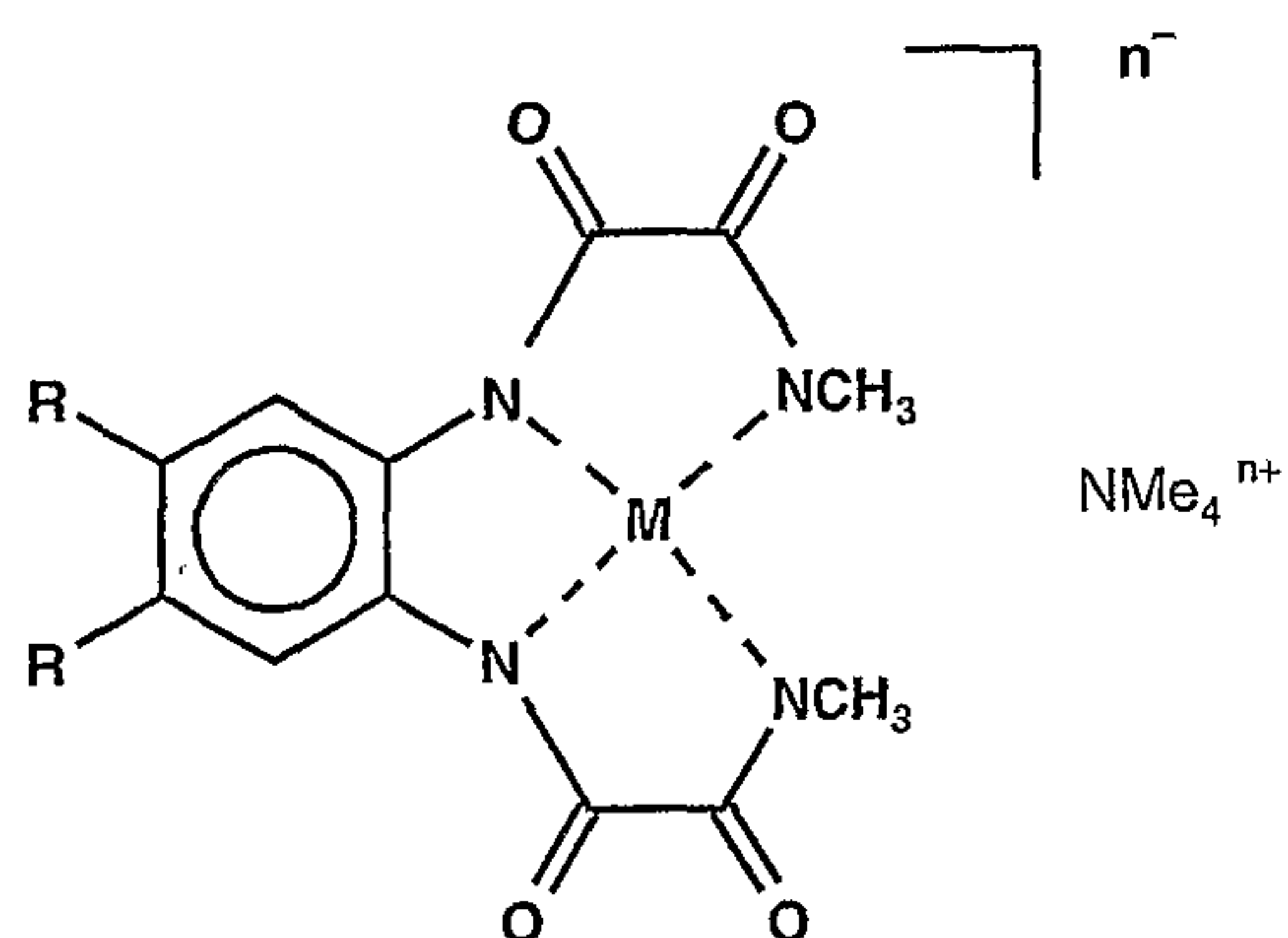
Mn complex of 1,2-phenylene-bisoxamic acid



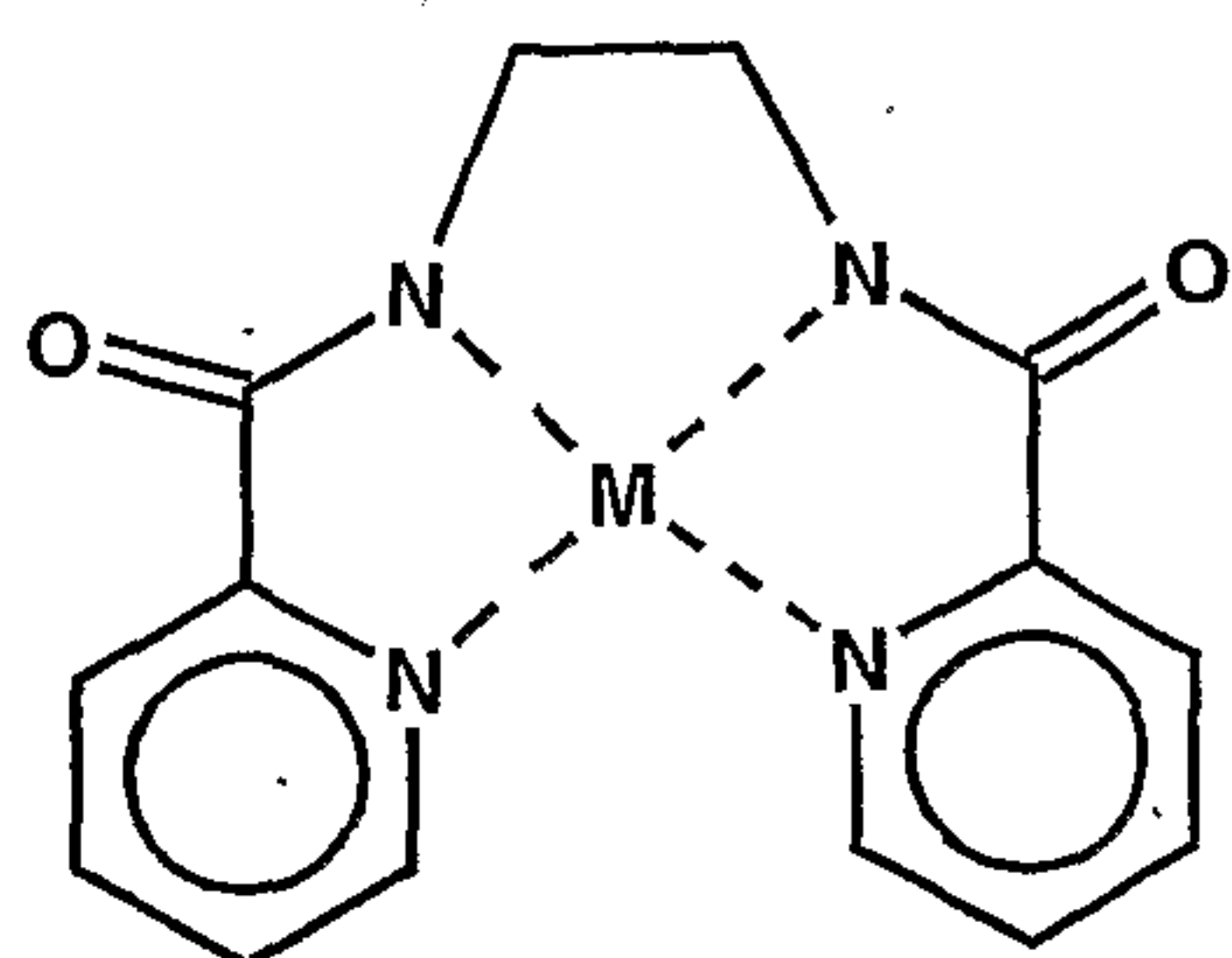
5

N-methyl-N'-[2-(methylaminooxalylamino)phenyl]oxalamide
(PBOMA)N-[4,5-dichloro-2-(methylaminooxalylamino)phenyl]-N'-
methyloxalamide (for R = Cl)

11



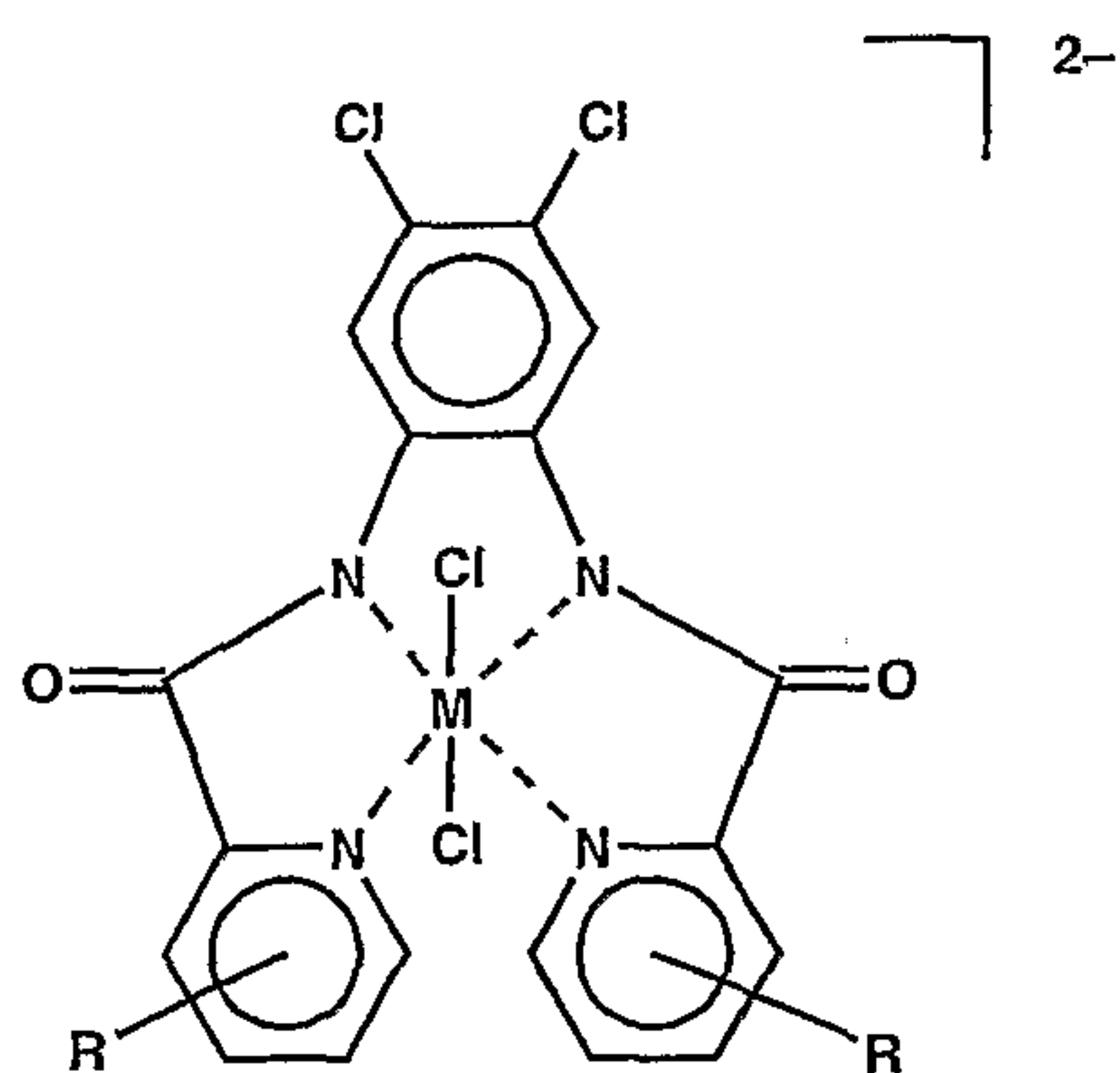
N,N' -bis(pyridine-2-carboxamido)-1,2-ethane (BPEN)



5

1,2-bis(pyridine-2-carboxamido)-4,5-dichlorobenzene (PCADB)

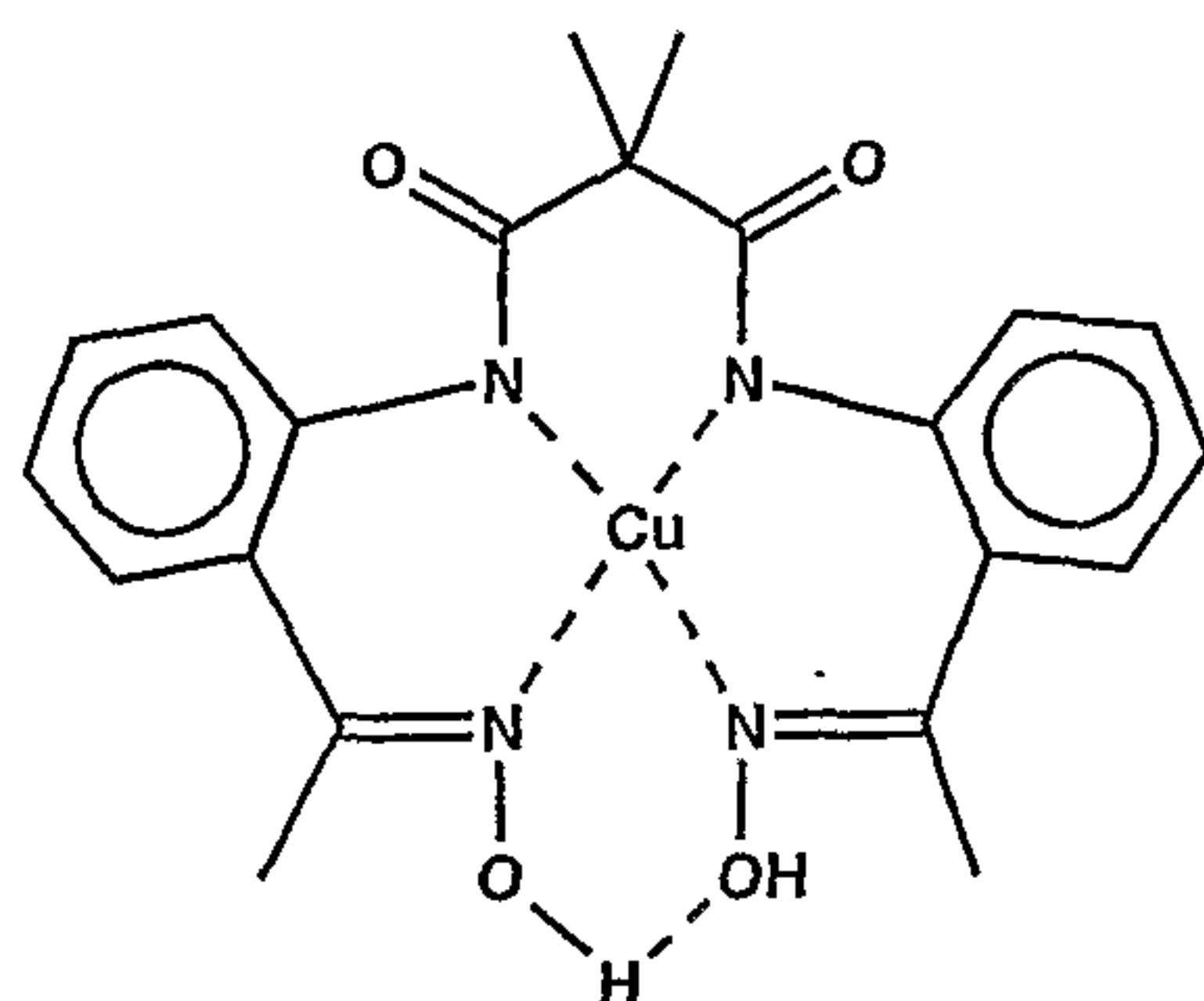
1,2-bis(4-*tert*-butylpyridine-2-carboxamido)-4,5-dichlorobenzene (for $R = tBu$)



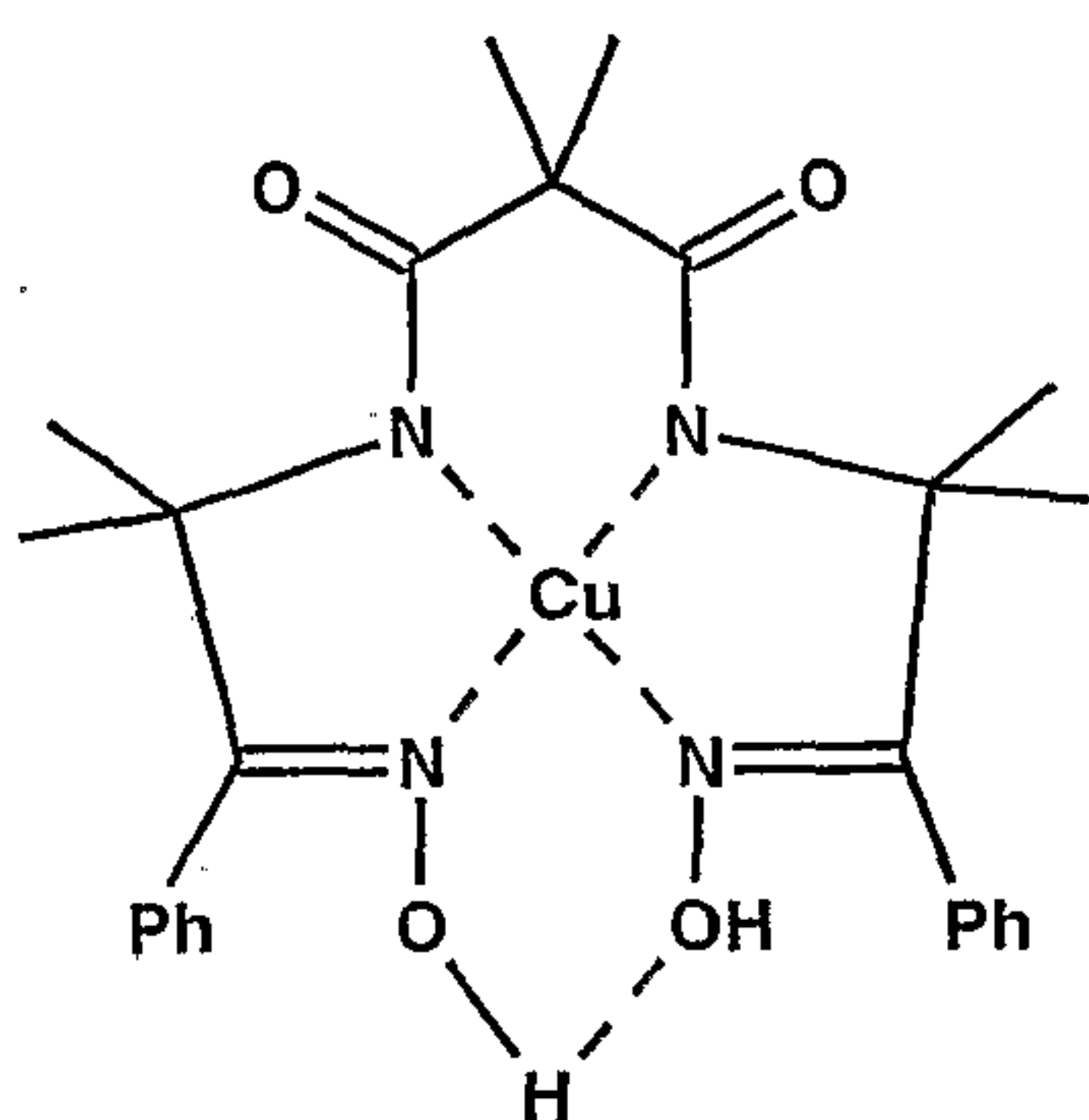
10

N,N' -bis[2-(1-hydroxyiminoethyl)phenyl]-dimethylmalonodiamide

12.



N,N'-bis[2-(2-methyl-1-oxo-1-phenyl)propyl]-
dimethylmalonodiamide



5

Apart from the ligand L, the catalyst can additionally contain coordinating co-ligands X. X here can be a mono-, di- or trivalent anion or a neutral molecule, which can be coordinated with the transition metal in a mono-, bi- or tridentate manner. The co-ligand is preferably the following groupings: OH^- , O^{2-} , NO_3^- , PO_4^{3-} , CN^- , SCN^- , HSO_4^- , SO_4^{2-} , Cl^- , Br^- , F^- , ClO_4^- , OCN^- , HCO_3^- , RS^- , CO_3^{2-} , SO_3^{2-} , RSO_3^- , $\text{S}_2\text{O}_6^{2-}$, RCO_2^- ; H_2O , ROH , CH_3CN , $\text{NRR}'\text{R}''$.

15

The counter-ion Y of the complex to be used can be anionic or cationic, wherein the number p is chosen such that complete charge compensation is achieved. The counter-ion can preferably have the following meaning: F^- , Cl^- , Br^- , I^- , NO_3^- , RSO_3^- (R e.g. preferably CF_3), ClO_4^- , RCO_2^- , PO_4^{3-} ,

20

HPO_4^{2-} , H_2PO_4^- , SO_4^{2-} , HSO_4^- , CO_3^{2-} , HCO_3^- , BF_4^- , PF_6^- , SO_3^{2-} ; Li^+ , Na^+ , K^+ , Mg^{2+} , Ca^{2+} , Ba^{2+} .

The bleaching catalysts to be used according to the invention activate elemental oxygen and peroxy compounds. Peroxy compounds are to be understood as meaning, in particular, hydrogen peroxide, compounds which liberate hydrogen peroxide, such as, in particular, sodium perborate monohydrate, sodium perborate tetrahydrate and sodium percarbonate, perphosphates and persulfates, peroxydicarboxylic acids and salts thereof and peroxydicarboxylic acid bleaching precursors, so-called activators, and mixtures of such substances. Suitable peroxydicarboxylic acids can be aliphatic or aromatic in nature and contain one or more peroxydicarboxylic acid groups. Aliphatic peroxydicarboxylic acids usually contain 1 to 20 C atoms, preferably 1 to 12 C atoms, and the particularly preferred peroxydicarboxylic acid is peroxyacetic acid. Among the peroxydicarboxylic acids with 2 peroxydicarboxylic acid groups, those having 4 to 18 C atoms are preferred; examples are diperoxyadipic acid, diperoxyazelaic acid, diperoxydodecanedioic acid, as well as salts of the acids mentioned, for example magnesium salts. Among the aromatic peroxydicarboxylic acids there are, in particular, peroxybenzoic acid, m-chlorobenzoic acid, p-sulfonatoperoxybenzoic acid, diperoxyisophthalic acid, phthalimidopercaproic acid, 4,4'-sulfonyl-diperoxybenzoic acid and magnesium salts of these acids.

30

The peroxydicarboxylic acids can also be formed in situ under the use conditions, and in particular from so-called activators, which are in general O-acyl compounds and N-acyl compounds. Such compounds form the corresponding

peroxycarboxylic acid under perhydrolysis conditions in the presence of hydrogen peroxide or a source of hydrogen peroxide. Activators which are particularly preferably to be used are: N,N,N'-tetraacetylenediamine (TAED), Na
5 1-methyl-2-benzoyloxybenzene-4-sulfonate, Na nonanoyloxybenzenesulfonate (NOBS), 2-(N,N,N-trimethylammonium)ethyl-sodium 4-sulfophenylcarbonate chloride (SPCC), pentaacetylglucose, phthalic anhydride.

10 For activation of peroxy compounds, the transition metal complexes to be used according to the invention are in general employed in an amount of about 0.0001 to 50 wt.%, in particular 0.01 to 20 wt.% and particularly preferably 0.01 to 1 wt.%, based on the peroxy compounds.

15

Bleaching agent compositions according to the invention comprise at least one peroxy compound and a transition metal complex to be used according to the invention in an active amount. Such compositions expediently comprise 0.001
20 to 50 wt.%, in particular 0.01 to 20 wt.% and particularly preferably 0.01 to 1 wt.% of a transition metal complex with a ligand according to the invention, based on the content of peroxy compounds or precursor of one.

25 Bleaching agent compositions according to the invention expediently additionally comprise one or more surfactants from the series consisting of anionic, cationic, zwitter-ionic and nonionic surfactants, in particular surfactants such as are used in conventional washing, bleaching and
30 cleaning compositions. Bleaching agent compositions according to the invention can furthermore also comprise organic and/or inorganic builders, such as zeolites. Further constituents can be those such as are used in

conventional washing, bleaching and cleaning compositions, including enzymes, pH regulators and conventional alkali metal carriers, such as alkali metal silicate and alkali metal carbonates.

5 Examples

Example 1:

Preparation of the dibenzotetramide 5,8,13,16-tetrahydro-5,8,13,16-tetraaza-dibenzo[a,g]cyclododecene-6,7,14,15-tetraone (TTBP)

- 10 Ligand: A solution of 5.52 g (17.9 mmol) diethyl 1,2-phenylene-dioxamate (preparation in accordance with: J. Am. Chem. Soc. 1993, 115(15), 6738) and 1.94 g (17.9 mmol) 1,2-phenylenediamine in 250 ml toluene was heated under reflux for 8 hours. The product was then filtered off and dried in
15 vacuo at 50°C. Yield: 29% (pale green solid).

- M complex (M = Fe, Cu, Mn, Co): 500 mg (1.54 mmol) of ligand were dissolved in 50 ml THF under argon and the solution was then cooled to -100°C. 4.2 ml (6.17 mmol) n-
20 butyllithium (15 per cent in pentane) were added all at once by means of a disposable syringe and, after 15 minutes, 195 mg (1.54 mmol) anhydrous iron(II) chloride were added. The reaction mixture was warmed to room temperature and stirred at this temperature for 22 hours.
25 Atmospheric oxygen was then passed through the solution in the course of 2 hours. The red-brown solid was filtered off and dried at 50°C in vacuo. Yield: 96%

- Analogously, the Mn complex was prepared with anhydrous MnCl₂ (42%, red-brown solid), the Cu complex with anhydrous
30 CuCl₂ (70%, dark brown solid) and the Co complex with anhydrous CoCl₂ (83%, dark red solid).

Example 2:

Preparation of N-methyl-N'-[2-(methyaminooxalylamino)-phenyl]oxalamide (PBOMA)

N,N'-1,2-Phenylene-bis(oxamic acid ethyl ester)

5 8.40 g (60.0 mmol) ethoxalyl chloride were added dropwise to a solution of 3.30 g (30.0 mmol) 1,2-phenylenediamine in 150 ml tetrahydrofuran analogously to the instructions in *J. Am. Chem. Soc.* 1993, 115(15), 6738. The solution was heated under reflux for 0.5 hour and solid constituents
10 were then filtered off. After distillation of the solvent, a little water was added to the oily residue, a colourless solid precipitating out. This was filtered off, washed with water and dried in vacuo. (Yield: 97%)

15 Reaction of the diester with methylamine

8.24 g (87.5 mmol) methylamine (33% in methanol) were added dropwise to a solution of 9.00 g (29.2 mmol) of the diethyl ester in 50 ml ethanol analogously to the instructions in *J. Chem. Soc. Dalton Trans.* 1997, 745 at room temperature
20 and the reaction solution was then stirred vigorously for 0.5 hour at 65°C. The colourless solid was filtered off, washed with a little cold methanol and methyl tert-butyl ether and dried in vacuo. (Yield: 82%)

25 Co complex of PBOMA:

2.62 g (7.18 mmol) cobalt(II) perchlorate dihydrate, which were dissolved in a little methanol beforehand, were added to 2.00 g (7.18 mmol) of the bisamide PBOMA and 11.0 g (30.2 mmol) tetramethylammonium hydroxide in 10 ml
30 methanol. A pale red solid precipitated out. This was filtered off and dried. (Yield: 84%)

Examples 3 to 8

The complexes of examples 1 and 2 and complexes prepared in an analogous manner or a manner known from the literature were investigated for their catalytic action by means of the Morin test and in some cases by means of a washing test.

Morin test: A sodium perborate monohydrate solution, a methanolic solution of tetraacetythylenediamine and a dilute solution of the combination to be investigated are added to an aqueous Morin solution.

After intensive mixing, the extinction/transmission is measured at 400 nm after 30 minutes at 30°C. The blank value is measured in the absence of the combination to be investigated.

Washing test: Laboratory washing apparatus type ATLAS LAUNDER-O-METER

Temperature: 30 °C

Washing time: 30 minutes

Water hardness: 14°d

Staining: tea, in some cases also grass on cotton

Detergent recipe:

12.2% anionic surfactant

7.7% nonionic surfactant

2.0% soap

34.8% zeolite A

4.2% polycarboxylate

0.5% phosphonic acid

4.1% corrosion inhibitor

1.1% magnesium silicate

1.1% greying inhibitor (CMC)

2.2% sodium sulfate

4.1% sodium citrate

Bleaching component:

5 17% sodium percarbonate

5% activator TAED

Metal complex: 2,400 ppm

Detergent concentration: 5 g/l

10 As a comparison, the base recipe plus percarbonate/TAED,
but without a metal complex (= catalyst) was always run
(CE1). This change in reflection compared with the starting
fabrics is subtracted from the change in reflection
achieved with percarbonate/TAED/bleaching catalyst.

The results follow from the table:

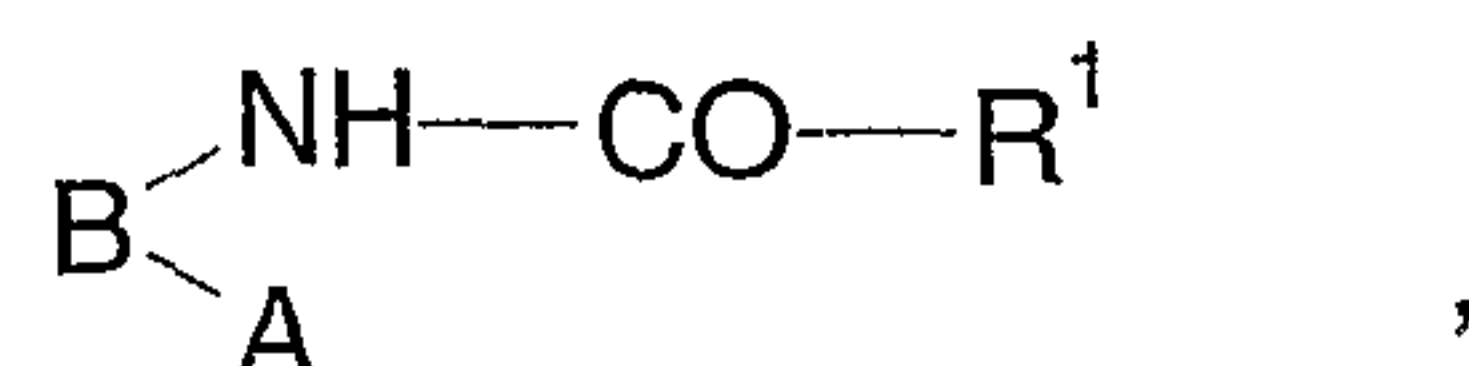
Table:

No.	Complex			Morin test transmission	Washing test (ΔR)
	M	L	X or Y		
3	Co	TTBP		94.8	0.2
4	Co	PBOMA	$Y=N(CH_3)_4^+$	94.8	1.9
5a	Co	OPBA		13	1.5
5b	Cu	OPBA		13.8	n.d.
5c	Fe	OPBA		5.8	n.d.
6	Mn	OPBA	$X=(\mu O)_2$ $Y=(Na^+)_4$	4.2	n.d.
7	Mn	BPEN		8	n.d.
8a	Co	PCADB	$X=(Cl^-)_2$ $Y=(Na^+)_4$	6.2	n.d.
8b	Fe	PCADB	$X=(Cl^-)_2$ $Y=(Na^+)_4$	46	n.d.

The test results show that the catalysts according to the invention, in particular cobalt complexes, lead to a high increase in the activity of the peroxyacetic acid formed in situ from an activator (TAED) and perborate.

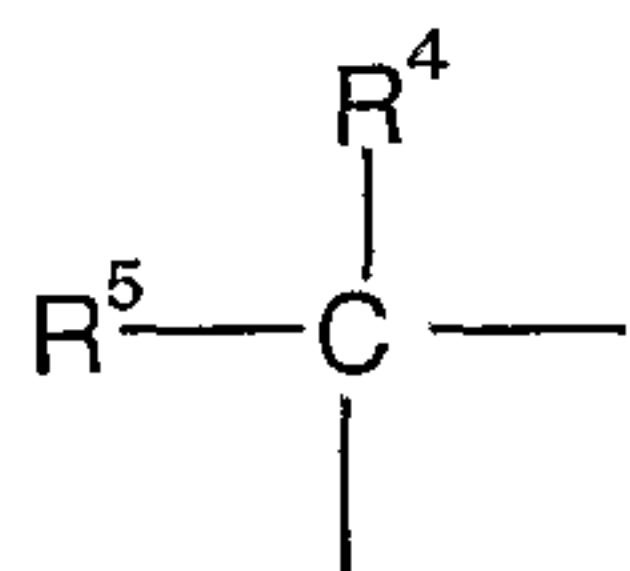
Patent claims:

1. Use of a transition metal complex with at least one nitrogen-containing polydentate ligand as a bleaching catalyst for activation of a peroxy compound or of oxygen, wherein the complex is mono- or polynuclear, the transition metal (M) is manganese, iron, cobalt or copper and the nitrogen-containing polydentate ligand (L), at least one of which is present, has the general formula (I)

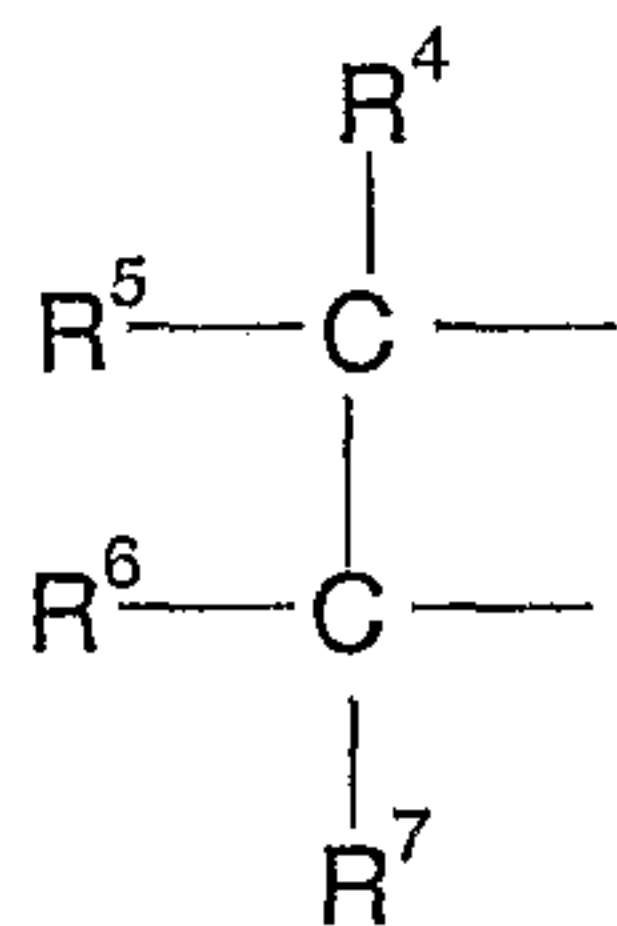


- 10 wherein A represents either the group $-\text{NH}-\text{CO}-\text{R}^2$ or the group $-\text{C}=\text{N}-\text{OZ}$,
 $\begin{array}{c} | \\ \text{R}^3 \end{array}$

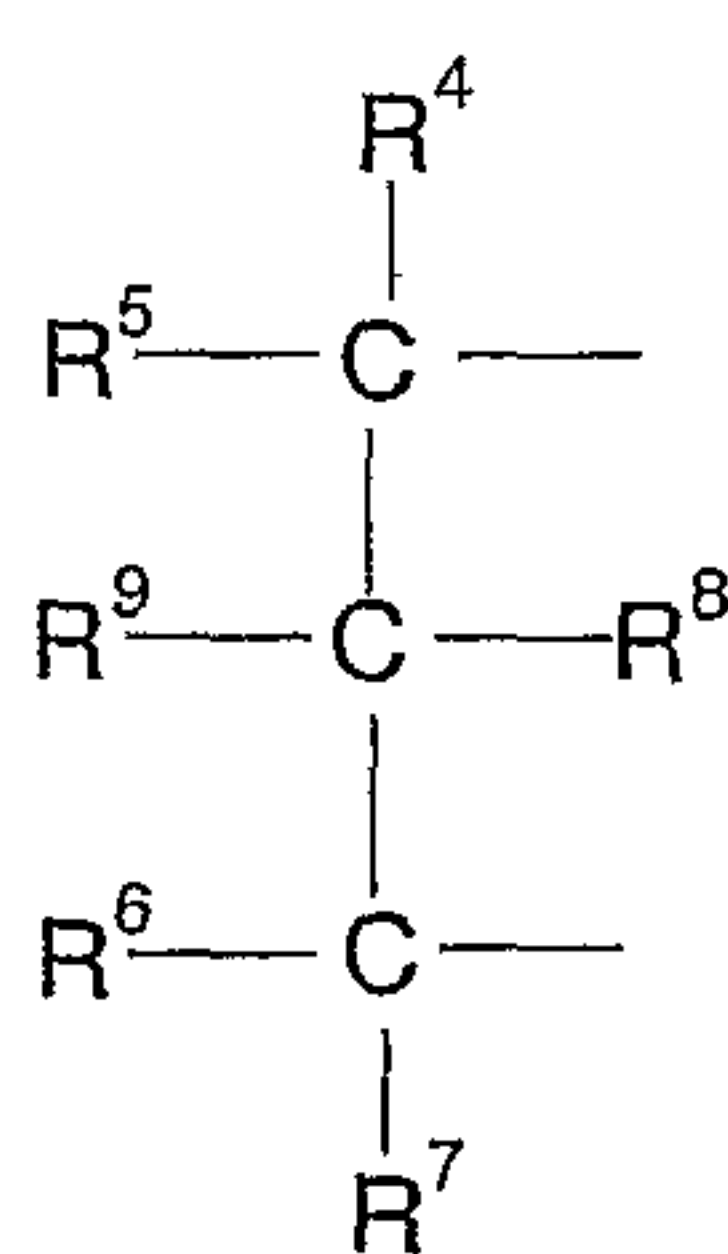
the bridge member B is chosen from the series consisting of



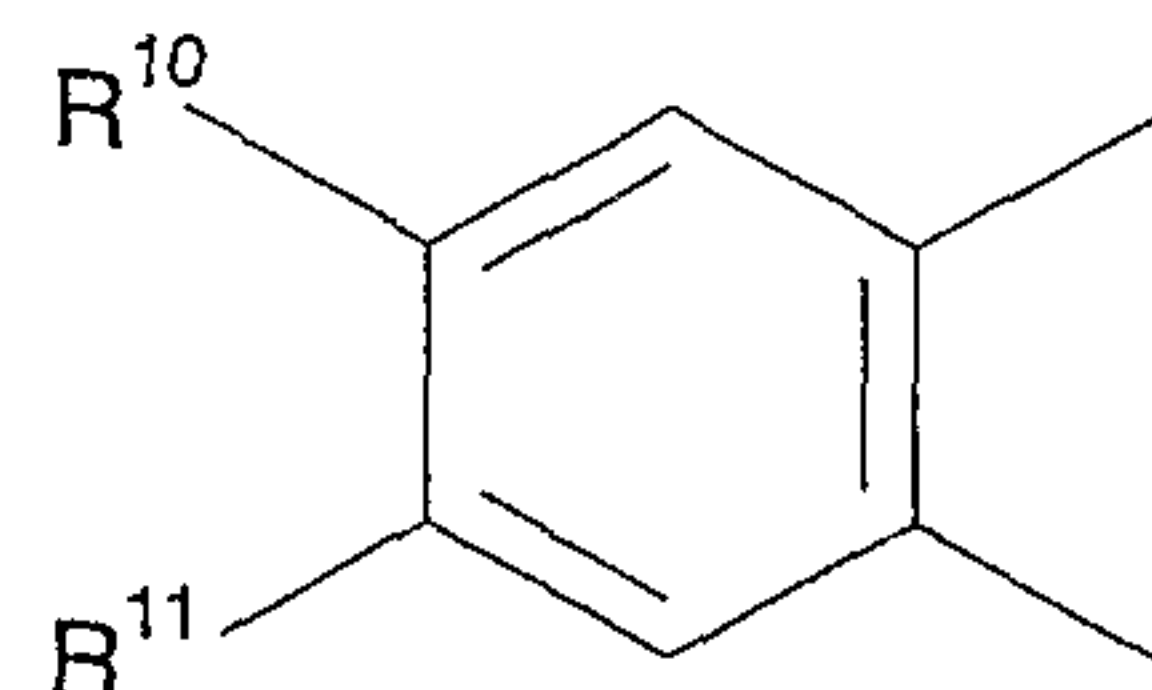
(B0)



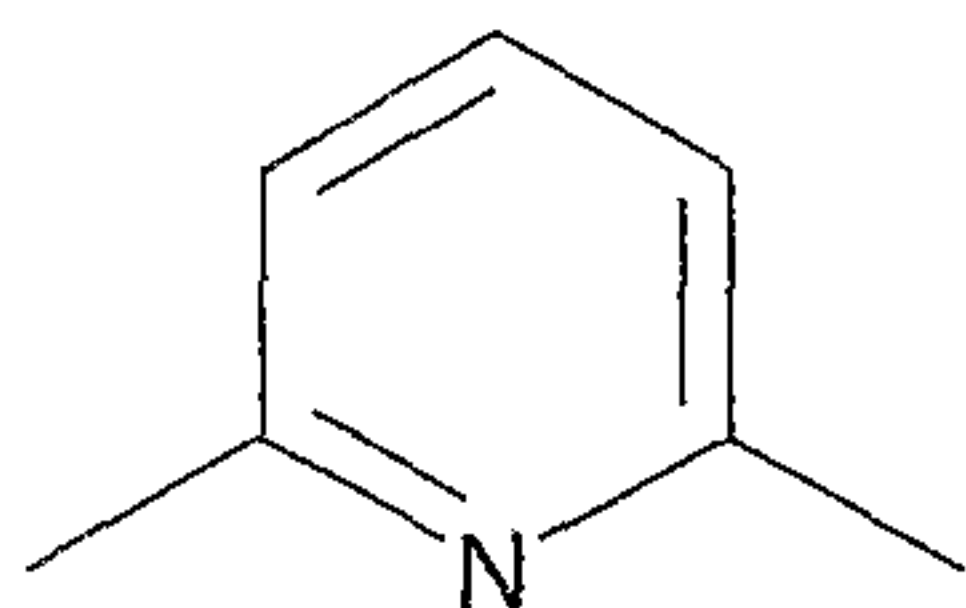
(B1)



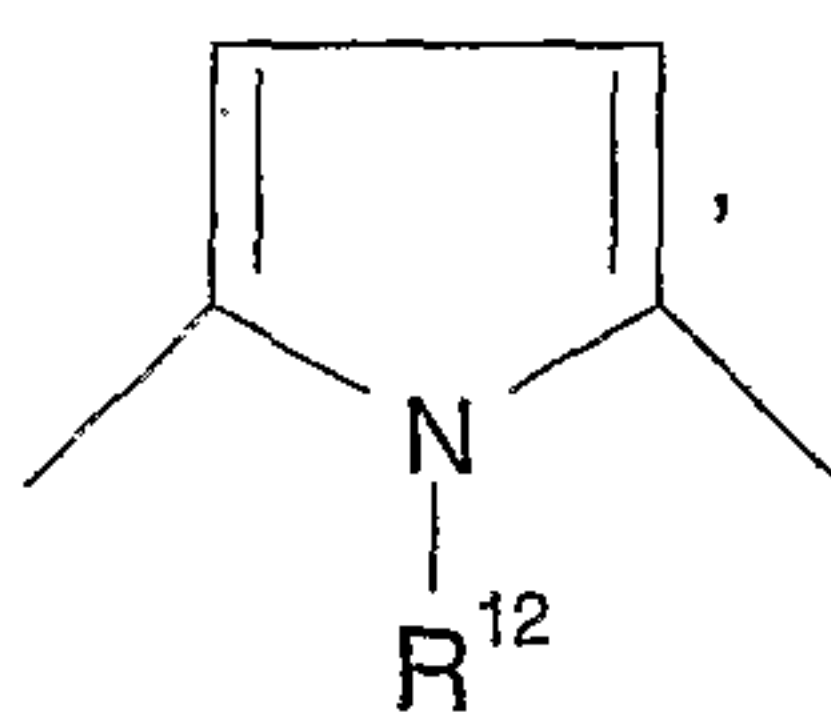
(B2)



(B3)

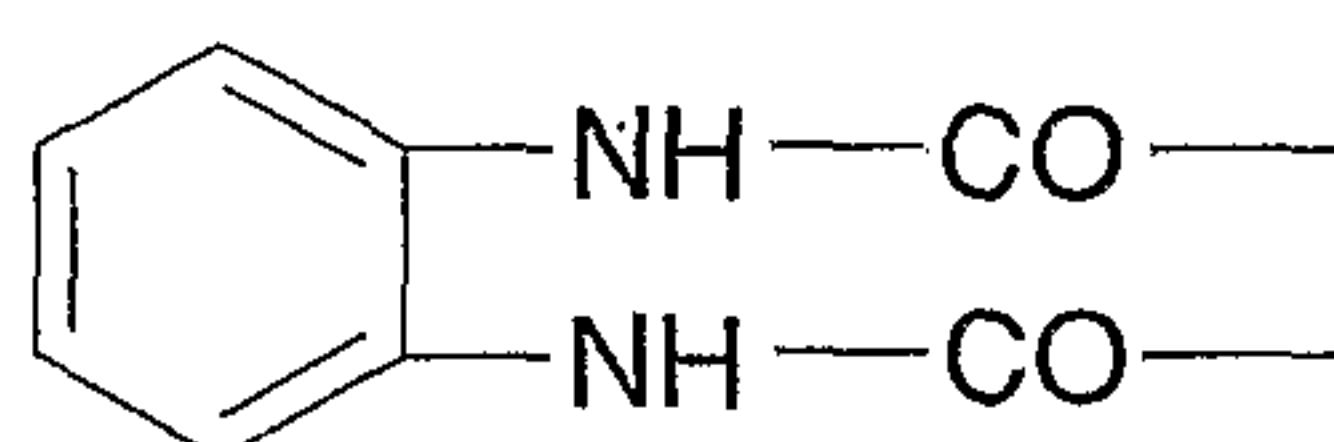


(B4)

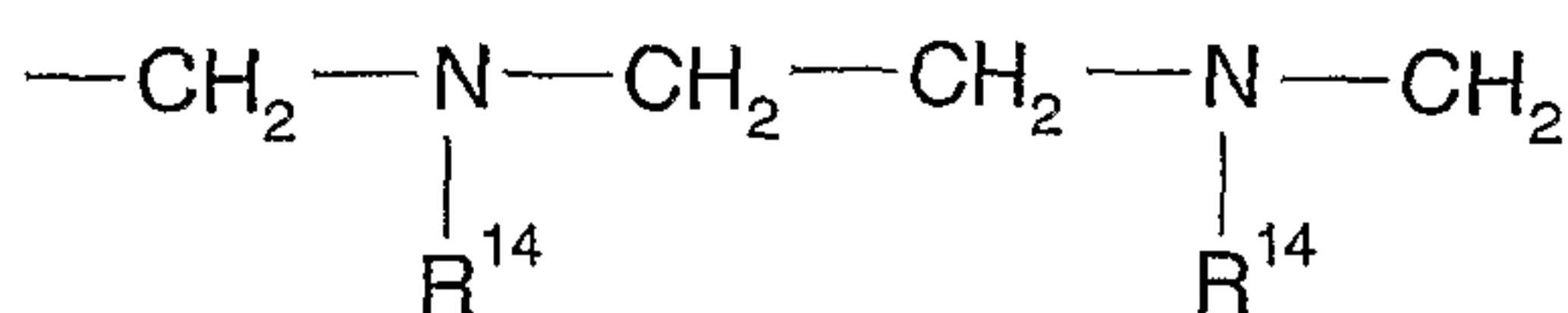


(B5)

wherein R^4 to R^7 independently of one another represent a radical from the series consisting of H, arylalkyl, aryl, heteroaryl, wherein R^4 with R^5 or/and R^6 with R^7 or R^4 with R^6 together with the atom(s) carrying them can form a five- to seven-membered cycloaliphatic or O- or N-heterocyclic ring, which can also contain a double bond, and wherein the structural elements of the general formulae (B0) to (B5) have a total of 2 to 20 C atoms, R^8 and R^9 independently of one another can represent a radical from the series consisting of H, methyl or together can represent carbonyl oxygen, R^{10} and R^{11} independently of one another can represent a radical from the series consisting of H, (C_1-C_4) alkyl, halogen or together can represent a fused-on aromatic ring and R^{12} can represent H or methyl, the radicals R^1 and R^2 independently of one another can represent a radical from the series consisting of $-COOH$, $-CONH_2$, $-CONHR^{13}$, $C(CH_3)_2OH$, 2-pyridyl, 1,3-oxazolin-2-yl, imidazol-2-yl or R^1-R^2 together can represent the radical

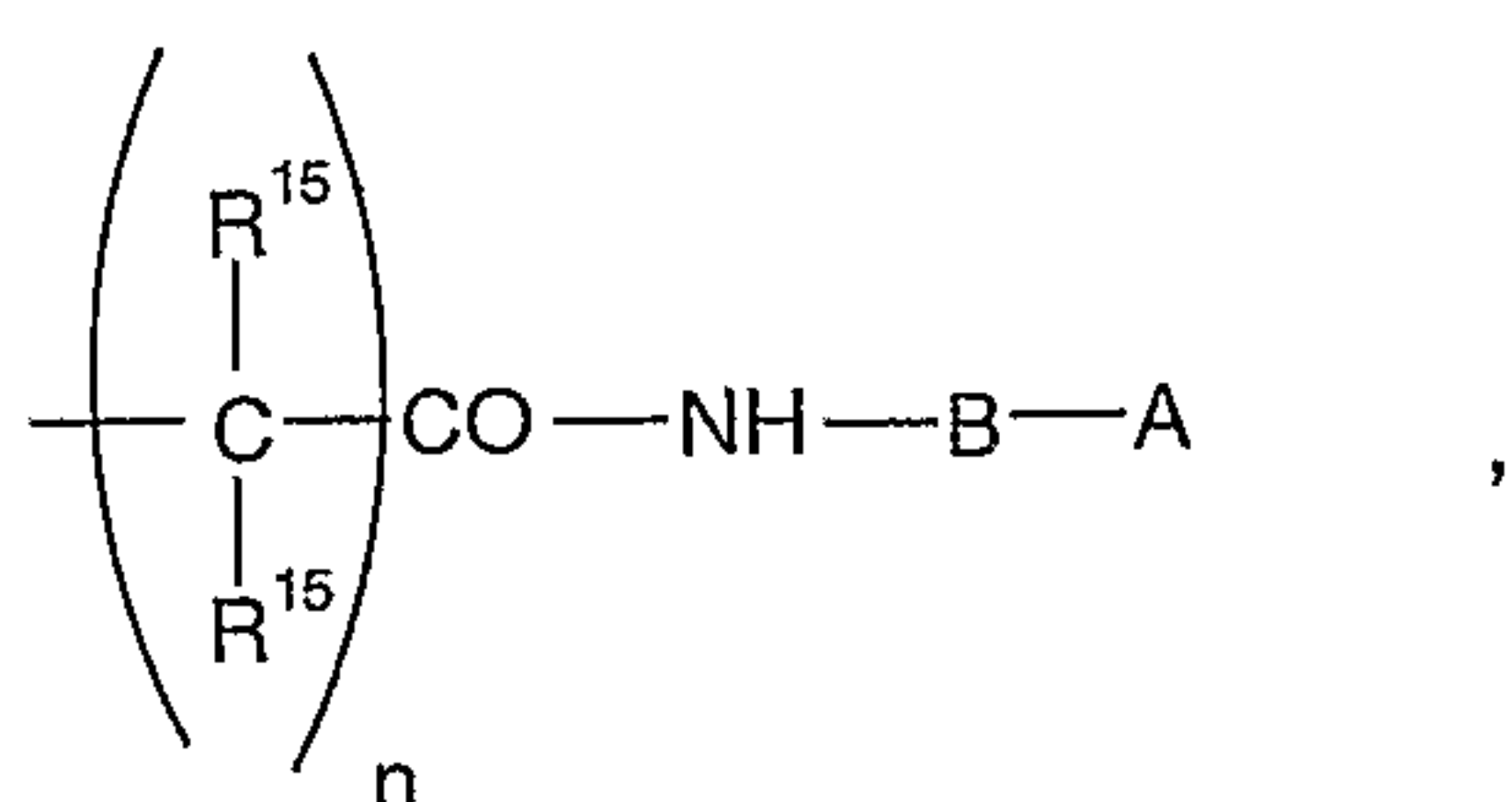


or



wherein R^{13} can be chosen from the series consisting of linear, branched or cyclic alkyl, aryl, heteroaryl, in particular 2-pyridyl, 1,3-oxazolin-2-yl and imidazol-2-yl and heteroalkylmethyl, R^{14} can be chosen from the series consisting of substituted or unsubstituted, linear, branched or cyclic

alkyl, benzyl, aryl, heteroaryl, heteroarylmethyl, and
 R^3 represents a radical from the series consisting of
 alkyl, aryl, heteroaryl, arylalkyl, heteroarylalkyl and
 Z represents H, alkyl, aryl, dialkylaminoethyl,
 5 heteroaryl
 and in the case of the oximes R^1 additionally can
 represent the radical



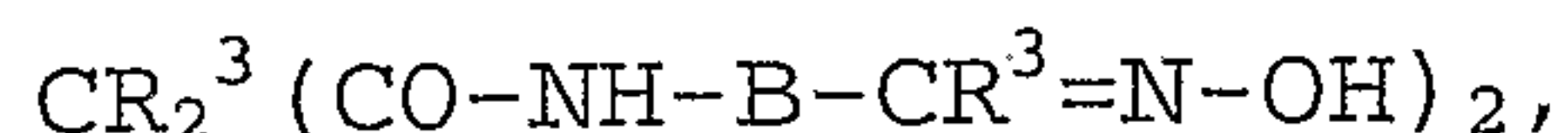
wherein n is 0 or 1, R^{15} can be H or alkyl and $R^{15}-C-R^{15}$
 10 can be cycloalkyl.

2. Use according to claim 1,
 characterized in that
 the ligand L has the general formula



15 wherein B represents unsubstituted or substituted ortho-
 phenylene, wherein the substituents can be bonded in
 particular in the 4,5-position and can be Cl; F or CH_3 ,
 and/or R^1 is chosen from the series consisting of $COOH$,
 $CO-NH-CH_3$, $C(CH_3)_2OH$, 2-pyridyl, 1,3-oxazolin-2-yl and
 20 imidazol-2-yl or R^1 represents a radical from the series
 consisting of phenylenediamine-N,N'-dicarbonyl or
 $CH_2-N-CH_2-CH_2-N-CH_2-$, where R^{14} is $-CH_2-COOH$.

3. Use according to claim 1 or 2,
 25 characterized in that
 the ligand L in the diamide-dioxime corresponds to the
 general formula



wherein B represents substituted ortho-phenylene and R^3 represents methyl.

4. Use according to one of claims 1 to 3
 5 characterized in that
 the complex has the general formula $[\text{L}_m\text{M}_n\text{X}_o]\text{Y}_p$,
 wherein L denotes a ligand according to one of claims 1
 to 6
 M denotes a transition metal from the series consisting
 10 of Mn(II) to Mn(IV), Fe(II), Fe(III), Co(II), Co(III),
 Cu(I) and Cu(II), in particular Co(II) or Co(III),
 X denotes a coordinating neutral or charged mono- or
 polyvalent ligand for saturation of the ligand sphere
 and
 15 Y denotes a non-coordinating counter-ion which can be
 anionic or, if the sum of anionic substituents in the
 ligand L exceeds the sum of the valency of the metal
 atoms M, can also be cationic,
 m denotes an integer in the range from 1 to 4, in
 20 particular 1 or 2,
 n denotes the number 1 or 2,
 o denotes zero or an integer in the range from 1 to 8
 and
 p denotes zero or an integer in the range from 1 to 8,
 25 in order to achieve complete charge compensation.

5. Use according to claim 4,
 characterized in that,
 a complex of the general formula $[\text{LMX}_o]\text{Y}_p$ or $[\text{L}_2\text{M}_2\text{X}_o]\text{Y}_p$,
 wherein the bridge member B of the ligand $\text{B}(\text{NH}-\text{CO}-\text{R}^1)_2$
 30 denotes ortho-phenylene or 4,5-dichlorophenylene and R^1
 denotes a radical from the series consisting of COOH,
 CONHCH_3 , $\text{C}(\text{CH}_3)_2\text{OH}$ and 2-pyridyl, is employed.

6. Use according to one of claims 1 to 5,
 characterized in that

hydrogen peroxide or a peroxycarboxylic acid having 2 to 18 C atoms, which can also have been formed in situ from a source of hydrogen peroxide and an activator from the series consisting of O-acyl or N-acyl compounds, is
5 activated.

7. Use according to one of claims 1 to 6 characterized in that the transition metal complex is employed in an amount of 0.0001 to 50 wt.%, based on the peroxy compound.

10 8. Bleaching agent composition comprising a peroxy compound and a transition metal complex in an amount effective for activation of the peroxy compound, characterized in that it comprises a transition metal complex according to one
15 of claims 1 to 5.

9. Bleaching agent composition according to claim 8, characterized in that the peroxy compound is chosen from the series consisting of hydrogen peroxide, a source of hydrogen peroxide, in
20 particular an alkali metal perborate monohydrate tetrahydrate or alkali metal percarbonate, a peroxycarboxylic acid having 2 to 18 C atoms or a combination of a source of hydrogen peroxide and a peroxycarboxylic acid precursor, in particular an O-acyl
25 or N-acyl compound, or from mixtures thereof.

10. Bleaching agent composition according to claim 8 or 9, characterized in that it additionally comprises one or more surfactants, in particular wash-active surfactants.

30 11. Bleaching agent composition according to one of claims 8 to 10, characterized in that

it additionally comprises builders, in particular zeolites.

12. Bleaching agent composition according to claim 10 or 11,

5 characterized in that

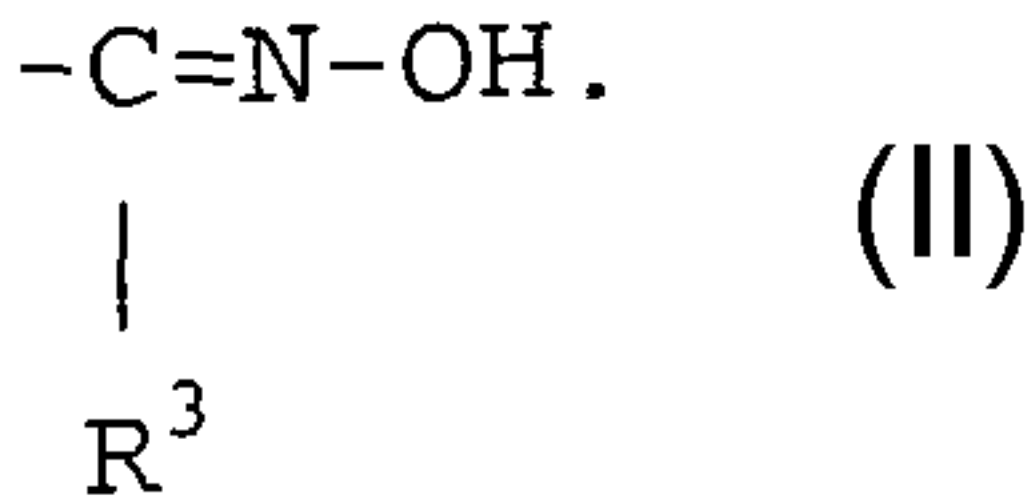
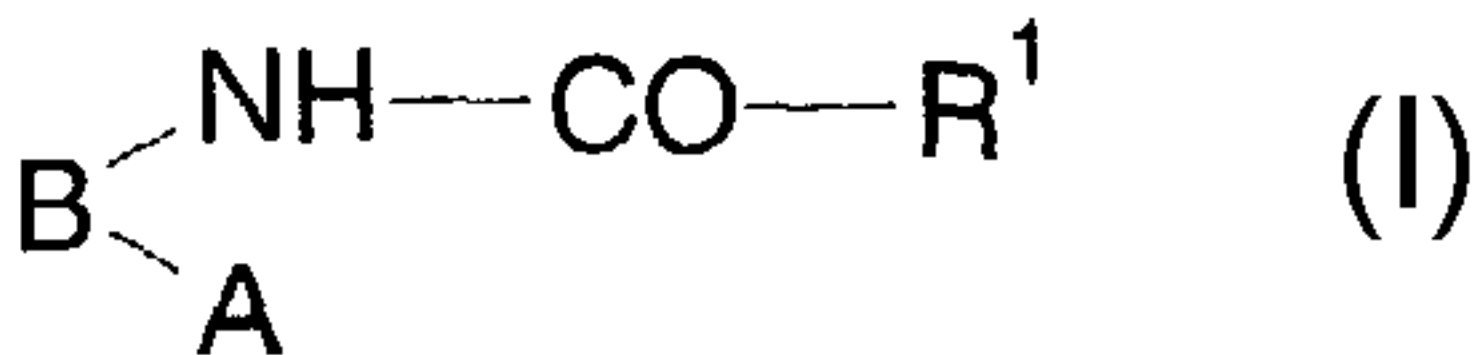
it is a constituent of a washing, bleaching or cleaning composition comprising one or more surfactants and one or more builders.

13. Bleaching agent composition according to one of claims 8 to 12,

10 characterized in that

it comprises 0,0001 to 50 wt.%, in particular 0.01 to 20 wt.% of a transition metal complex according to one of claims 1 to 7, based on the content of peroxy compound or precursor thereof.

15



PAPER

[View Article Online](#)
[View Journal](#) | [View Issue](#)

Study of the scale-up, formulation, ageing and ammonia adsorption capacity of MIL-100(Fe), Cu-BTC and CPO-27(Ni) for use in respiratory protection filters†

S. Hindocha  and S. Poulston*

Received 3rd March 2017, Accepted 24th March 2017

DOI: 10.1039/c7fd00090a

The metal–organic frameworks (MOFs) MIL-100(Fe), Cu-BTC and CPO-27(Ni) were synthesised in 1 kg batches. The materials were then formed in two different industrially relevant ways. Firstly, dry granulation was used to produce pellets which were sieved to give material with a 300–1000 μm size, and the fines were subsequently recycled to mimic a large scale industrial process. Secondly, wet granulation with a polymer was used to produce granules which were again sieved to 300–1000 μm . XRD data shows that the structures of MIL-100(Fe) and CPO-27(Ni) remain intact during both forming processes, whilst Cu-BTC is shown to degrade during processing. This is in line with the ammonia adsorption data obtained for the formed materials which evaluated the ammonia adsorption capacity of the materials using breakthrough measurements. MIL-100(Fe) and CPO-27(Ni) are shown to have capacities of 47 mg g^{-1} and 62 mg g^{-1} respectively whilst Cu-BTC has a decreased capacity of 37 mg g^{-1} from 97 mg g^{-1} upon forming. The formed materials were also aged at 25 $^{\circ}\text{C}$ and 80% humidity for a week and the ammonia adsorption capacity re-evaluated. As expected, Cu-BTC decomposed under these conditions, whilst MIL-100(Fe) and CPO-27(Ni) show slightly decreased ammonia adsorption capacities of 36 mg g^{-1} and 60 mg g^{-1} respectively.

Introduction

The National Institute of Occupational Safety and Health (NIOSH) certifies respiratory filters for protection against a wide range of chemical gases, for example ammonia (NH_3), hydrogen sulphide (H_2S) and hydrogen chloride (HCl). Current respiratory protection filters use impregnated activated carbon to provide this broad-spectrum protection. Given the chemical variety of toxic gases it is no surprise that the adsorption performance of activated carbon varies across the gases. Impregnation of a range of inorganic and organic compounds with acidic

Johnson Matthey Technology Centre, Blount's Court Road, Sonning Common, RG4 9NH, UK. E-mail: stephen.poulston@matthey.com

† Electronic supplementary information (ESI) available. See DOI: 10.1039/c7fd00090a



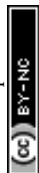
and basic functionality can result in limitations to the effectiveness of the material for individual toxic gas components. Though activated carbon can be optimised for a specific gas, it may not be the most effective means of removing some chemicals.

An alternative approach may be offered by the use of other adsorbent materials specifically targeted at individual gases which can allow for an overall improvement in the filter performance when combined with activated carbon.¹ The use of metal-organic frameworks (MOFs) for the adsorption of toxic gases has been investigated^{2,3} due to the tunability of the materials. MOFs provide highly porous structures into which specific functionality can be designed. The selection of metal centres and organic ligands allows materials to be produced with target applications in mind. As a result, MOFs have been investigated for a range of different applications including catalysis,⁴ gas storage,⁵ gas separations⁶ and toxic industrial chemical (TIC) degradation.⁷ For example, NU-1000 has been shown to catalytically degrade dimethyl-4-nitrophenyl phosphate.⁷ However, more commonly MOFs have been investigated as adsorbents for TIC removal in respiratory protection applications with a range of gases. The adsorption of hydrogen sulphide,⁸ chlorine,⁹ nitrogen oxide¹⁰ and ammonia¹¹ into MOF materials have all been studied and generally the incorporation of a specific chemical functionality aids adsorption.

The use of MOFs for the adsorption of ammonia in respiratory protection applications has been investigated in detail. Several reports have systematically investigated different MOFs for ammonia adsorption including the CPO-27/MOF-74 series of materials. This series allows for the investigation of ammonia adsorption onto different vacant metal sites without altering the topology of the MOF.¹² Other reports have used the UiO-66 series of materials to investigate how ligand functionality can impact the MOFs' ammonia adsorption capacity with functionalities that can hydrogen bond to ammonia, increasing material performance.¹³

The forming of MOFs into granules,¹⁴ extrudates¹⁵ and pellets¹⁶ has previously been reported, along with the effect the forming process has on the structure of the MOF and the surface area. The addition of a binder and the amount can also have an impact on the material properties.¹⁷

This paper aims to investigate three MOFs, MIL-100(Fe), Cu-BTC and CPO-27(Ni), which have been synthesised at a 1 kg scale¹⁸ and formed in industrially relevant processes. These three materials have previously been studied¹¹ for ammonia adsorption within the literature. Here they have been evaluated for ammonia adsorption capacity using breakthrough measurements, which are compared to an activated carbon currently used within respiratory protection filters. We present the performance of the materials whilst considering the commercial aspects of a respiratory protection product. This included forming the MOF to produce particles with a size range of 300–1000 μm . Testing of the formed materials was completed under conditions appropriate for this application: humid conditions, relevant space velocity and challenge concentrations. The formed samples were aged in conditions comparable to those in the NIOSH specifications to investigate the impact of ageing on the ammonia adsorption performance of the MOFs. NIOSH specifications for respiratory protection devices also detail a drop test and a vibration test, these tests are used to investigate the robustness of the device and the adsorption material. Here we report an attrition test completed on the formed samples to investigate this.



The three materials reported here were selected to investigate the different issues surrounding a respiratory protection product where cost, performance and stability all need to be considered.

Experimental

All materials were purchased from Sigma Aldrich or Alfa Aesar and used as received. Powder X-ray diffraction (XRD) measurements were collected using a Bruker AXS D8 Advance instrument in the parallel beam mode with an Anton Parr HTK1200N sample chamber using Cu K α radiation at room temperature with a step size of 0.0223° in two theta (2θ) and a 3–100° range. Phase identification was completed using Bruker AXS Diffrac Plus, Eva V19 (1996–2013), Bruker AXS Diffrac Eva V4.0 (2010–2014) software and the ICDD PDF Files: PDF-4+ 2013, COD (REV30738 2011.11.2) database. Crystallite size and lattice parameter measurements were completed using Bruker-AXS Topas 4.2 (1999–2009) software. Nitrogen isotherm measurements were collected on a Quantachrome Autosorb-iQ-MP at 77 K, 2-station model with each station having 1 Torr, 10 Torr and 1000 Torr transducers. MOF samples were degassed using a two-step programme ramp to 90 °C for 2 hours followed by a ramp to 150 °C for 13 hours. All the BET surface areas were calculated using the Rouquerol method.^{19,20}

Synthesis of Cu-BTC

Cu(OH) $_2$ and 1,3,5-benzenetricarboxylic acid were stirred in water and MeOH in the following molar ratio (1.5 : 1 : 83 : 175). The resulting mixture was stirred for 48 hours. The resulting bright blue solid was isolated by vacuum filtration, washed with a 1 : 1 water and methanol mixture. The solid was then stirred in MeOH for a further hour, filtered by vacuum filtration, washed with MeOH and dried in ambient conditions.

Synthesis of MIL-100(Fe)

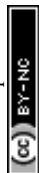
Fe(NO $_3$) $_3$ ·9H $_2$ O and 1,3,5-benzenetricarboxylic acid were stirred in water in the following molar ratio (1.1 : 1 : 38). The mixture was heated to 90 °C for 18 hours and cooled to room temperature. The red product was isolated using centrifugation (4000 rpm, 20 min) and washed three times in a 1 : 1 water : ethanol mixture before being dried in ambient conditions.

Synthesis of CPO-27(Ni)

Ni(OH) $_2$ and 2,5-dihydroxyterephthalic acid were stirred in water with the following molar ratio (1 : 2 : 98). The resulting mixture was stirred and heated to 90 °C for 18 hours. The resulting dark yellow solid was isolated by vacuum filtration, washed with warm water, and dried at 40 °C overnight.

General procedure for dry granulation

To produce MOF_1 the MOF (2.0 g) was pressed using a 4.5 cm die, considering the force per area the pressure applied to the die was 58.6 MPa. The MOF was pressed for a total of 2 minutes before the resulting pellet was crushed and sieved to give particles with a 300–1000 μ m size range.



For the repeated pressing study particles isolated below 300 μm were repressed under the above conditions a further five times to afford MOF_2 samples.

General procedure for wet granulation

To produce MOF_3 materials, the MOF (1.0 g) and poly-vinyl alcohol (PVA, 2% by weight) were granulated with water (0.25 ml). The resulting granules were sieved to a 300–1000 μm size range. It is worth noting that it was possible to form granules with the use of little or no binder (<2%), but these tended to be less uniform than those made from a mixture containing a larger amount of binder.

General procedure for the ageing of formed materials

To produce MOF_4 samples, MOF_1 (2 g) was placed in an open container in a humidity controlled chamber at 40 °C and 80% humidity for 7 days. The resulting aged MOF was characterised and tested for ammonia adsorption performance.

General procedure for the attrition test

The MOF (0.2 g) was placed in a small vial which was rolled for 18 hours on a roller mill. The MOF was then sieved to remove all the material below 300 μm and the remaining material weighed.

General procedure for ammonia adsorption test

The formed MOF (~ 0.1 g) was placed into a plug flow reactor with an internal diameter of 8 cm, and the reactor bed was packed to a height of 4 mm. A gas stream with a flow rate of 500 ml min^{-1} of ammonia (500 ppm) in nitrogen with 20% oxygen was humidified to an RH of 40%. This stream was passed through the packed bed and analysed using FTIR. The MOF was not pre-treated prior to the experiment.

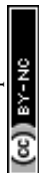
The error within the test was evaluated using a commercial mordenite material and was found to be 4 mg g^{-1} . The ammonia adsorption capacity and breakthrough times reported here are the average of two experimental runs.

Results and discussion

Each of the materials discussed within this paper is known to adsorb ammonia, however here we discuss various ways to form the three selected MOFs into shapes applicable for respiratory applications.

The MOFs have been granulated in two ways; dry granulation and wet granulation. These two techniques were investigated due to their industrial relevance. The studies completed with MIL-100(Fe), Cu-BTC and CPO-27(Ni) are described here.

Dry granulation is a large scale industrial technique which compacts material and produces non-uniformly shaped pellets. These pellets are then sieved to the application specific size. Material below this size range is recycled to increase the yield of particles in the correct size range. For many materials *i.e.* carbons this repeated compaction has little impact on the performance of the final product, however, it is thought that repeated compaction may have a more significant impact on MOF materials. To determine how dry granulation affects the structure



and the surface area of the MOFs discussed here, materials were pressed and sieved, and the resulting pellets were characterised and tested (MOF_1). The fines (particles < 300 μm) obtained during the sieving step were re-pressed and sieved to the correct size. This process was repeated a total of five times to mimic the large scale industrial process and investigate the how robust the MOF materials were to repeated compaction. Isolated pellets which were pressed a total of five times are noted as MOF_2, and these pellets were characterised and their ammonia adsorption capacity measured.

The secondary forming method investigated was wet granulation, a common industrial process used to produce spherical-like granules. Optimisation of the granulation process to increase the yield of particles in the correct size range is more challenging. Here we report samples made during a small-scale development study. A binding polymer was added to the MOF to produce robust granules. Here we report samples which were produced with the addition of 2% polymer, these are referred to as MOF_3. The granules produced were sieved to the desired particle range prior to characterisation and performance testing.

The ammonia adsorption performance of the shaped MOFs was tested using a plug-flow reactor to obtain breakthrough curves. All breakthrough experiments were completed under humid conditions (40% RH), with a challenge concentration of 500 ppm ammonia. The data obtained was used to calculate the ammonia capacity for each sample. Testing the formed MOFs under these conditions is representative of the NIOSH specifications and gives an indication of how the material would perform in a respiratory protection device.

For a respiratory protection device, there are three types of ageing test within the device specifications: a hot, a cold and a humidity ageing test. Here we report the humidity ageing of the formed MOFs (MOF_4). MOF_1 samples were aged at 25 °C in 80% humidity for 7 days before being fully characterised and tested. We also detail an attrition test which was completed to investigate the robustness of the formed materials. This is an in-house test which has been used to compare the materials to each other. Whilst unlikely to be representative of the NIOSH specification test it has been used to give a qualitative assessment of the material properties.

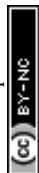
In the following sections the characterisation data and ammonia adsorption capacity of the materials produced is detailed by MOF. Table 1 shows a summary of the sample labels for reference.

CPO-27(Ni)

CPO-27(Ni) was synthesised under aqueous conditions at kilogram scale. Fig. 1 shows the powder XRD pattern for as-synthesised CPO-27(Ni). This is compared to

Table 1 Reference summary of sample names and description

Sample name	Sample description
MOF_1	Dry granulation
MOF_2	Dry granulation repeated 5 times
MOF_3	Wet granulation using 2% polymer
MOF_4	MOF_1 aged at 25 °C, 80% humidity



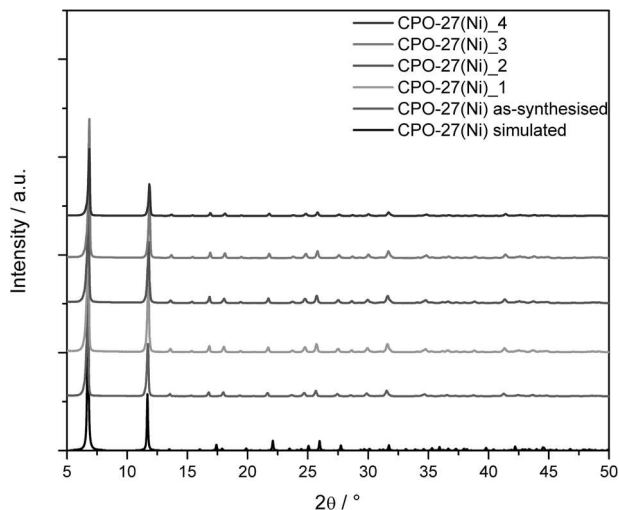


Fig. 1 Powder X-ray diffraction data of as-synthesised CPO-27(Ni) compared to the formed and aged samples; the calculated pattern of CPO-27(Ni) was simulated from the crystal structure.

the powder pattern simulated from the crystal structure and the XRD patterns of the formed samples.

Rietveld refinement of the as-synthesised material shows the sample to be phase pure CPO-27(Ni). The XRD patterns of CPO-27(Ni)_1 and CPO-27(Ni)_2 show that the structure is retained, indicating that repeated compaction during dry granulation has little impact on the structure of CPO-27(Ni). The crystal structure is also retained for the wet granulated material (CPO-27(Ni)_3) and the aged sample (CPO-27(Ni)_4).

Whilst the XRD data suggests there is little change in the structure of the MOF, the calculated BET surface area shows larger variation between the samples (Table 2). The surface area measurements show that the compaction of the as-synthesised CPO-27(Ni) causes a decrease in surface area. As the sample is repeatedly compacted the surface area continues to decrease (CPO-27(Ni)_2). This is not unexpected and has been previously reported by Peterson *et al.*²¹ Interestingly, the sample which had been wet granulated (CPO-27(Ni)_3) showed an

Table 2 Lattice parameters and crystallite size calculated from the Rietveld refinement of the powder XRD data from the CPO-27(Ni) series of materials along with the BET surface area

Sample ID	a (Å)	c (Å)	Crystallite size (nm)	BET surface area (m ² g ⁻¹)
CPO-27(Ni)_as-synthesised	25.9636(3)	6.69534(12)	82.0(15)	937
CPO-27(Ni)_1	25.9469(5)	6.68919(2)	73.1(14)	855
CPO-27(Ni)_2	25.9525(15)	6.68914(5)	76.2(17)	805
CPO-27(Ni)_3	25.9583(3)	6.6912(4)	89.4(16)	1319
CPO-27(Ni)_4	25.9504(12)	6.6897(6)	85.0(2)	257



increased surface area. Currently the reason for this is unclear and work is ongoing to investigate this further. The aged sample, CPO-27(Ni)_4, shows the lowest surface area measured, suggesting there is some decomposition of the material during humidity ageing which is not observable in the powder XRD data.

The ammonia adsorption capacity of the formed materials was evaluated. Fig. 2 shows the breakthrough curves for the CPO-27(Ni) samples. Notably the as-synthesised powder sample was not tested due to back pressure issues encountered. The breakthrough curves were used to calculate the ammonia adsorption capacity of each sample and identify the breakthrough time at 12.5 ppm ammonia. These are shown in Table 3.

The breakthrough time has been recorded at 12.5 ppm as this is the ammonia limit set within NIOSH specifications for respiratory protection devices. An activated carbon sample was also tested so that the results obtained could be compared to a control sample. The breakthrough curves show that the CPO-27(Ni) samples have a significantly increased ammonia capacity and breakthrough concentration time over the activated carbon sample.

The ammonia adsorption capacity (Table 3) of the wet granulated sample CPO-27(Ni)_3 is lower than that of the dry granulated samples (CPO-27(Ni)_1 and CPO-27(Ni)_2). Whilst the ammonia capacity of CPO-27(Ni)_2 is comparable to CPO-27(Ni)_1, the breakthrough time is reduced. This is also observed for the aged sample CPO-27(Ni)_4, although the ammonia capacity is comparable to the unaged sample CPO-27(Ni)_1 the breakthrough time is more than halved. It is of note that the shape of the breakthrough curve for CPO-27(Ni)_4 is different to CPO-27(Ni)_1, indicating that the kinetics of adsorption have changed and that much of the ammonia capacity is in the high concentration ammonia region. This is also the case for CPO-27(Ni)_2. For respiratory protection devices, having additional capacity within this region is not ideal as it is not utilised.

The data obtained from the attrition test shows that, as expected, repeated compaction produces more robust granules, exemplified by CPO-27(Ni)_2. It can

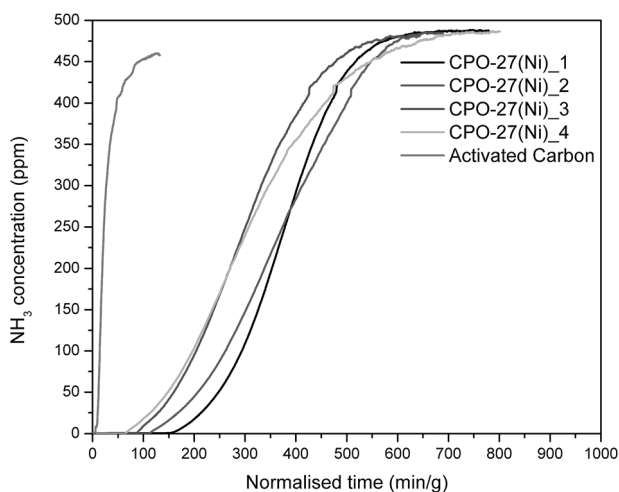


Fig. 2 Ammonia breakthrough curves for CPO-27(Ni)_1 to CPO-27(Ni)_4 and a commercial activated carbon sample.

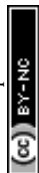


Table 3 Ammonia adsorption capacity of CPO-27(Ni) materials and the breakthrough time at 12.5 ppm ammonia

Sample	Ammonia adsorption capacity (mg g ⁻¹)	Breakthrough time (min g ⁻¹)	Attrition test percentage loss (%)
Activated carbon	8	9	0
CPO-27(Ni)_1	64	189	29
CPO-27(Ni)_2	65	141	3
CPO-27(Ni)_3	51	106	18
CPO-27(Ni)_4	61	90	64

also be seen that the use of a binder in CPO-27(Ni)_3 has a positive impact on the robustness of the granules when compared to CPO-27(Ni)_1. The aged material CPO-27(Ni)_4 is shown to have a large percentage loss suggesting that whilst ageing the material may not have a large impact on the ammonia capacity, the strength of the granules is adversely impacted.

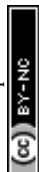
Further work to improve the robustness of the CPO-27(Ni) granules is ongoing, however the data presented here shows the increased ammonia adsorption capacity of CPO-27(Ni) when compared to activated carbon.

MIL-100(Fe)

MIL-100(Fe) was synthesised under aqueous conditions and washed with a 1 : 1 ethanol/water mixture. The main issue encountered during the scale-up synthesis is the isolation of the product. Vacuum filtration of the material is slow due to the small particle size produced. A study investigating flocculation of the material was completed, however this proved unsuccessful. Due to the slow filtration, the final product was isolated by centrifugation. Fig. 3 shows the measured powder XRD data for the as-synthesised MIL-100(Fe) compared to the simulated powder pattern. Rietveld refinement of the powder pattern shows the material to be phase pure MIL-100(Fe). The formed samples are also shown to be phase pure MIL-100(Fe) as is the aged material, MIL-100(Fe)_4.

As-synthesised MIL-100(Fe) has a BET surface area of 1212 m² g⁻¹, comparable to literature values.²² Table 4 shows the surface area values for the MIL-100(Fe) materials. Forming MIL-100(Fe) using dry granulation (MIL-100(Fe)_1 and MIL-100(Fe)_2) results in a decrease in surface area, as seen with CPO-27(Ni). MIL-100(Fe)_4 also shows a decrease in surface area when compared to MIL-100(Fe)_1, indicating that humidity ageing of the material does have an impact on the material despite powder XRD data showing that MIL-100(Fe)_4 is phase pure. Addition of the polymer for wet granulation is shown to have little impact on the surface area of MIL-100(Fe)_3, unlike the wet granulated CPO-27(Ni).

Table 5 shows the ammonia adsorption capacity and breakthrough time at 12.5 ppm ammonia for the formed MIL-100(Fe) samples. The dry granulated sample MIL-100(Fe)_2 has a lower ammonia capacity and a shorter breakthrough time than MIL-100(Fe)_1, showing that repeated compaction of the material has an impact on the performance. MIL-100(Fe)_4 shows a larger decrease in both the capacity and breakthrough time, indicating the adverse effect of ageing the MOF under humid conditions. The wet granulated sample MIL-100(Fe)_3 shows



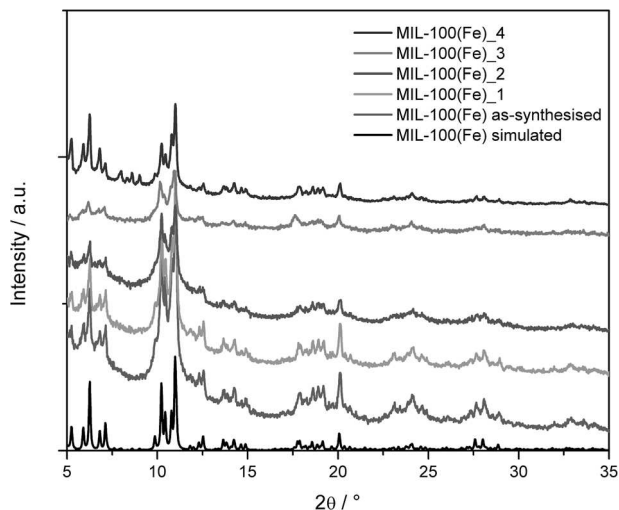


Fig. 3 Powder X-ray diffraction data of as-synthesised MIL-100(Fe) compared to the formed and aged samples; the calculated pattern of MIL-100(Fe) was simulated from the crystal structure.

Table 4 Lattice parameters and crystallite size calculated from the Rietveld refinement of the powder XRD data from the MIL-100(Fe) series of materials along with the BET surface area

Sample ID	a (Å)	Crystallite size (nm)	BET surface area (m ² g ⁻¹)
MIL-100(Fe) as-synthesised	73.1389(7)	50.29(1)	1212
MIL-100(Fe)_1	73.1616(13)	65.32(5)	928
MIL-100(Fe)_2	73.1120(12)	35.45(36)	522
MIL-100(Fe)_3	72.9992(41)	21.21(80)	1172
MIL-100(Fe)_4	73.17658(41)	81.22(1)	727

a slightly increased ammonia capacity when compared to MIL-100(Fe)_1, however, when the error within the test is considered the difference in the data is small, suggesting the addition of the polymer has a negligible impact on the MOF.

The attrition test data shows all the formed samples produced to be relatively robust. However, as with CPO-27(Ni)_4 the aged sample MIL-100(Fe)_4 shows an increased mass loss compared with the other materials. Humidity ageing was completed on the dry granulated MIL-100(Fe)_1, and work is currently underway to study the ageing effects on the wet granulated material.

Cu-BTC

Cu-BTC was synthesised in a water/methanol solvent mixture and washed with methanol. It is of note that washing the material with water alone results in a different material which was not identified. Fig. 4 shows the measured XRD patterns for the Cu-BTC samples. As-synthesised Cu-BTC was activated at 120 °C

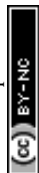
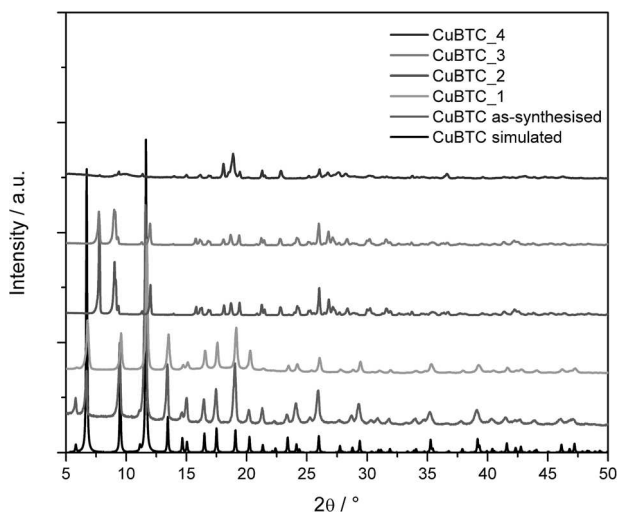


Table 5 Ammonia adsorption capacity of MIL-100(Fe) materials and the breakthrough time at 12.5 ppm ammonia

Sample	Ammonia adsorption capacity (mg g ⁻¹)	Breakthrough time (min g ⁻¹)	Attrition test percentage loss (%)
MIL-100(Fe)_1	47	135	3
MIL-100(Fe)_2	44	92	8
MIL-100(Fe)_3	50	100	2
MIL-100(Fe)_4	36	32	74

**Fig. 4** Powder X-ray diffraction data of as-synthesised Cu-BTC compared to the formed and aged samples; the calculated pattern of Cu-BTC was simulated from the crystal structure.

under vacuum and subsequently hydrated by exposure to the ambient atmosphere prior to forming.

The XRD patterns of the formed samples show that only Cu-BTC_1 retains the Cu-BTC structure, this was confirmed by the Rietveld refinement. Repeated compaction of the fines produced Cu-BTC_2, and the XRD data shows that this has caused the structure to decompose. This decomposition can also be observed in the colour of the material. Fig. 5 shows an image of the dry granulated Cu-BTC pellets; after each cycle of compaction the colour of the sample changes.

Using the powder XRD patterns of Cu-BTC_2, _3 and _4, phase identification of the samples was attempted; this showed that the materials consist of a mixed phase system, containing hydrogen triaquabenzene-1,3,5-tricarboxylate copper(II) along with a second decomposition product. To the best of our knowledge the identity of the Cu-BTC decomposition product has not yet been identified in the literature.

Table 6 shows the BET surface area of the Cu-BTC samples. Whilst the initial compaction results in a slight loss of surface area, the decomposition of the Cu-BTC structure causes a larger decrease in the BET surface area, which is observed



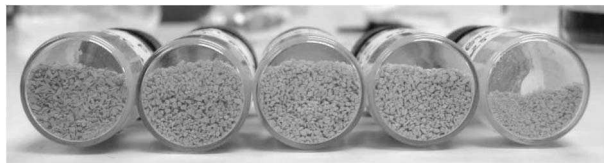


Fig. 5 Cu-BTC_1 (far left) and Cu-BTC_2 (far right).

Table 6 Phase ID, lattice parameters and crystallite size calculated from the Rietveld refinement of the powder XRD data from the Cu-BTC series of materials along with the BET surface area

Sample ID	Phase ID	a (Å)	Crystallite size (nm)	BET surface area (m ² g ⁻¹)
Cu-BTC as-synthesised	Cu-BTC	26.3876(19)	57.0(2)	1605
Cu-BTC_1	Cu-BTC	26.3629(10)	49.6(2)	924
Cu-BTC_2	Mixed phase system	N/A	N/A	144
Cu-BTC_3	Mixed phase system	N/A	N/A	147
Cu-BTC_4	Mixed phase system	N/A	N/A	132

for Cu-BTC_2. Wet granulation of Cu-BTC (Cu-BTC_3) and ageing of the material (Cu-BTC_4) results in the same decomposed structure and loss of surface area.

The change in structure also results in a decrease in the ammonia adsorption capacity and breakthrough time, shown in Table 7. The ammonia adsorption capacity of Cu-BTC_1 is, as expected, the highest of all the materials reported within this paper. Repeated compaction of Cu-BTC results in a decrease in capacity and breakthrough time, exemplified by Cu-BTC_2. Cu-BTC_4 shows a decreased ammonia adsorption capacity and a much-reduced breakthrough time when compared to Cu-BTC_1, showing the impact ageing the material in humid conditions has on the performance.

The attrition test shows that decomposition of Cu-BTC during repeated compaction does not have a massive impact on the robustness of the granules, with an 18% loss for Cu-BTC_1 and a 17% loss for Cu-BTC_2. This contrasts with the aged material Cu-BTC_4 which decomposed during the ageing test and has a much larger percentage loss. Interestingly, part of this loss was due to oversized granules >1000 µm, indicating that some granules had agglomerated.

Table 7 Ammonia adsorption capacity of Cu-BTC materials and the breakthrough time at 12.5 ppm ammonia

Sample	Ammonia adsorption capacity (mg g ⁻¹)	Breakthrough time (min g ⁻¹)	Attrition test percentage loss (%)
Cu-BTC_1	105	210	18
Cu-BTC_2	38	47	17
Cu-BTC_3	19	43	11
Cu-BTC_4	46	80	69



The change in structure and subsequent reduced ammonia adsorption performance of Cu-BTC upon granulation and ageing suggests that the material may not be robust enough for respiratory protection devices.

Conclusions

Three MOFs have been synthesised at a 1 kilogram scale and the resulting products have been formed *via* wet and dry granulation routes. The materials have been shown to produce pellets and granules using different industrially relevant processes. The formed materials were subsequently tested for ammonia adsorption using breakthrough measurements.

CPO-27(Ni) is shown to have good ammonia adsorption capacity in both dry and wet granulated forms. The data shows that wet granulated samples have a lower capacity than the dry granulated materials, indicating that in this case compaction may be the preferred method of forming for this MOF. Ageing the sample has little impact on the ammonia capacity of the material although it does decrease the breakthrough time, and from the shape of the breakthrough curve it can be seen that the kinetics of adsorption change.

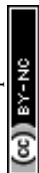
MIL-100(Fe) is shown to have the lowest fresh ammonia adsorption capacity of the three MOFs investigated here. Repeated dry granulation has a small impact on the capacity of the MOF but a larger impact on the breakthrough time when compared to MIL-100(Fe)_1. It is interesting that wet granulation with 2% polymer (MIL-100(Fe)_3) produces granules which have both a good ammonia adsorption capacity and breakthrough time. Ageing MIL-100(Fe) results in a small decrease in capacity and a large decrease in breakthrough time, this again is due to a change in the kinetics of adsorption.

It has been shown that Cu-BTC can be granulated using dry granulation, however repeated dry granulation, completed to reduce waste, results in decomposition of the MOF. Cu-BTC_1 has been shown to have the highest fresh ammonia adsorption capacity of the three MOFs reported here. However, ageing of the sample results in a significant change in the structure and a decrease in ammonia capacity. In the data presented here it has not been possible to form Cu-BTC in the industrially relevant ways investigated whilst retaining high ammonia adsorption capacities. Forming Cu-BTC in relevant conditions and investigating the resulting stability of the material requires further work.

The data presented here indicates that overall CPO-27(Ni) is the preferred MOF for use in the adsorption of ammonia within respiratory protection devices. However, each of the MOFs reported here has drawbacks: Cu-BTC has stability problems during forming, MIL-100(Fe) has a lower performance compared to both CPO-27(Ni) and Cu-BTC, and CPO-27(Ni) is costly to synthesise. These three material properties, stability, performance and cost, all need to be considered when producing a respiratory protection device.

Acknowledgements

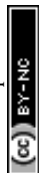
This work has been carried out within the ProDIA project that has received funding from the European Union's Horizon 2020 research and innovation programme under grant agreement No. 685727. The authors would like to thank the JMTC analytical department, specifically Huw R. Marchbank for XRD analysis and



Markus Knaebbeler-Buss for nitrogen isotherm analysis. Thanks also go to Ian Casely for synthesis of CPO-27(Ni) and Chiara Sexton for work on the wet granulation study.

References

- 1 B. GmbH, *US Pat.*, 0 166 970, 2016.
- 2 J. B. DeCoste and G. W. Peterson, *Chem. Rev.*, 2014, **114**, 5695.
- 3 G. W. Peterson, D. K. Britt, D. T. Sun, J. J. Mahle, M. Browe, T. Demasky, S. Smith, A. Jenkins and J. A. Rossin, *Ind. Eng. Chem. Res.*, 2015, **54**, 3626.
- 4 E. D. Metzger, C. K. Brozek, R. J. Comito and M. Dincă, *ACS Cent. Sci.*, 2016, **2**, 148.
- 5 J. Jiang, H. Furukawa, Y.-B. Zhang and O. M. Yaghi, *J. Am. Chem. Soc.*, 2016, **138**, 10244.
- 6 D.-L. Chen, H. Shang, W. Zhu and R. Krishna, *Chem. Eng. Sci.*, 2014, **117**, 407.
- 7 J. E. Mondloch, M. J. Katz, W. C. Isley III, P. Ghosh, P. Liao, W. Bury, G. W. Wagner, M. G. Hall, J. B. DeCoste, G. W. Peterson, R. Q. Snurr, C. J. Cramer, J. T. Hupp and O. K. Farha, *Nat. Mater.*, 2015, **14**, 512.
- 8 L. Hamon, C. Serre, T. Devic, T. Loiseau, F. Millange, G. Férey and G. De Weireld, *J. Am. Chem. Soc.*, 2009, **131**, 8775.
- 9 J. B. DeCoste, M. A. Browe, G. W. Wagner, J. A. Rossin and G. W. Peterson, *Chem. Commun.*, 2015, **51**, 12474.
- 10 A. M. Ebrahim, B. Levasseur and T. J. Bandosz, *Langmuir*, 2013, **29**, 168.
- 11 M. J. Katz, A. J. Howarth, P. Z. Moghadam, J. B. DeCoste, R. Q. Snurr, J. T. Hupp and O. K. Farha, *Dalton Trans.*, 2016, **45**, 4150.
- 12 T. G. Glover, G. W. Peterson, B. J. Schindler, D. Britt and O. Yaghi, *Chem. Eng. Sci.*, 2011, **66**, 163.
- 13 H. Jasuja, G. W. Peterson, J. B. DeCoste, M. A. Browe and K. S. Walton, *Chem. Eng. Sci.*, 2015, **124**, 118.
- 14 P.-J. Kim, Y.-W. You, H. Park, J.-S. Chang, Y.-S. Bae, C.-H. Lee and J.-K. Suh, *Chem. Eng. J.*, 2015, **262**, 683.
- 15 D. Crawford, J. Casaban, R. Haydon, N. Giri, T. McNally and S. L. James, *Chem. Sci.*, 2015, **6**, 1645.
- 16 V. Finsy, L. Ma, L. Alaerts, D. E. De Vos, G. V. Baron and J. F. M. Denayer, *Microporous Mesoporous Mater.*, 2009, **120**, 221.
- 17 C. A. Grande, V. I. Ágüeda, A. Spjelkavik and R. Blom, *Chem. Eng. Sci.*, 2015, **124**, 154.
- 18 P. L. C. Johnson Matthey, WO Pat., 160683, 2013.
- 19 J. Rouquerol, P. Llewellyn and F. Rouquerol, *Stud. Surf. Sci. Catal.*, 2007, **160**, 49.
- 20 K. S. Walton and R. Q. Snurr, *J. Am. Chem. Soc.*, 2007, **129**, 8552.
- 21 G. W. Peterson, J. B. DeCoste, F. Fatollahi-Fard and D. K. Britt, *Ind. Eng. Chem. Res.*, 2014, **53**, 701.
- 22 Y.-K. Seo, J. W. Yoon, J. S. Lee, U.-H. Lee, Y. K. Hwang, C.-H. Jun, P. Horcajada, C. Serre and J.-S. Chang, *Microporous Mesoporous Mater.*, 2012, **157**, 137.



Synthesis, Characterization, and Ammonia Adsorption Properties of Mesoporous Metal–Organic Framework (MIL(Fe))–Graphite Oxide Composites: Exploring the Limits of Materials Fabrication

Camille Petit and Teresa J. Bandoz*

Composites of MIL-100(Fe) and graphite oxide (GO) were prepared with various ratios of the two components and tested for ammonia removal in dynamic conditions. The initial and exhausted samples were characterized by X-ray diffraction, nitrogen adsorption, thermal analysis, Fourier Transform infrared spectroscopy, Raman spectroscopy, and scanning electron microscopy. The results indicate that the formation of well-defined MIL-100(Fe)/GO composites is not favored. This is linked to the specific geometry of MIL-100(Fe). The attachment of the GO carbon layers to the spherical cages of MIL-100(Fe) (via coordination between the oxygen groups of GO and the metallic sites of the metal–organic framework) prevents the proper formation of the MIL-100(Fe) structure. Therefore, the composite with the highest GO content has a lower porosity and smaller ammonia adsorption capacity than those calculated for the physical mixture of MIL-100(Fe) and GO. The main mechanism of ammonia retention is via Brönsted interactions between ammonia and the water molecules present in MIL-100(Fe). Nevertheless, the presence of excess water in the system lowers the acidity of the MIL material, and consequently causes a decrease in the ammonia adsorption. The Lewis interactions between ammonia and the metal centers in MIL also take place during the adsorption process.

a microporous structure, nevertheless a class of MOFs with larger pores, called MIL (Material of Institut Lavoisier), was recently synthesized by Férey and coworkers.^[7,8] An example of such materials is MIL-100(Fe).^[9] In this compound, metallic units, made of iron(III), are connected via benzenetricarboxylate molecules which serve as organic linkers.^[9] The nature of the iron offers several advantages compared to other metals owing to its low cost, redox properties, non-toxicity, and environmentally-friendly character. MIL-100(Fe) exhibits a zeolite-like morphology^[8–10] and three types of pores/cages with internal diameters of 8.7, 25, and 29 Å exist in its structure.^[2,8–10] The two latter pores are accessible via pentagonal windows in the microporous range (about 4.7–5.5 Å and 8.6 Å, respectively).^[8–10] MIL-100(Fe), and its isorecticular counterpart MIL-100(Cr), have been tested in the adsorption of CO₂, CH₄, hydrogen storage, catalysis, and drug delivery.^[9–11]

1. Introduction

Metal–organic frameworks (MOFs) represent a class of materials prepared by self-assembly of metallic ions and organic ligands (usually carboxylate, sulfonate, or phosphonate), which results in the formation of well-defined networks with high porosity.^[1–4] Owing to the diversity of chemistry (several metals can be used) and the diversity of the network geometry that can be designed (several organic ligands can be used), MOFs materials find applications in various fields such as gas adsorption, gas separation, catalysis.^[5,6] Most MOFs exhibit

To ensure the potential use of the MOF materials in industrial/large-scale applications, several concerns must be addressed. Progresses are required to improve their stability in the presence of humidity or upon a solvent removal (one of the steps of their synthesis), to process the materials into “user-friendly” configurations, and to enhance their dispersive forces and thus to increase the adsorption of small molecule gases (e.g., ammonia or hydrogen). Recent studies have tried to address these shortcomings. The common solution proposed is the formation of composites including MOF and another substrate. The substrate varies depending on the MOF selected and the application targeted.^[12–26] Most commonly used materials are polymers,^[12,13] alumina,^[14–18] oxides,^[18] carbon nanotubes,^[19–21] functionalized graphite,^[14,22] or graphite oxide (GO).^[23–26] The latter substrate was used to enhance the adsorption of small molecule gases at ambient conditions.^[23,25,26] It was found that the oxygen functionalities of GO (hydroxyl, carboxyl, epoxy, ketone) are able to coordinate to the metallic centers of the MOFs and thus allow the growth of the crystals onto the graphene layers.^[22–24] New micropores were created at the interface of the MOF units and

C. Petit, Prof. T. J. Bandoz
The City College of New York and the Graduate School of the City
University of New York
160 Convent Avenue, New York, NY 10031, USA
E-mail: tbandoz@ccny.cuny.edu

DOI: 10.1002/adfm.201002517

the graphene layers.^[23,24] This new porosity was found to be responsible for the enhanced ammonia adsorption capacity of the composites compared to the parent materials.^[25,26] In these studies, the MOF selected was either MOF-5 or HKUST-1. These two compounds differ in the nature of their metals and organic ligands. Nevertheless, owing to the cubic shape of the unit cell of both materials, the coordination sites to the metal are comprised within parallel planes (if we consider parallel faces of the cubic cell) or perpendicular planes (if we consider perpendicular faces of the cubic cell).^[27,28] This specific feature favored the attachment of the graphene layers to the MOF units and the subsequent growth of the crystal. In the case of MIL-100(Fe), the geometry of the MOF unit differs greatly since the pores are within the cages (spheres) rather than in cubes as for MOF-5 and HKUST-1.^[9] As a result, the coordination sites to the metals are located in various planes that are not necessarily parallel or perpendicular to each other. Consequently, a very disordered structure can be anticipated from the formation of MIL-100(Fe) and GO composites.

The objective of this study is to investigate the applicability of the MOF materials with a complex structure for the formation of composites with distorted graphene layers and to evaluate the possibility of the application of these new materials in the separation science. Therefore, the composites of MIL-100(Fe) and GO were prepared with varying ratios of the two components. The samples were then characterized by various techniques and tested for ammonia adsorption in dynamic conditions. The results of this study should shed some light on the potential limits in the preparation of MOF-based composites as well as on ammonia adsorption process in MIL materials.

2. Results and Discussion

Figure 1 presents the X-ray diffraction patterns of the parent materials and the composites. GO exhibits a single peak at about 9.3° , indicative of an interlayer distance of about 9.5 \AA , as calculated using Bragg's law. It has to be mentioned that a peak

below 7° on the GO XRD pattern has its origin in the sample holder. Due to the mesoporous character of MIL-100(Fe), most peaks for the MIL sample are observed in a small angle region and are characteristic of the structure of that particular MOF.^[9,29] For MIL-GO1 material, most peaks from MIL are preserved except those of low intensity ($2\theta \sim 6, 7$ and 11°), suggesting that the MOF structure is mainly preserved and the graphene layers from GO only induced slight distortion. No sign of GO is observed on this material. This can be due to the low content of GO in this sample as well as the fact that GO readily exfoliates in water upon sonication during the synthesis procedure.^[30] The first hypothesis seems the most plausible since the XRD pattern of a physical mixture of MIL-100(Fe) and GO (GO content of about 10 wt%) was analyzed and did not exhibit any peak from GO (result not shown here). In the case of MIL-GO2 sample, on the contrary, most peaks from the MIL component are absent and only small intensity peaks are observed at about $3.5, 4$ and 4.2° . Also in this sample, the graphene component cannot be distinguished. All of these indicate that in the MIL-GO2 sample, GO prevented the proper crystallization of the MOF.

The difference in the structure between the MIL-GO1 and MIL-GO2 samples is also seen based on the analysis of nitrogen adsorption isotherms. The isotherms for the MIL sample and the derived composites are plotted in Figure 2. The GO sample is not shown since it exhibits no porosity.^[31] All isotherms are of type-I and indicative of the microporous character of the samples. The different slopes observed on the isotherms are related to the two types of microporous windows of the mesoporous cages of MIL-100(Fe).^[9] This feature was already observed by Horcajada and coworkers for that specific MOF^[9] and is also evidenced in other MIL materials.^[32] Table 1 reports the parameters of the porous structure for all samples derived from nitrogen isotherms. The porosity of the MIL and MIL-GO1 samples is in the same range with a surface area of about $1430 \text{ m}^2 \text{ g}^{-1}$ and a total volume of pores of $0.750 \text{ cm}^3 \text{ g}^{-1}$. These values are slightly below the ones reported by Horcajada and coworkers for the same synthesis procedure.^[9] The MIL-GO1 material exhibits a slightly higher surface area (7% more) and volume of pores than that calculated for the physical mixture of MIL and GO (see Table 1). The physical mixture corresponds to the material obtained when no chemical interactions between the MOF units and the graphene layers are involved. This enhanced porosity (surface area and volume of pores) compared to that for the physical mixture was also observed in the case of the MOF/GO composites based on HKUST-1.^[13] In the latter study, the new porosity was linked to new pores created at the interface between the MOF units and the graphene layers owing to the coordination of the oxygen groups of GO with the metallic centers of the MOF.^[13] In the case of MIL-GO1, the beneficial interactions between the MOF units and GO layers seem to be present as well. This synergy might counterbalance the slightly negative effect of the GO layers on the MOF crystallization (and thus porosity) observed on the X-ray diffraction pattern for this sample (Figure 1). On the contrary, the MIL-GO2 surface area and total volume of pores are about 20% smaller than those of MIL and 10% smaller than those calculated for the physical mixture. These findings support the XRD results and indicate that, in MIL-GO1, the graphene layers did

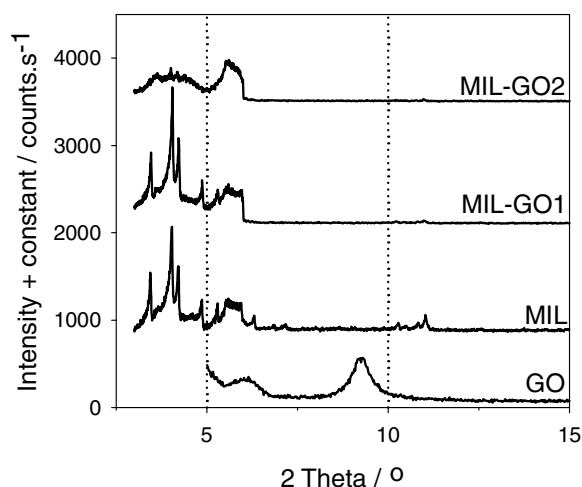


Figure 1. X-ray diffraction patterns for all the samples studied before exposure to ammonia.

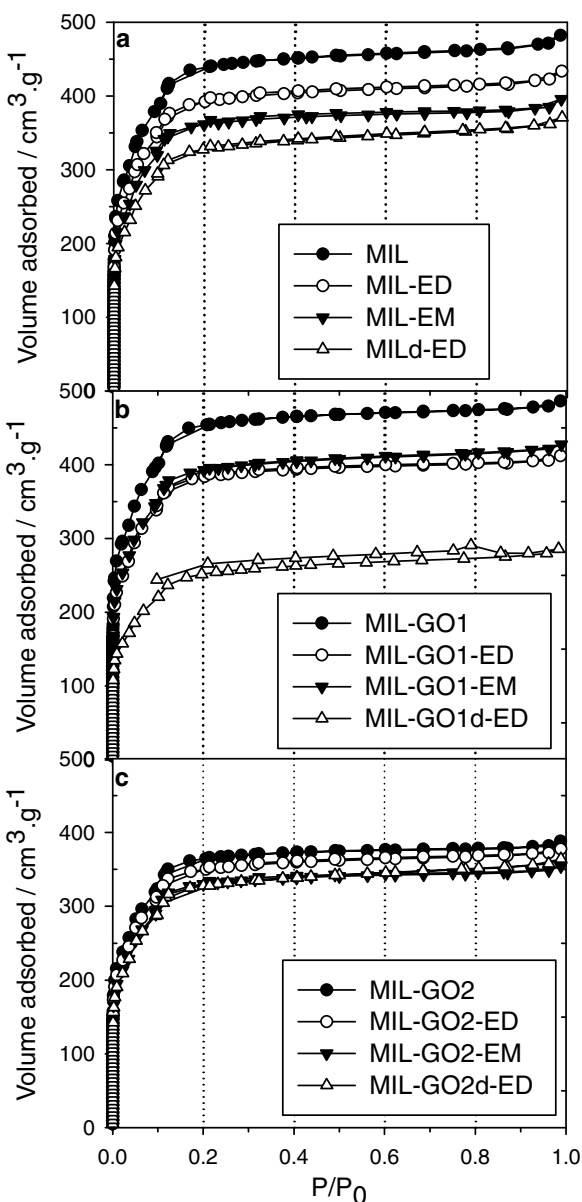


Figure 2. Nitrogen isotherms for a) the MIL sample and b,c) the composites before and after exposure to ammonia.

not significantly disturb the crystallization/porosity of the MIL component but, at a higher GO content (see MIL-GO2), they start to have a detrimental effect on the crystallization of the MOF phase (and thus porosity).

The results of thermal analysis for all materials studied are shown in **Figure 3**. The GO sample exhibits the expected pattern for this type of material.^[31] The first peak (~100 °C) is related to the removal of physically adsorbed water^[33] while at higher temperatures, the decomposition of epoxy groups (~200 °C) and carboxyl groups (250–400 °C) takes place.^[34,35] The MIL sample and the derived composites have similar thermal stabilities. At first, the molecules of free water contained inside the pores are released at about 100 °C.^[9,29] Then the decomposition of the MIL occurs in several steps starting at about

270 °C.^[9,29] The various peaks observed above 270 °C might be related to the decomposition of the organic ligand followed by the progressive reduction of the iron species from Fe₃O₄ to Fe₂O₃ and then FeO.^[36] The temperature of decomposition as well as the extent of each weight loss agree with the data reported in the literature.^[9,11] The fact that MIL-GO2 exhibits a similar thermal desorption pattern to those for the two other MIL-containing samples indicates that the graphene layers did not prevent the formation of the MIL units but only affected their crystallization (as suggested by XRD and nitrogen adsorption analyses). As observed for other MOF/GO composites, the intense peak from the decomposition of the epoxy groups in GO does not appear on the curves of the composites.^[23,24] This can be linked to the involvement of these functionalities in linkages with the metallic sites in MOF.^[23,24] Another reason, which we cannot exclude may be in the low graphite content in these materials. Nevertheless, based on the chemistry of the MIL materials (metallic sites coordinated to carboxylate-based ligands), it seems reasonable to assume that binding between GO functional groups and the iron centers in MIL occurs. This scenario is supported by the ratios of iron sites to GO epoxy groups and of iron sites to GO oxygen groups for both composites. Considering the elemental composition of MIL-100(Fe) proposed by Horcajada and coworkers,^[9] and the total amount of oxygen groups (and epoxy groups) in GO prepared by the Hummers method reported by Petit and coworkers,^[37] as well as the composition of the two composites, the ratios calculated are 5.5 (epoxy) and 3.5 (total) for MIL-GO1, and 2.6 (epoxy) and 1.7 (total) for MIL-GO2. Even though these numbers represent only an approximation of the actual values, they still indicate that the iron centers are in excess compared to the oxygen groups from GO. Thus, there were probably enough accessible metallic centers in the MIL component to react with the GO functionalities. It is interesting to notice that even though chemical interactions between the GO layers and the MOF units seem to occur in both composites, they are only beneficial in the case of MIL-GO1 sample. For this sample, these interactions are likely responsible for the new pores created at the interface between the graphene layers and the MOF blocks detected from nitrogen sorption measurements. On the contrary, for the MIL-GO2 sample, they seem to prevent the proper crystallization of the MIL.

FT-IR spectra for the MIL-containing samples are plotted in **Figure 4**. Most bands on the MIL and composites spectra originate from the carboxylate groups vibrations and appear at 710, 760, 955, 1130, 1380, 1450, 1580, and 1630 cm⁻¹. All these features are in agreement with the ones reported in the literature.^[11,29,38] In the 1300–1700 cm⁻¹ region, bands are attributed to the asymmetric and symmetric vibrations of the carboxylate groups, while the wavenumber range below 1300 cm⁻¹ is related to the out-of-plane vibrations of the same functionality.^[39,40] A shoulder at 1715 cm⁻¹ for the MIL and composite materials is noticed indicating that a small portion of the carboxylate groups are protonated.^[38] Around 3000–3700 cm⁻¹, vibrations from water molecules are observed.^[33] From these features, one can see that the FT-IR spectra for MIL material and the two composites are identical. This supports the findings from thermal analyses and indicates the existence of MOF units in the composites.

Table 1. Parameters of the porous structure derived from the nitrogen isotherms at $-196\text{ }^{\circ}\text{C}$ for the samples studied before and after exposure to ammonia as well as the parameters calculated for the physical mixture (H).

Sample	S_{BET} [$\text{m}^2\text{ g}^{-1}$]	V_t [$\text{cm}^3\text{ g}^{-1}$]	V_{meso} [$\text{cm}^3\text{ g}^{-1}$]	V_{mic} [$\text{cm}^3\text{ g}^{-1}$]	V_{mic}/V_t	$S_{\text{BET}}^{\text{H}}$ [$\text{m}^2\text{ g}^{-1}$]	V_t^{H} [$\text{cm}^3\text{ g}^{-1}$]	$V_{\text{mic}}^{\text{H}}$ [$\text{cm}^3\text{ g}^{-1}$]
MIL	1413	0.746	0.087	0.587	0.79	—	—	—
MIL-ED	1266	0.671	0.140	0.531	0.79	—	—	—
MIL-EM	1166	0.612	0.115	0.497	0.81	—	—	—
MILd-ED	1064	0.573	0.133	0.440	0.77	—	—	—
MIL-GO1	1464	0.752	0.160	0.592	0.79	1366	0.721	0.568
MIL-GO1-ED	1235	0.637	0.112	0.525	0.82	—	—	—
MIL-GO1-EM	1270	0.661	0.130	0.531	0.80	—	—	—
MIL-GO1d-ED	828	0.442	0.122	0.330	0.75	—	—	—
MIL-GO2	1172	0.600	0.099	0.501	0.84	1290	0.681	0.536
MIL-GO2-ED	1127	0.584	0.107	0.477	0.82	—	—	—
MIL-GO2-EM	1066	0.548	0.095	0.453	0.83	—	—	—
MIL-GO2d-ED	1066	0.548	0.095	0.453	0.83	—	—	—

Raman spectra of the materials studied are presented in **Figure 5**. GO spectrum exhibits two broad peaks at 1615 and 1370 cm^{-1} . The latter features are attributed to the G and D bands, respectively.^[41,42] The former band is related to the in-phase vibration of the graphite lattice whereas the D band originates from the presence of disordered regions/defects in the graphite lattice caused by the oxidation treatment.^[41,42] These patterns are characteristic of graphite oxide.^[42] Several peaks are detected on the spectrum of the MIL sample at: 1385, 1475, 1560, and 1620 cm^{-1} . Interpretation of MOFs' Raman spectra in the literature is not always consistent which makes the assignment of the bands observed here difficult. Nevertheless, it seems reasonable to assign the bands to vibrations in the organic component of the MOF and more precisely to the asymmetric and symmetric stretching vibration of the carboxylate as well as the vibrations of C=C bond from the benzene ring.^[43,44] The spectra of MIL-GO1 and MIL-GO2 differ from those of GO and MIL. Although the main bands seen on MIL spectrum remain, several changes are observed. First, the band at 1385 cm^{-1} broadens and the intensity of the band at 1475 cm^{-1} decreases and a shoulder appears at 1500 cm^{-1} . Moreover, a shoulder is observed on the band at 1620 cm^{-1} . The broadening of the band at 1385 cm^{-1} is likely related to an overlap with the D band from GO. The presence of GO (G band) might also partially overlaps with the band at 1620 cm^{-1} causing the apparent splitting of that band. The latter two features confirm the presence of GO in the composites. The change in the band at about 1475 cm^{-1} can be related to a change in the organic ligand coordination since carboxylate vibrations are usually observed in this region.^[43] This would confirm that the graphene component introduced some distortion in the MOF structure, as already suggested by the above described analyses. In order to further confirm the distortion of the MOF structure, the hypothetical spectra (of the two composites) was created from the spectra of the parent components taking into account the percentage of GO and MIL in the composites (not shown here). Even though the estimation is very rough and it assumes the same contribution of the signal intensities as for the parent components, these spectra revealed less peaks than

those present on the measured spectra for the composites. This supports our observation that GO in the composite affected the structure of the MIL component.

SEM images are presented in **Figure 6**. In GO, a very dense and disordered arrangement of graphene layers is observed. In the case of the MIL sample, a well-defined octahedral crystal is seen with some remains of an amorphous phase. For the sample with the low GO content (MIL-GO1), the surface of the particle is less smooth than that for the MIL sample which may be due to a higher degree of defects and/or the presence of graphene layers "covering" the MIL particles. These features are much more pronounced for MIL-GO2 for which smaller particles with a more irregular texture are observed, suggesting a higher amount of an amorphous phase. These results are in agreement with the X-ray diffraction data.

Differences in our materials are also visible by analyzing their performance for ammonia removal. The breakthrough and desorption curves for the parent materials and the composites are presented in **Figure 7**. The adsorption capacities derived from the breakthrough curves are listed in Table 2 along with the capacities calculated for the physical mixture for the composites. As seen in Table 2, the ammonia breakthrough capacity in dry conditions (without prior drying of the sample) decreases with an increase in the GO content. For the other conditions, we observe the following trend: MIL-GO1 > MIL > MIL-GO2. It is interesting to notice that the measured capacities of MIL-GO1 are higher than that of the physical mixture (except those measured in the dry conditions without a prior sample drying). This suggests that in MIL-GO1, a synergetic effect between the MOF component and the graphene layers exists, leading to the increased ammonia adsorption. This effect is consistent with the formation of new pores as indicated from nitrogen adsorption measurements. On the other hand, for the MIL-GO2 sample, since there is no beneficial interaction between the MIL units and the graphene layers, no enhancement is observed for both the nitrogen and ammonia adsorptions.

Not only do the ammonia breakthrough tests provide information on the availability of the adsorption centers, but they also highlight some other aspects of ammonia retention in

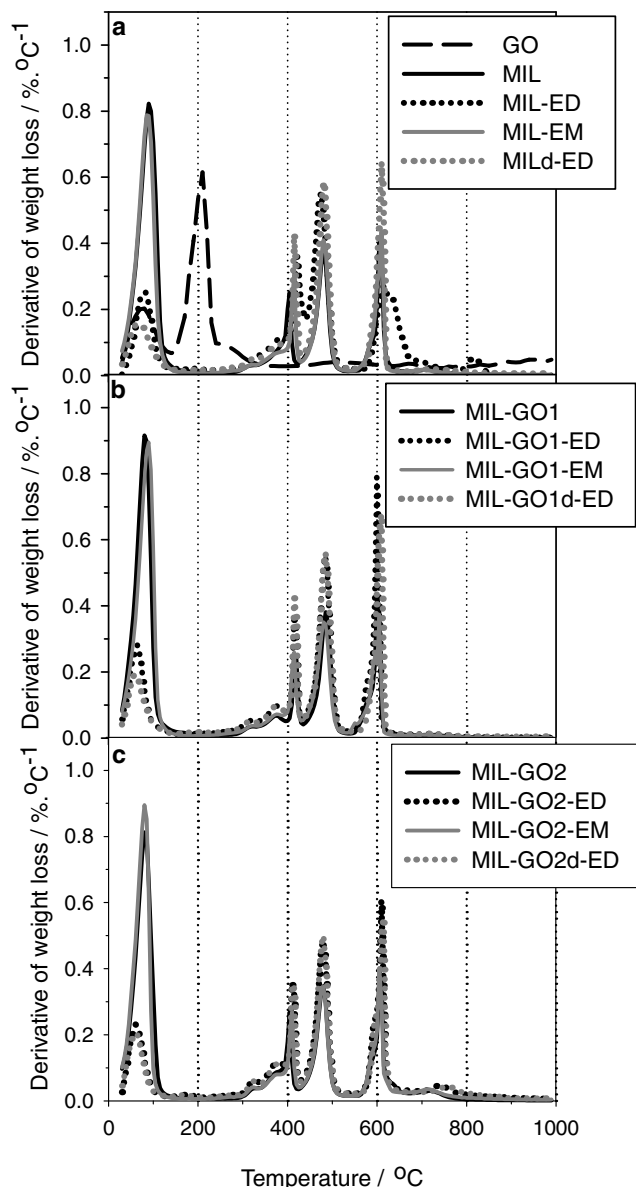


Figure 3. DTG curves for the a) GO and MIL samples and b,c) the composites before and after exposure to ammonia.

these materials. As seen in Table 2, the adsorption capacities range from about 30 to 90 mg g⁻¹ depending on the materials and the conditions of the tests. These values are much higher than the ones reported on virgin activated carbons tested in similar conditions.^[45] Moreover, one can see that the adsorption capacities follow the trend: ED after drying > ED > EM. This order indicates that the presence of water in the system is detrimental for the ammonia retention. This finding seems to be in contradiction with other studies showing an enhancement in ammonia adsorption in the presence of water.^[45] This enhancement was attributed to the dissolution of ammonia in water and can happen only when a film of water covers pore walls.^[46] Since this effect is mainly observed for microporous materials^[26,47,48] and MIL contains mesoporous cages, this phenomenon, and thus the effect of water on ammonia dissolution, cannot be

considered as predominant. To understand the behavior of MIL and the composites as ammonia adsorbents, one has to look at the coordination of the metallic centers. Vimont and coworkers in their study of MIL-100(Cr) showed that two main types of water exist in this material.^[29] The first one corresponds to water molecules directly coordinated to the metallic sites, and the second to water molecules hydrogen-bonded to the first type of water molecules.^[29] It was suggested that the first type of water is released at about 150 °C leaving unsaturated Cr³⁺ sites, and the second at about 100 °C.^[29] Vimont and coworkers also found that the Brönsted acidity of the latter type of water is weaker than that of the former.^[29] Although all these findings are for the chromium type MIL-100, given the identical structure of MIL-100(Fe), one can expect the similar arrangements of water in the case of MIL-100(Fe). For our samples run in the dry conditions without prior drying, both types of water molecules must be present. Since the second type is the first to be in contact with ammonia, its lower Brönsted acidity likely causes less ammonia to be retained on the surface than in the case of the dried samples. The schematic view of the Brönsted interactions between ammonia and water is presented in Figure 8. It has to be mentioned here that for the dried materials, a part (small) of metallic centers might be free of water and thus some ammonia molecules could be coordinated to the iron sites. This would correspond to Lewis acid/base interactions (electronic vacancy on the iron sites and lone pair of electrons on ammonia) which are shown in Figure 8. We now have to explain why the experiments run in the moist conditions induce the smaller adsorption capacities than those run in the dry conditions. The reason for this may be found in a competition between ammonia and water molecules for adsorption on the preadsorbed water molecules (the first type). This competition is supported by the similarity in the energy associated with hydrogen bonding between two molecules of water and between a molecule of water and a molecule of ammonia.^[49] As seen from the data collected in Figure 7, the desorption curves for the samples dried before the tests are steeper than those for the not-dried materials. This behavior indicates that ammonia is more strongly retained on the dried materials. This supports the above presented hypothesis proposing the adsorption mechanism on these materials. As suggested above based on FTIR spectra, it should be noted that some organic ligands of the MIL component (in the MIL sample and composites) are protonated. Thus, reaction between NH₃ and these acidic sites cannot be excluded.

If the retention of ammonia on our materials occurs only via Brönsted interactions or coordination to the metallic sites as described above, then no visible decomposition/distortion of the MOF structure should be observed in the exhausted adsorbents compared to the initial ones. Confirmation of this is presented below based on thermal analysis and FT-IR spectra of the samples before and after the exposure to ammonia.

As seen from Figure 3, no significant changes are observed on the DTG curves after ammonia. As expected, the intensity of the peak related to the removal of water (at about 100 °C) decreases for the samples run in dry conditions. This indicates that the chemistry of the materials is mostly preserved after the exposure to ammonia and that no reaction between NH₃ and the framework occurred during adsorption, at least to a

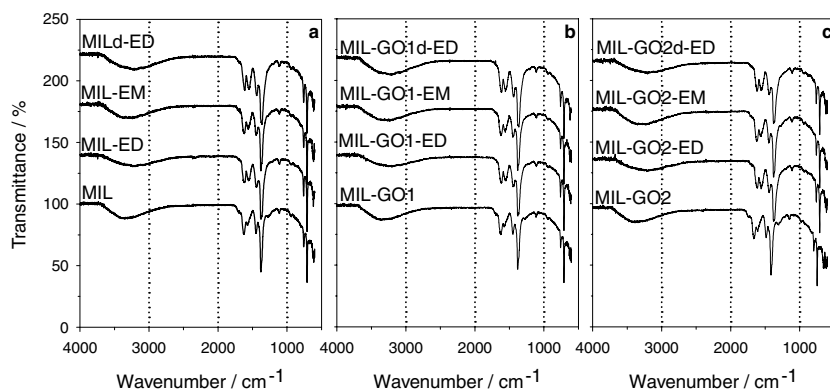


Figure 4. FT-IR spectra for a) the MIL sample and b,c) the composites before and after exposure to ammonia.

measurable extent. The only noticeable difference is the broadening of the peak at 600 °C with a shift towards higher temperatures and an increase in the intensity of the one around 800 °C for MIL-ED. Further tests would be needed to fully understand this pattern. Nevertheless, we can hypothesize that a change in the environment of the iron species as a result of ammonia adsorption caused the modification of the iron reduction process. This hypothesis is supported by the fact that the new pattern is observed in the dry conditions when ammonia molecules are closer to the iron centers.

FT-IR spectra of the MIL and composite samples before and after the exposure to ammonia support the thermal analyses' results (Figure 4). The features for the exhausted samples are similar to those of the initial samples suggesting that ammonia did not react with the MOFs units and thus did not cause their

collapse/decomposition. However, we can see a change in the 1580 cm⁻¹ band with an increase in its intensity as less water is present in the system. Indeed, this effect is more pronounced for the dried samples run in the dry conditions and less defined for the samples run in the moist conditions. This change in the FT-IR spectra indicates a distortion/change in the coordination between the carboxylate groups and the metallic centers.^[50] This modification is less pronounced in the absence of water probably because water molecules act as a "shielding agent" for the metallic sites.^[51] Indeed, as described above, for the dried samples run in the dry conditions, ammonia molecules are closer to the iron centers. Consequently,

they are more likely to induce distortion in the iron/carboxylate coordinations.

The porosity (the surface areas and volume of pores) of the exhausted samples (Figure 2, Table 1) also did not change significantly after the exposure to ammonia which is in agreement with the apparently limited reaction of ammonia with the MOF component and the limited distortion of the MOF framework (Table 1). The decrease in the surface area and volume of pores, probably caused by the strong retention of ammonia on the surface of the materials, ranges from about 4 to 25% depending on the samples and the experimental conditions of adsorption. For the MIL-GO1d sample run in the dry conditions, on which the largest adsorption capacity was measured, the decrease in the surface area and volume of pores reaches about 50%. One can notice that the decrease in porosity is less pronounced for the nondried samples than for the dried ones. This is likely related to the higher amount of ammonia retained on the latter samples which must block the pores. The results support our hypothesis that ammonia adsorption in MIL and the composites occurs mainly via interactions with the Brönsted sites of the MIL and physisorption. This is different from the findings on other MOFs and MOF/GO composites for which ammonia reacts with the metallic centers of the MOF and/or the organic ligands, causing the progressive collapse of the structure.^[25,26] Although the mechanisms of adsorption on MIL and the derived composites probably limit the amount of ammonia that can be retained compared to other MOFs, it also enables the potential regeneration and reuse of the materials.

Considering the above results, it is evident that unlike the previous findings for the other types of MOF (MOF-5, HKUST-1), building the MIL/GO composites has apparent limitations since a distortion of the MOF structure is observed at low GO content (9 wt%). More precisely, the detrimental effects observed in the MIL-GO2 sample include the decreased porosity (surface area and volume of pores) and ammonia adsorption capacity compared to those for the physical mixture. These effects can be better visualized by comparing the possible arrangement/interactions between the graphene layers and the pores/units of MIL, MOF-5, and HKUST-1. The schematic views of these interactions are proposed in **Figure 9** for the three MOFs. As presented, in the case of MOF-5 and HKUST-1, the carbon layers coordinated to the MOF units via their oxygen groups

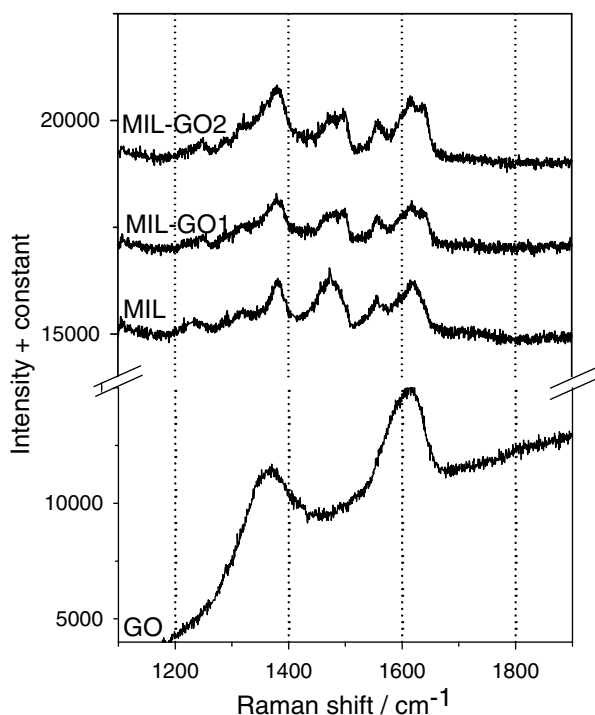


Figure 5. Raman spectra for all samples before exposure to ammonia.

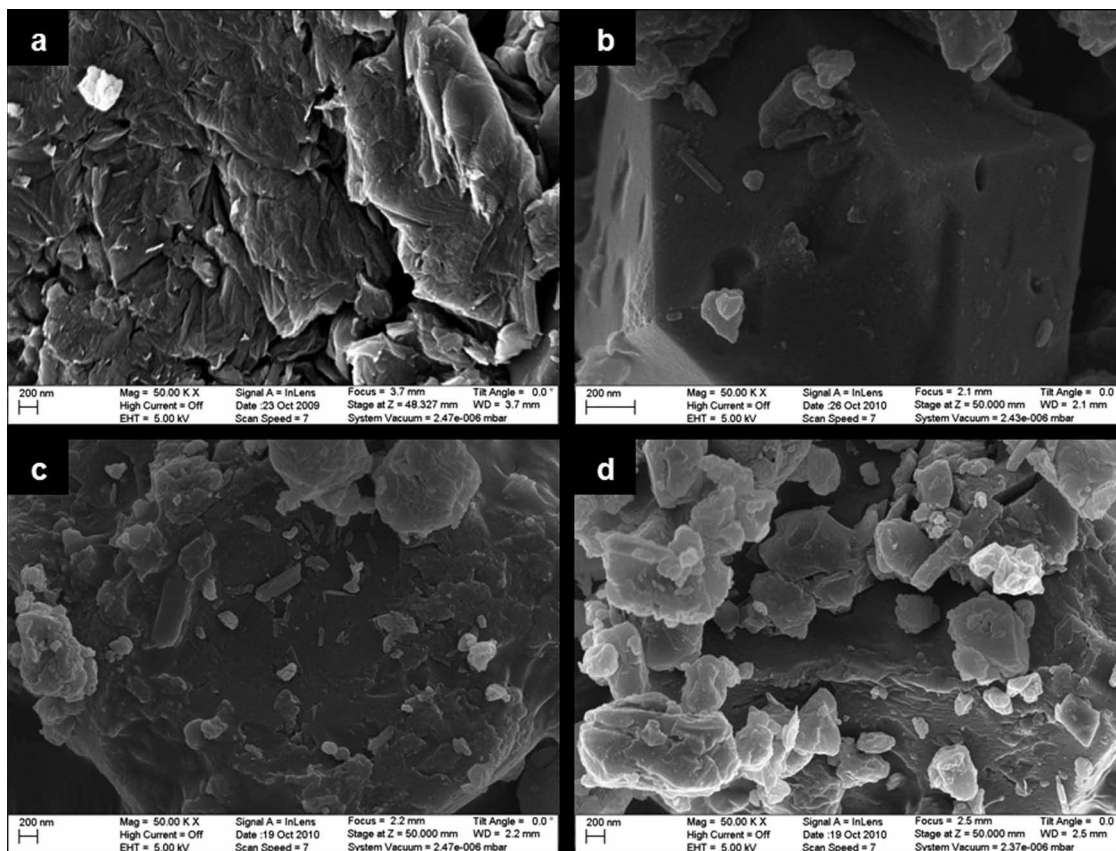


Figure 6. SEM images for: a) GO, b) MIL, c) MIL-GO1, and d) MIL-GO2.

can be either parallel or perpendicular to each other. In both cases, owing to the cubic shape of the two MOFs unit cell, new MOF units can continue to form around the first cell in a “normal” way. On the contrary, for the MIL material, owing to the spherical shape of the pores (only one type of cages shown here), the graphene layers have more than two ways of coordination to the MOF units. Due to these various possibilities of attachment, the graphene layers prevent the building of the MIL by blocking the assembly of several cages into a zeolite-like network. This is supported by the fact that when attempts were made to increase the content of GO in the composite (above 10 wt%), the MIL formation did not occur. At a very low GO content, as in the case of MIL-GO1, the probability to have two or more carbon layers linked to the MIL cages is reduced. This would explain why the detrimental effect of the presence of the GO disturbed graphene layers on the overall properties of the composites is not observed for this material.

3. Conclusions

The results of this study indicate that, unlike other types of MOF, MIL-100(Fe) is not an ideal candidate to build the MOF/GO composites. The reason for this lies in the particular shape of MIL-100(Fe) cages. Indeed, owing to the spherical pores of MIL-100(Fe), several GO carbon layers can coordinate to the MIL units (interactions of oxygen groups of GO and the metallic

sites of MIL) via various possible orientations. These specific ways of coordination prevents the proper formation/attachment of other MOF units around the first unit, thus affecting the formation of the whole framework. This effect means that the composites exhibit lower porosity (surface area and volume of pores) and ammonia adsorption capacity than the physical mixture of the MIL and GO. This detrimental effect is not seen for very small GO content since, in that case, the probability of the coordination of many GO carbon layers to one MIL unit is limited. From the point of view of ammonia adsorption, it is found that the main mechanism of retention on MIL-100(Fe) is via Brönsted interactions between ammonia and the water molecules present in the MOF. Nevertheless, the presence of “excess water” in the system lowers the apparent acidity of the MIL material, and consequently causes a decrease in the ammonia adsorption capacity. There is also an indication that the Lewis interactions between ammonia and the metal centers in MIL also play a role in the adsorption process. Since ammonia does not react with the MIL (no bond breaking), the framework structure is not significantly affected during adsorption (no distortion or collapse). This finding differs from the results reported in other studies for MOF-5 and HKUST-1 (and derived composites) for which reactions between ammonia and the framework occurred causing the decomposition of the network. This is an important factor from the point of view of adsorbent regeneration. It has to be mentioned here that the materials studied can be considered as good ammonia adsorbents taking into account

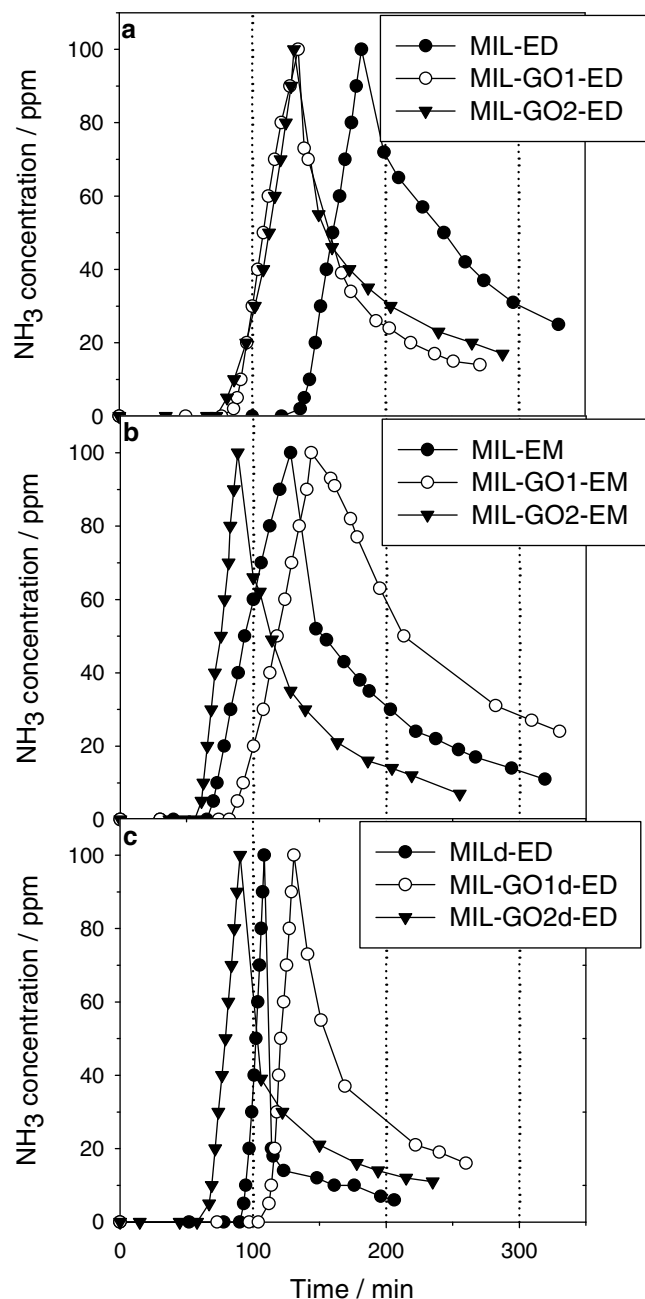


Figure 7. Ammonia breakthrough and desorption curves for the samples studied in a,b) dry and moist conditions and c) in dry conditions for the dried samples.

their capacity, strength of NH_3 adsorption, and the stability of the pore structure.

4. Experimental Section

Materials: Graphite oxide was synthesized by oxidation of graphite (Sigma-Aldrich) using the Hummers' method.^[53] The details are described elsewhere.^[37] The synthesis of MIL-100(Fe) was adapted from that of Horcajada and coworkers.^[9] Briefly, iron powder (0.83 g), 1,3,5-benzenetricarboxylic (2.06 g), hydrofluoric acid (38–40%, 0.6 mL), nitric

Table 2. Ammonia breakthrough capacities measured and calculated for the physical mixture for the samples studied.

	NH_3 Breakthrough capacity [mg g^{-1}]	Breakthrough capacity of the physical mixture [mg g^{-1}]
GO-ED	26.8	—
GO-EM	31.1	—
MIL-ED	55.7	—
MIL-EM	39.8	—
MILd-ED	73.8	—
MIL-GO1-ED	48.6	54.6
MIL-GO1-EM	44.2	39.5
MIL-GO1d-ED	90.6	72.1
MIL-GO2-ED	44.0	53.3
MIL-GO2-EM	28.4	39.1
MIL-GO2d-ED	60.4	69.9

acid (65%, 1.14 mL) and deionized water (80 mL) were mixed, stirred and placed in a 125 mL-Teflon liner. The liner was then inserted in a Parr acid digestion vessel and then progressively heated to 150 °C within 8 hours. The temperature was maintained at 150 °C for 4 days and then vessel was progressively cooled to a room temperature (in about 24 hours). The crystals formed were collected after filtration and washed with deionized water. The sample was subsequently immersed in hot water (80 °C) for 3 hours (about 1 g in 300 mL). The product was finally filtrated, washed with deionized water and dried in air. The synthesized MOF was kept in a dessicator and is referred to as MIL.

Two composites were prepared in the same way as for MIL except that various amounts of GO powder were added to the mixture of MOF precursors and the mixture was subsequently sonicated before the heat

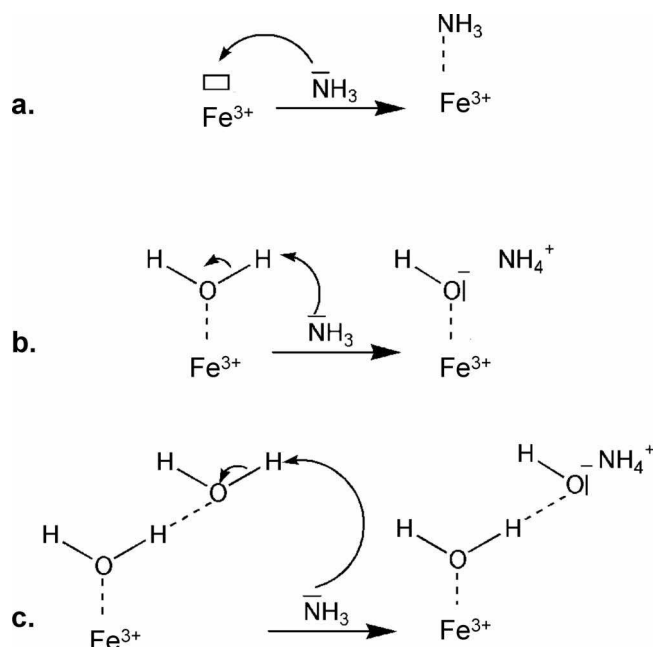


Figure 8. a) Lewis and b,c) Brønsted acid base interactions between ammonia and the MIL component.

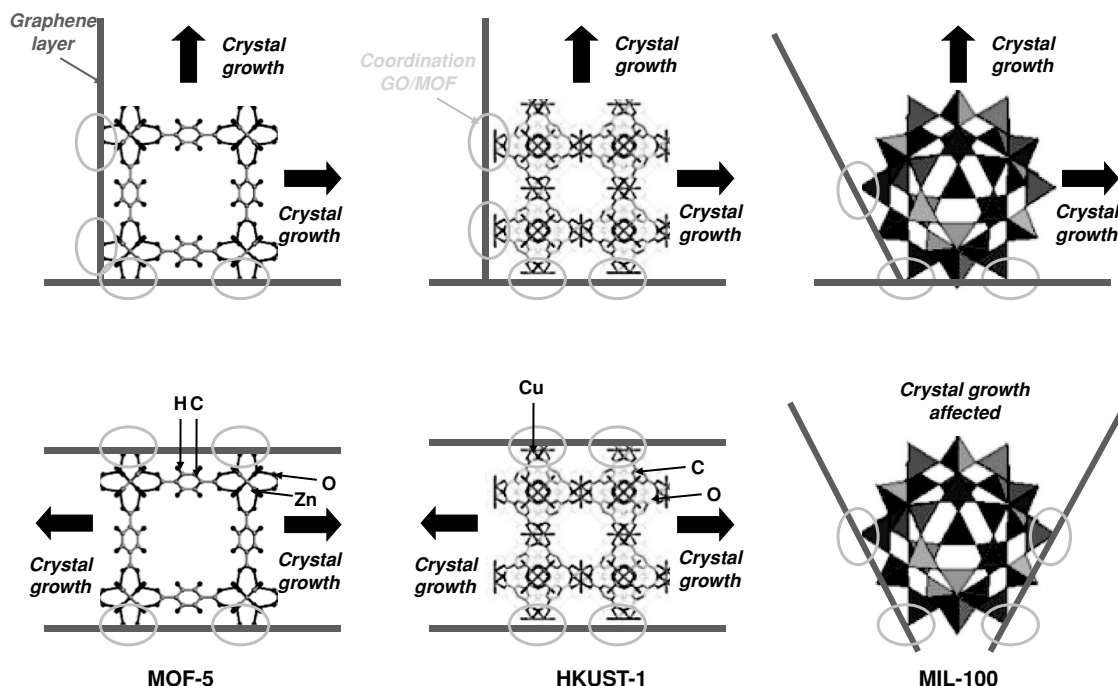


Figure 9. Schematic comparison of the coordination between GO carbon layers to the MOF units for different types of MOF network: MOF-5, HKUST-1 and MIL-100. For MOF-5 and HKUST-1: atoms indicated on the Figure. For MIL-100(Fe): the red pyramids represent supertetrahedra units made of trimers of iron octahedra linked by molecules of BTC as previously described.^[52]

treatment. The first composite contains 4 wt% of GO, and the second 9 wt%. They are referred to as MIL-GO1 and MIL-GO2, respectively. When the amount of GO added to the MOF precursors mixture was increased, the formation of MIL did not occur. A darkening of the material's color was observed as the GO content increases from 0 to 9 wt%, likely because of the black/brown tint of GO.

The MIL sample and the composites were also dried overnight in air at 120 °C to evaluate the role of water on ammonia adsorption. The resulting samples are named MILd, MIL-GO1d and MIL-GO2d, respectively.

NH₃ Breakthrough Dynamic Test: In order to determine the ammonia breakthrough capacity, dynamic breakthrough tests were performed at room temperature. In a typical test, a flow of ammonia diluted with air went through a fixed bed of adsorbent with a total inlet flow rate of 225 mL min⁻¹ and an ammonia concentration of 1000 ppm. The adsorbent's bed contained about 2 cm³ of glass beads well mixed with the amount of adsorbent required to obtain a homogeneous bed (between 250 and 500 mg). The mixture was packed into a glass column. The beads were used to avoid the pressure drop. The concentration of ammonia in the outlet gas was measured using an electrochemical sensor (Multi-Gas Monitor ITX system). The adsorption capacity of each adsorbent was calculated in mg per g of sorbent by integration of the area above the breakthrough curve. Tests in dry and wet conditions were implemented by diluting the ammonia stream with either dry or moist air stream, respectively. More precisely, two flows, one of air (dried with calcium sulfate or bubbled in deionized water) and one of ammonia (5000 ppm), were regulated by two rotameters and then combined to get the desired concentration of ammonia (1000 ppm). The experiments in dry and moist conditions were done to analyze the effects of water on the adsorption capacity. After the breakthrough tests, all samples were exposed to a flow of carrier air only (180 mL min⁻¹) to impose the desorption of ammonia and thus to evaluate the strength of its retention. The suffixes -ED and -EM are added to the name of the samples after exposure to ammonia in dry and moist conditions, respectively.

XRD: X-ray diffraction (XRD) measurements were conducted using standard powder diffraction procedures. Adsorbents (initial

and exhausted) were ground with DMF (methanol for GO) in a small agate mortar. The mixture was smear-mounted onto a glass slide and then analyzed by Cu_{Kα} radiation generated in a Philips X'Pert X-ray diffractometer. A diffraction experiment was run on standard glass slide for the background correction.

FT-IR Spectroscopy: Fourier transform infrared (FT-IR) spectroscopy was carried out using a Nicolet Magna-IR 830 spectrometer using the attenuated total reflectance method (ATR). The spectrum was generated, collected 16 times and corrected for the background noise. The experiments were done on the powdered samples (initial and exhausted), without KBr addition.

Raman Spectroscopy: Raman spectroscopy was carried out on a MonoVista Confocal Raman microscope spectrometer using a 514.5 nm argon ion laser. The totality of the instrument power was used in order to get the best signal. The collection optic was set at 100× magnification. The spectrum was collected 30 times. The experiments were done on the powdered samples deposited on a silicon wafer.

Thermal Analysis: Thermogravimetric (TG) curves were obtained using a TA instrument thermal analyzer. The initial and exhausted samples were exposed to an increase in temperature (10 °C min⁻¹) while the nitrogen flow rate was held constant (100 mL min⁻¹). From the TG curves, differential TG (DTG) curves were derived.

Sorption of Nitrogen: Nitrogen isotherms were measured at -196 °C using an ASAP 2010 instrument (Micromeritics). Prior to each measurement, initial and exhausted samples (0.05 g) were outgassed at 120 °C to vacuum 10 Torr. The surface area, S_{BET} (Brunauer-Emmett-Teller method), the micropore volume, V_{mic} (calculated from the t-plot), the mesopore volume, V_{mes} , the total pore volume, V_t , were calculated from the isotherms.

Acknowledgements

This work was supported by ARO (Army Research Office) grant W911NF-10-1-0030 and NSF collaborative grant 0754945/0754979. The authors

are grateful to Professor John Lombardi and Mr. Yi Pan for their help in performing Raman analyses.

Received: December 29, 2010

Revised: January 25, 2011

Published online: April 12, 2011

- [1] J.-R. Li, R. J. Kuppler, H.-C. Zhou, *Chem. Soc. Rev.* **2009**, *38*, 1477–1504.
- [2] G. Férey, *Chem. Soc. Rev.* **2008**, *37*, 191–214.
- [3] P. Wright, in *Microporous framework solids* (Ed.: P. Wright), RSC Publishing, Cambridge, UK, **2008**, pp. 8–78.
- [4] S. L. James, *Chem. Soc. Rev.* **2003**, *32*, 276–288.
- [5] A. U. Czaja, N. Trukhan, U. Muller, *Chem. Soc. Rev.* **2009**, *38*, 1284–1293.
- [6] U. Müller, M. M. Schubert, O. M. Yaghi, in *Chemistry and Applications of Porous Metal–Organic Frameworks* (Eds.: U. Müller, M. M. Schubert, O. M. Yaghi), Wiley-VCH Verlag GmbH & Co. KGaA, **2008**, pp. 247–262.
- [7] Serre C., Millange F., Thouvenot C., Noguès M., Marsolier G., Louër D., Férey G. *J. Am. Chem. Soc.* **2002**, *124*, 13519–13526.
- [8] G. Férey, C. Serre, C. Mellot-Draznieks, F. Millange, S. Surblé, J. Dutour, I. Margiolaki, *Angew. Chem. Int. Ed.* **2004**, *43*, 6296–6301.
- [9] P. Horcajada, S. Surble, C. Serre, D.-Y. Hong, Y.-K. Seo, J.-S. Chang, J.-M. Greneche, I. Margiolaki, G. Férey, *Chem. Commun.* **2007**, 2820–2822.
- [10] P. L. Llewellyn, S. Bourrelly, C. Serre, A. Vimont, M. Daturi, L. Hamon, G. De Weireld, J.-S. Chang, D.-Y. Hong, Y. Kyu Hwang, S. Hwa Jung, G. Férey, *Langmuir* **2008**, *24*, 7245–7250.
- [11] P. Horcajada, S. Serre, M. Vallet-Regí, M. Sebban, F. Taulelle, G. Férey, *Angew. Chem. Int. Ed.* **2006**, *118*, 6120–6124.
- [12] L. D. O'Neill, H. Zhang, D. Bradshaw, *J. Mater. Chem.* **2010**, *20*, 5720–5726.
- [13] M. D. Rowe, D. H. Thamm, S. L. Kraft, S. G. Boyes, *Biomacromolecules* **2009**, *10*, 983–993.
- [14] M. Arnold, P. Kortunov, D. J. Jones, Y. Nedellec, J. Kärger, J. Caro, *Eur. J. Inorg. Chem.* **2007**, 2007, 60–64.
- [15] J. Gascon, S. Aguado, F. Kapteijn, *Microporous Mesoporous Mater.* **2008**, *113*, 132–138.
- [16] Y. Liu, Z. Ng, E. A. Khan, H.-K. Jeong, C.-B. Ching, Z. Lai, *Microporous Mesoporous Mater.* **2009**, *118*, 296–301.
- [17] Y. Yoo, H.-K. Jeong, *Chem. Commun.* **2008**, 2441–2443.
- [18] S. Hermes, D. Zacher, A. Baunemann, C. Wöll, R. A. Fischer, *Chem. Mater.* **2007**, *19*, 2168–2173.
- [19] S. J. Yang, J. Y. Choi, H. K. Chae, J. H. Cho, K. S. Nahm, C. R. Park, *Chem. Mater.* **2009**, *21*, 1893–1897.
- [20] A. Pichon, *Nat. Chem.* **2009**, DOI: 10.1038/nchem.239.
- [21] X. Chen, P. Lukaszczuk, C. Tripisciano, M. H. Rummeli, J. Sremscek-Nazzari, I. Pelech, R. J. Kalenczuk, E. Borowiak-Palen, *Phys. Status Solidi B* **2010**, *10.1002/pssb.201000122*.
- [22] M. Jahan, Q. Bao, J.-X. Yang, K. P. Loh, *J. Am. Chem. Soc.* **2010**, *132*, 14487–14495.
- [23] C. Petit, T. J. Bandoz, *Carbon* **2010**, *49*, 563–572.
- [24] C. Petit, T. J. Bandoz, *Adv. Mater.* **2009**, *21*, 4753–4757.
- [25] C. Petit, T. J. Bandoz, *Adv. Funct. Mater.* **2010**, *20*, 111–118.
- [26] C. Petit, B. Mendoza, T. J. Bandoz, *Langmuir* **2010**, *26*, 15302–15309.
- [27] S. S.-Y. Chui, S. M.-F. Lo, J. P. H. Charmant, A. G. Orpen, I. D. Williams, *Science* **1999**, *283*, 1148–1150.
- [28] H. Li, M. Eddaoudi, M. O'Keeffe, O. M. Yaghi, *Nature* **1999**, *402*, 276–279.
- [29] A. Vimont, J.-M. Goupil, J.-C. Lavalley, M. Daturi, S. Surblé, C. Serre, F. Millange, G. Férey, N. Audebrand, *J. Am. Chem. Soc.* **2006**, *128*, 3218–3227.
- [30] S. Park, R. S. Ruoff, *Nat. Nano* **2009**, *4*, 217–224.
- [31] M. Seredych, C. Petit, A. V. Tamashausky, T. J. Bandoz, *Carbon* **2009**, *47*, 445–456.
- [32] G. Férey, C. Mellot-Draznieks, C. Serre, F. Millange, J. Dutour, S. Surble, I. Margiolaki, *Science* **2005**, *309*, 2040–2042.
- [33] R. C. Weast, M. J. Astle, in *Handbook of Chemistry and Physics*. 62 ed. (Eds.: R. C. Weast, M. J. Astle), CRC Press, Boca Raton, FL, **1981**.
- [34] A. Lerf, H. He, M. Forster, J. Klinowski, *J. Phys. Chem. B* **1998**, *102*, 4477–4482.
- [35] E. Papirer, J. Dentzer, S. Li, J. B. Donnet, *Carbon* **1991**, *29*, 69–72.
- [36] S. C. Ndlela, B. H. Shanks, *Ind. Eng. Chem. Res.* **2003**, *42*, 2112–2121.
- [37] C. Petit, M. Seredych, T. J. Bandoz, *J. Mater. Chem.* **2009**, *19*, 9176–9185.
- [38] M. R. Lohe, M. Rose, S. Kaskel, *Chem. Comm.* **2009**, 2009, 6056–6058.
- [39] S. Hermes, F. Schroder, S. Amirjalayer, R. Schmid, R. A. Fischer, *J. Mater. Chem.* **2006**, *16*, 2464–2472.
- [40] E. Biemmi, T. Bein, N. Stock, *Solid State Sci.* **2006**, *8*, 363–370.
- [41] F. Tuinstra, J. L. Koenig, *J. Chem. Phys.* **1970**, *53*, 1126–1130.
- [42] K. N. Kudin, B. Ozbaz, H. C. Schniepp, R. K. Prud'homme, I. A. Aksay, R. Car, *Nano Lett.* **2008**, *8*, 36–41.
- [43] G. Socrates, in *Infrared and Raman characteristic groups frequencies: tables and charts* (Eds.: G. Socrates), Wiley-VCH Verlag GmbH & Co. KGaA, **2004**, pp. 128–129.
- [44] C. Prestipino, L. Regli, J. G. Vitillo, F. Bonino, A. Damin, C. Lamberti, A. Zecchina, P. L. Solari, K. O. Kongshaug, S. Bordiga, *Chem. Mater.* **2006**, *18*, 1337–1346.
- [45] T. J. Bandoz, C. Petit, *J. Colloid Interf. Sci.* **2009**, *338*, 329–345.
- [46] C. L. McCallum, T. J. Bandoz, S. C. McGrother, E. A. Müller, K. E. Gubbins, *Langmuir* **1998**, *15*, 533–544.
- [47] C. Petit, T. J. Bandoz, *Environ. Sci. Technol.* **2008**, *42*, 3033–3039.
- [48] C. Petit, C. Karwacki, G. Peterson, T. J. Bandoz, *J. Phys. Chem. C* **2007**, *111*, 12705–12714.
- [49] B. Marten, K. Kim, C. Cortis, R. A. Friesner, R. B. Murphy, M. N. Ringnalda, D. Sitkoff, B. Honig, *J. Phys. Chem.* **1996**, *100*, 11775–11788.
- [50] K. Nakamoto, in *Infrared and Raman Spectra of Inorganic and Coordination Compounds, Applications in Coordination, Organometallic, and Bioinorganic Chemistry* (Ed.: K. Nakamoto), Wiley, Hoboken, NJ, **2009**, pp. 62–67.
- [51] B. Levasseur, C. Petit, T. J. Bandoz, *ACS Applied Materials & Interfaces* **2010**, *2*, 3606–3613.
- [52] G. Férey, C. Mellot-Draznieks, C. Serre, F. Millange, *Acc. Chem. Res.* **2005**, *38*, 217–225.
- [53] W. S. Hummers, R. E. Offeman, *J. Am. Chem. Soc.* **1958**, *80*, 1339–1339.



Contents lists available at ScienceDirect

Microporous and Mesoporous Materials

journal homepage: www.elsevier.com/locate/micromeso

MCM-41 impregnated with active metal sites: Synthesis, characterization, and ammonia adsorption

Amanda M.B. Furtado, Yu Wang, T. Grant Glover, M. Douglas LeVan^{*}

Department of Chemical and Biomolecular Engineering, Vanderbilt University, Nashville, TN 37235, USA

ARTICLE INFO

Article history:

Received 30 November 2010

Received in revised form 29 January 2011

Accepted 31 January 2011

Available online 5 March 2011

Keywords:

MCM-41

Ordered mesoporous silica

Metal salt

Ammonia adsorption

Chemisorption

ABSTRACT

Active metal sites incorporated into nanoporous materials have shown potential as novel catalytic adsorbents for the removal of toxic industrial chemicals from air. This work explores the effects of the metal cation, anion, metal oxidation state, pH, solubility, and drying temperature on the ammonia capacity of MCM-41-impregnated samples. The nitrates, chlorides, sulfates, and carbonates of zinc, copper, and iron have been successfully impregnated using a solution method into a mesoporous silica material and characterized via XRD, XPS, adsorption isotherms, and ammonia capacity. The conditioning temperature was found to have a major impact on the ammonia capacity of the impregnated samples. At both 120 °C and 250 °C, the metal type and anion type were determined to be statistically significant predictors of ammonia capacity and the pH and metal oxidation state were not. The solubility of the metal salt in water was also determined to be an ammonia capacity predictor. Overall, ZnCl_2 was found to be most effective at enhancing the ammonia capacity; consequently, this metal salt was analyzed in more detail. Impregnation amounts from 20 to 50 wt% ZnCl_2 in MCM-41 gave high ammonia capacities. The highest capacity achieved was 8.8 mol ammonia/kg adsorbent, which is more than four times the capacity of the base, unimpregnated MCM-41 material.

© 2011 Elsevier Inc. All rights reserved.

1. Introduction

Mesoporous materials with ordered pore structures and large surface areas have shown promise for use in industrial applications ranging from air to water purification. MCM-41 [1], which is a member of the M41S family of siliceous materials, is one popular example of this type of structured mesoporous material. MCM-41 has a hexagonal close-packed structure composed of unidirectional cylindrical channels arranged in a hexagonal manner [2]. This ordered mesoporous material has a high surface area and is an ideal backbone for a well characterized adsorbent.

Ammonia is widely used as an industrial chemical, yet at too high a concentration, it is also hazardous to human health [3]. When ammonia must be removed from waste streams in industrial settings, activated carbons are generally used [4]. These have a large pore size distribution that provides macropores and mesopores to enhance the transport properties throughout the adsorbents and micropores that provide capacity for physical adsorption due to their strong potential wells [5]. Siliceous materials have also been found to have an affinity for ammonia due to

hydrogen bonding interactions between ammonia and hydroxyl groups on the silica surface [6–8]. Ordered mesoporous silicas such as MCM-41 are useful materials for ammonia adsorption due to their high adsorptive potential for ammonia, which is higher than that of unimpregnated carbons [9]. Ordered silicas have high adsorption potential for ammonia due to their polarity; since carbon is a nonpolar substrate, its ability to interact with polar molecules such as ammonia is limited. Similar to current activated carbon materials, ordered mesoporous materials can also be impregnated with active sites to provide chemisorption potential within the adsorbent [10–17]. This would provide both a base structure and impregnants with affinity for ammonia adsorption.

Historically, metal salts have been impregnated within activated carbons to provide active sites for chemisorption [18,19]. Metal salts that have been studied specifically for ammonia removal include zinc chloride [20] and basic copper carbonate [22]. Sulfate containing compounds have also recently been studied for their effects on ammonia removal [23]. Transition metal ions such as copper and iron are reactive due to their unfilled 3d molecular orbitals [24]. Ammonia complexes with the reactive centers of the transition metal complexes, thereby forming coordination compounds by weak chemisorption [25]. The incorporation of zinc reactive sites into MCM-41 for use as a catalyst has been studied extensively [5,26]. The literature in this area is unclear, however, regarding whether the ammonia complexation affinity stems from

^{*} Corresponding author. Address: Vanderbilt University, PMB 351604, 2301 Vanderbilt Place, Nashville, TN 37235-1604, USA. Tel.: +1 615 322 2441; fax: +1 615 343 7951.

E-mail address: m.douglas.levan@vanderbilt.edu (M.D. LeVan).

the metal cation, the salt anion, or from interactions with the entire compound.

Due to the importance of ammonia removal via coordination with metals and the relatively uncharted area of metal salt precursor optimization, the objective of this study is to identify material compositions and preparation techniques that lead to a high ammonia removal capability. To accomplish this, a designed experiment is conducted to measure the effects of metal type, anion type, metal oxidation state, sample pH, and drying temperature on the impregnated MCM-41 materials. The results are analyzed statistically to determine the most important factors yielding high ammonia capacities, and they are also related to the structural characteristics of the metal impregnated samples. After analyzing the ammonia capacities of these samples, the concentration of metal salt in the impregnated material with the highest ammonia capacity is optimized. The most promising samples are characterized via pH measurements, XRD, and N_2 adsorption isotherms.

2. Experimental methods

2.1. Materials

Tetramethylammonium hydroxide pentahydrate, TMAOH (97%), tetramethylammonium silicate solution, TMA Si (99.99%, 15–20 wt% in water), and sulfuric acid (95.0–98.0%) were purchased from Sigma–Aldrich. Hexadecyltrimethylammonium chloride, CTAC (25%) in water was purchased from Pfaltz and Bauer. A solution of ammonium hydroxide (29 wt%) in water, Cab-O-Sil M5, and anhydrous zinc chloride were purchased from Fisher Scientific. All metal salts were purchased from Fisher Scientific and were ACS grade chemicals.

2.2. MCM-41 synthesis

The base siliceous MCM-41 material with a 37 Å pore was synthesized based on the procedure outlined by Glover et al. [28]. Briefly, a solution of 2.4 g of 29 wt% ammonium hydroxide and 21.2 g of 25 wt% CTAC was mixed with a solution of 3.04 g of TMAOH and 20 g of 10 wt% solution of TMA Si. 4.5 g of Cab-O-Sil M5 fumed silica was added to the solution, forming a reaction gel with molar ratios $SiO_2:0.2CTAC:0.4TMAOH:0.03NH_4OH:0.13TMA Si:26.1H_2O$. The reaction gel was stirred for 30 min and placed in a Teflon-lined autoclave and held at 80 °C in an oven for 24 h. The autoclave was removed from the oven after 24 h, cooled to room temperature, and titrated to a pH of 10.0 using concentrated sulfuric acid. It was then returned to the oven and this titration procedure was repeated every 24 h for a total of 3 titrations. After the third titration, the reactor was returned to the oven and held at 80 °C for a final 24 h. The product was filtered and washed with distilled water to remove the remaining surfactant and allowed to dry at room temperature for 48 h. The calcination procedure used to burn the surfactant from the MCM-41 involved heating the as-synthesized MCM-41 in air from room temperature to 540 °C at a rate of 1 °C/min and holding the sample at 540 °C for 10 h.

2.3. Metal impregnation

To produce the initial metal salt-impregnated MCM-41 samples, a wet impregnation [27] was performed. A predetermined weight of metal salt and 0.6 g of MCM-41 were stirred in an aqueous solution for 18 h. Unless otherwise specified, the metal salt impregnation amount corresponded to a Si/metal atomic ratio of 5. After stirring, the aqueous solutions were evaporated in air at 120 °C for 2 h and then half of the resulting dry, impregnated,

Table 1

Metal salts used for impregnation and oxidation state of the metals.

Anion	Metal ion				
	Zn ⁺²	Cu ⁺¹	Cu ⁺²	Fe ⁺²	Fe ⁺³
Cl ⁻¹	✓	✓	✓	✓	✓
NO ₃ ⁻¹	✓	–	✓	–	✓
SO ₄ ⁻²	✓	–	✓	✓	✓
CO ₃ ⁻²	✓	–	✓	–	–

MCM-41 was heated in air in a tube furnace from room temperature to 250 °C with a 5 °C/min increase and held at 250 °C for 2 additional hours. Thus, each metal salt impregnated material heated to two different temperatures was derived from the same batch of material. Previous work in our research group has focused on carbon silica composite materials; consequently, the two conditioning temperatures were chosen to give some insight into the behavior of the metal salt impregnants at low carbonization temperatures in case these samples are used as the silica phase for future CSC materials [28].

Three metals and four different anions were chosen for investigation in this work. The metals, which have the potential for interacting strongly with ammonia, were zinc, copper (I and II), and iron (II and III) [5,18–20,22,29–32]. The anions include the sulfates, carbonates, nitrates, and chlorides of the metals. These pairs resulted in impregnating a total of 14 different metal salts into the MCM-41. Table 1 summarizes the samples investigated in this work, as well as the oxidation state of the metal in each material. Two batches of MCM-41 were used to make a replicate of each impregnated material at both conditioning temperatures.

Statistical analysis of data was performed using the software package JMP 8.0. The models used to describe the data are standard least squares linear regression analyses. In all models, ammonia capacity was set as the dependent variable and the cations and anions were set as individual independent variables. Based on experimental data, linear combinations of each cation and anion were used to calculate coefficients for each independent variable within the model. The result is a predictive model equation that can be used to define the importance of each anion and cation at enhancing ammonia capacity.

2.4. Drying procedure

An initial study was performed to determine how the conditioning temperature of the metal salt impregnated materials affected the ammonia capacity. Five conditioning methods were tested on ZnSO₄-impregnated MCM-41 with a Si/Zn atomic ratio of 5. The conditioning methods were (1) drying under vacuum at room temperature, (2) heating in a convection oven at 60 °C until dry, (3) heating in a convection oven at 120 °C for 2 h, (4) initial heating at 120 °C for 2 h and additional heating using a tubular furnace at 250 °C for 2 h, and (5) initial heating at 120 °C for 2 h and additional heating using a tubular furnace at 540 °C for 10 h. The latter conditioning method mirrors the calcination procedure of the parent MCM-41 material. In this case, the impregnated ZnSO₄ will experience thermal conditions that are the same as during MCM-41 synthesis; consequently, this heating step mimics the thermal decomposition of the metal salt that would occur if it were impregnated into the MCM-41 reaction gel during synthesis.

2.5. Materials characterization

2.5.1. Nitrogen isotherms

Adsorption isotherms were measured at –196 °C using a Micromeritics ASAP 2020 with UHP nitrogen as the analysis gas.

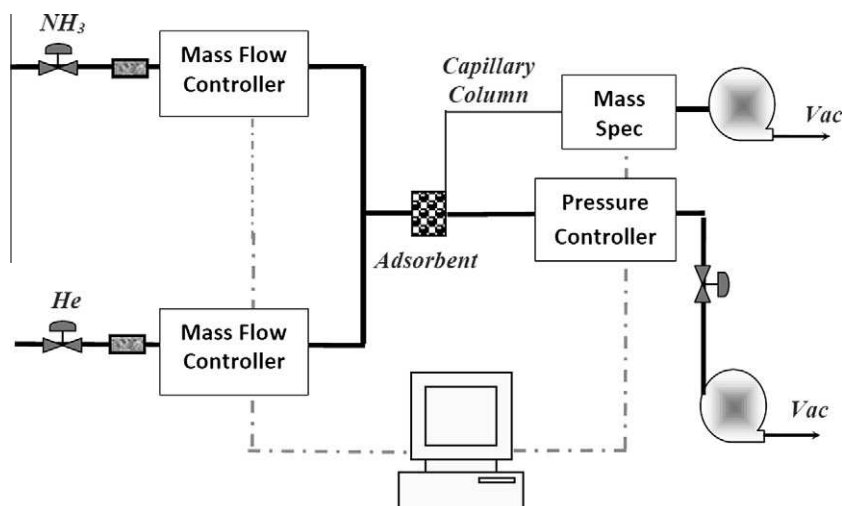


Fig. 1. Schematic of breakthrough apparatus used to determine ammonia capacities.

Prior to measurement, approximately 0.1 g of each sample was degassed for 8 h with heating to 120 °C and vacuuming to 10 μ bar. Density functional theory (DFT) was used to calculate the pore size distribution.

2.5.2. X-ray diffraction

XRD was used to confirm the long range structure of the MCM-41 and to confirm that the metal-impregnated samples also maintained the native MCM-41 structure. The profiles were measured using a Scintag X1h/h automated powder diffractometer with Cu target, a Peltier-cooled solid-state detector, a zero background Si(510) support, and with a copper X-ray tube as the radiation source.

2.5.3. pH

The surface pH of the metal salt impregnated samples was measured using a Hanna Instruments 8242 pH meter with a gel-filled electrode. Determining the solution pH is useful to indicate the overall acidity of the sample once dry; higher sample acidity should correlate to higher ammonia capacity due to acid-base reactions during adsorption [21]. The pH was tested from a stirred solution of 0.1 g of the metal salt impregnated sample and 10 mL of distilled water. The pH of some initial samples was measured after 1, 2, 3, 4, 6, and 18 h of stirring. As these exhibited minimal difference after 4 h, the pH of the remaining samples was measured after 4 and 18 h of equilibration.

2.5.4. X-ray photoelectron spectroscopy

XPS was performed with a PHI Versaprobe XPS Microprobe analysis system manufactured by Physical Electronics, Inc. The apparatus was equipped with a monochromatic Al K(α) X-ray source ($E = 1486.6$ eV). Spectra were collected over binding energies ranging from 1300 to 100 eV, with high resolution sulfur spectra collected over binding energies ranging from 175 to 160 eV. The pass energy was set to 58.7 eV for determination of atomic ratios and binding energies were referenced to the silicon 2p peak [38]. All samples were analyzed twice; once with no additional treatment and once after being crushed to a fine powder to expose the inner surface of MCM-41. Since the XPS yields information on the outer 30–50 Å of the sample, the two analyses allow for determination of the bulk amount of metal salt throughout the sample, as well as determination of the amount of metal salt clustered at the surface of the MCM-41 after impregnation.

2.5.5. Ammonia adsorption

Equilibrium capacities for room temperature ammonia adsorption were measured for all samples using a breakthrough apparatus, a schematic of which is shown in Fig. 1. The concentration of ammonia fed to the adsorbent bed was kept constant at 1133 mg/m³ (1500 ppm_v) in helium. The capacity of the adsorbent material, n (mol ammonia/kg adsorbent), was calculated from

$$n = \frac{F}{m} \int_0^\infty (C_0 - C) dt \quad (1)$$

where C_0 is the feed concentration in units of mol/m³, and C is the effluent concentration at time t . F , the volumetric flow rate of gas through the adsorbent bed, was adjusted from 10 to 50 sccm to give a breakthrough time of approximately 1 h. The mass of the sample, m , was held constant at approximately 10 mg and housed in a small cylindrical adsorbent bed. The ammonia capacity calculated using the breakthrough apparatus had a standard deviation on the order of 3%.

3. Results and discussion

3.1. Materials characterization

3.1.1. Nitrogen isotherms

Two batches of parent MCM-41 used as the base material for impregnations were characterized using nitrogen isotherms. Fig. 2 depicts the nitrogen adsorption isotherm at −196 °C for one batch. The isotherm is typical of a mesoporous MCM-41 material and is Type IV based on the IUPAC classification scheme. The isotherm exhibits an inflection point at relative pressure, P/P_0 , of 0.3, which is characteristic of capillary condensation in the mesopores. Hysteresis due to capillary condensation is also evident in the desorption branch of the isotherm. Table 2 summarizes the physical properties gleaned from the nitrogen adsorption isotherm for both batches. The average pore size of the MCM-41 material was found to be similar for both batches when analyzed using DFT.

The three impregnated materials with the highest average ammonia capacities, MCM-41 impregnated with Cu(NO₃)₂ at 120 °C, ZnCl₂ at 250 °C, and Zn(NO₃)₂ at 120 °C, were analyzed in more detail. Table 3 summarizes the ammonia capacities and material characteristics derived from the nitrogen isotherms for those samples. The addition of metal salts within the MCM-41 resulted in approximately a 40% decrease in the calculated BET

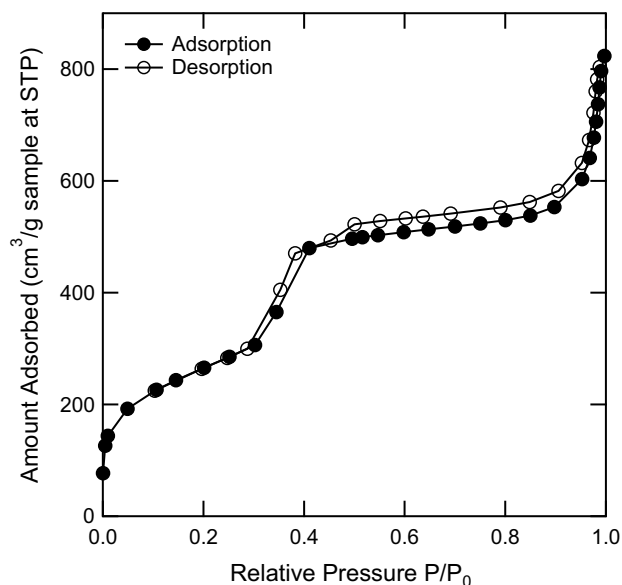


Fig. 2. Nitrogen adsorption isotherm for the parent MCM-41 material.

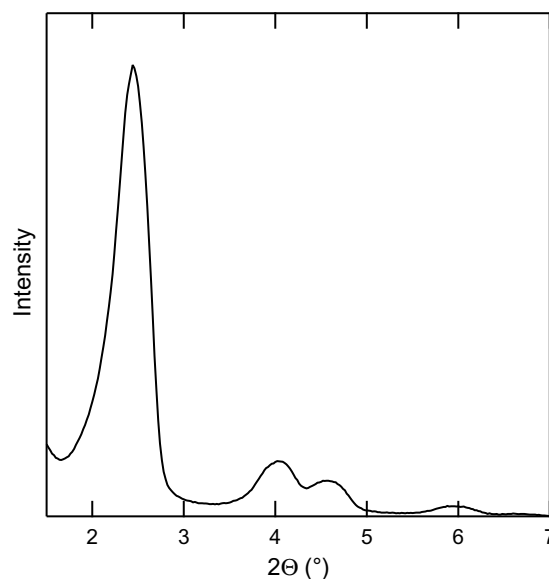


Fig. 3. X-ray diffraction pattern for the parent MCM-41 material.

Table 2

Physical properties of the parent MCM-41 as derived from nitrogen adsorption isotherms.

Property	MCM-41 batch 1	MCM-41 batch 2
S_{BET}	930 m ² /g	916 m ² /g
V_{pore}	1.27 cm ³ /g	1.20 cm ³ /g
d_{DFT}	34.0 Å	37.9 Å

Table 3

Physical properties of the three most promising impregnated materials. Ammonia capacities measured using 1133 mg/m³ ammonia in helium. All samples impregnated with a silicon to metal atomic ratio of 5.

Sample	Avg. NH ₃ capacity (mol/kg)	S_{BET} (m ² /g)	V_{pore} (cm ³ /g)	d_{DFT} (Å)
Cu(NO ₃) ₂ -MCM-41 at 120 °C	6.85	614	0.80	30, 12
ZnCl ₂ -MCM-41 at 250 °C	6.70	400	0.49	31, 13
Zn(NO ₃) ₂ -MCM-41 at 120 °C	6.60	568	0.76	32, 13

surface area for the impregnated samples compared to the parent material. According to the DFT analysis, the average pore size of the samples decreased slightly compared to the parent material. The decreases in surface area and pore size result from the metal salts lining the interior walls of the MCM-41 [13] due to metal salt uptake into the MCM-41 pores.

Four ZnSO₄ impregnated MCM-41 samples were adjusted for pH using sulfuric acid to monitor the effects of pH on ammonia capacity within a sample. Zinc sulfate was chosen as the impregnant because we had previously studied it in-depth at different conditioning temperatures. Nitrogen isotherms on these samples showed a decrease in surface area and pore volume after modification with sulfuric acid.

3.1.2. X-ray diffraction

In addition to the N₂ adsorption isotherm, X-ray diffraction was also used to characterize the parent MCM-41 material shown in Fig. 3. A high degree of structural ordering is indicated by the four discrete sharp peaks in the low angle spectrum [33].

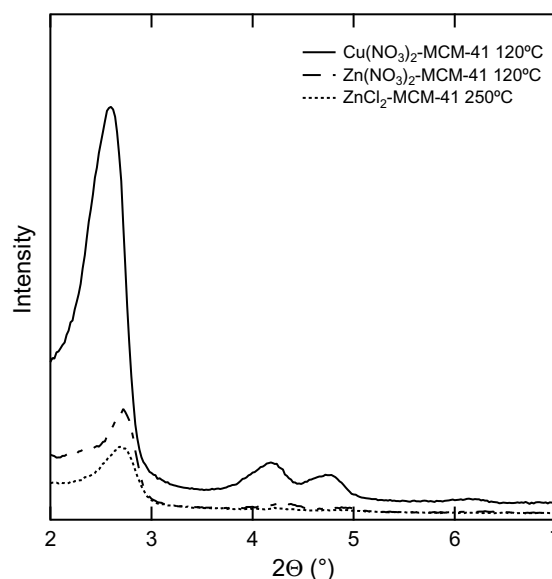


Fig. 4. Small angle XRD scan for some metal-impregnated MCM-41 samples.

As shown in Fig. 4, X-ray diffraction analyses of the three metal-impregnated samples with the highest ammonia capacities confirmed that the zinc and copper salt impregnated materials maintained the long range MCM-41 order. This is indicated by the intense reflection between the low angles of 2.0 and 2.8° 2θ, which corresponds to the (100) basal plane. The materials also exhibit two peaks between 4.0 and 5.0° 2θ, which correspond to the distance between planes (110) and (200).

XRD was also used to characterize the structural change of four ZnSO₄ impregnated MCM-41 samples that were pH adjusted with sulfuric acid to monitor the effects of pH on ammonia capacity within a sample. Fig. 5 depicts the XRD profiles for the four samples, and shows a decrease in the ordering of the MCM-41 matrix with the addition of sulfuric acid. This is consistent with results from the nitrogen isotherms, which depict a decrease in surface area and pore volume after acid treatment.

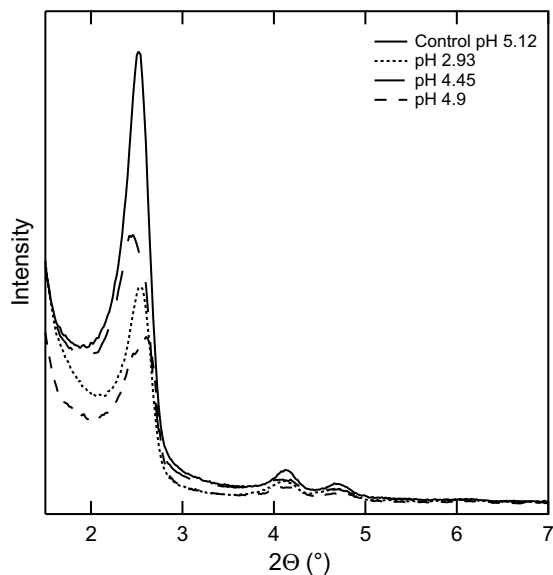


Fig. 5. XRD profiles for the pH-adjusted ZnSO_4 -MCM-41 impregnated samples. The control sample maintains higher order than the acidic samples.

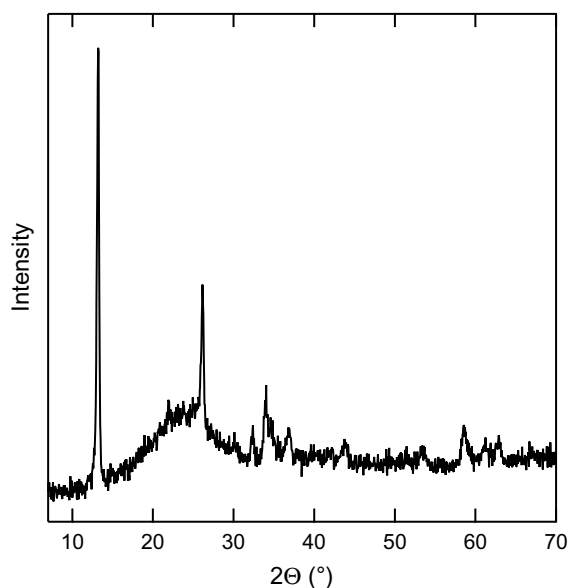


Fig. 6. Large angle XRD scan of the $\text{Cu}(\text{NO}_3)_2$ -MCM-41 sample conditioned at 120 °C. The sample exhibits peaks at 12.7°, 25.5°, and 34°, which correspond to the presence of copper nitrate hydroxide.

XRD scans of the most effective metal salt-impregnated materials identified metal salt crystals in some samples. Specifically, the $\text{Cu}(\text{NO}_3)_2$ -MCM-41 material conditioned at 120 °C showed evidence of copper nitrate hydroxide peaks. As shown in Fig. 6, the sample exhibits reflections at 12.7°, 25.5°, and 34° 2θ , which correspond to the presence of copper nitrate hydroxide crystals [34]. Similar scans of ZnCl_2 -MCM-41 conditioned at 250 °C and $\text{Zn}(\text{NO}_3)_2$ -MCM-41 conditioned at 120 °C did not exhibit the respective metal salt peaks. This is attributed to the formation of small zinc salt crystals that are finely dispersed throughout the MCM-41 material [35].

3.1.3. X-ray photoelectron spectroscopy

XPS was used to decipher the quantity of zinc and sulfur in the ZnSO_4 impregnated samples that were used to determine the most

Table 4

Atomic percentages of species that comprise the ZnSO_4 impregnated material. All samples impregnated with a silicon to metal atomic ratio of 5.

Sample	Atomic % O	Atomic % Si	Atomic % Zn	Atomic % S	Zn/S Ratio
MCM-41	71.8	28.2	–	–	–
ZnSO_4 -MCM-41 120 °C	71.2	27.0	0.8	0.8	1.0
ZnSO_4 -MCM-41 250 °C	70.7	25.5	2.2	1.6	1.4
ZnSO_4 -MCM-41 540 °C	69.6	25.6	3.1	1.6	1.9

effective conditioning method. These quantities are summarized in Table 4. It is evident that the ratio of zinc to sulfur in the 540 °C sample is higher than that found in the other samples. The samples conditioned at 120 °C and 250 °C have Zn/S ratios of approximately 1, whereas the sample conditioned at 540 °C has a ratio of 1.9. This difference in the Zn/S ratio for the high and low temperature samples is consistent with sulfurous compounds being liberated during the high temperature conditioning step and the zinc sulfate converting to zinc oxide and migrating within the walls of MCM-41 [36,37]. For additional verification of the rate process occurring at the high conditioning temperature, another sample of MCM-41 impregnated with ZnSO_4 was heated to 540 °C for 3 days. A comparison of the XPS spectra for the two 540 °C samples and the control sample conditioned at 120 °C is shown in Fig. 7. There is no sulfur peak present in the XPS scan after heating at 540 °C for three days. Consequently, high temperature conditioning decomposes the ZnSO_4 into Zn/ZnO and SO_2/SO_3 , and the sulfurous compounds are liberated from these samples while the Zn remains.

A similar analysis of the uncrushed samples resulted in Zn/Si and Zn/S ratios similar to that of the ground samples. If the metal salt did not successfully migrate within the MCM-41 pores and remained outside of the MCM-41 matrix during impregnation, the Zn/Si ratio of the uncrushed sample would be larger than that of the crushed sample. It is evident from this analysis that the impregnated ZnSO_4 was uniformly distributed throughout the MCM-41 matrix via impregnation.

3.2. Ammonia adsorption

All average ammonia capacities and their standard deviations are listed in Table 5. The standard deviations are higher than 3% be-

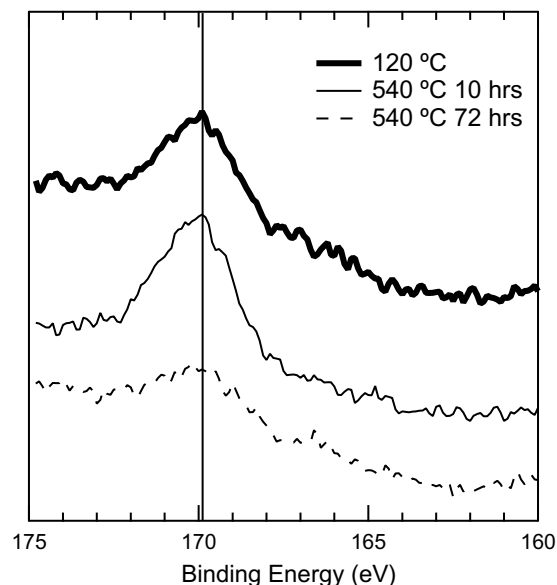
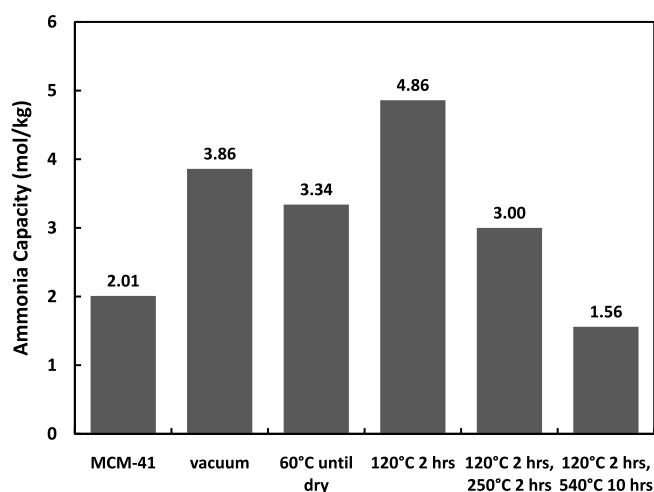


Fig. 7. High resolution XPS spectra of sulfur peaks in the ZnSO_4 -MCM-41 impregnated samples conditioned at 120 °C, 540 °C for 10 h, and 540 °C for 72 h.

Table 5Ammonia capacities for all metal salt impregnated MCM-41 materials for 1133 mg/m³ ammonia in helium. All samples impregnated with a silicon to metal atomic ratio of 5.

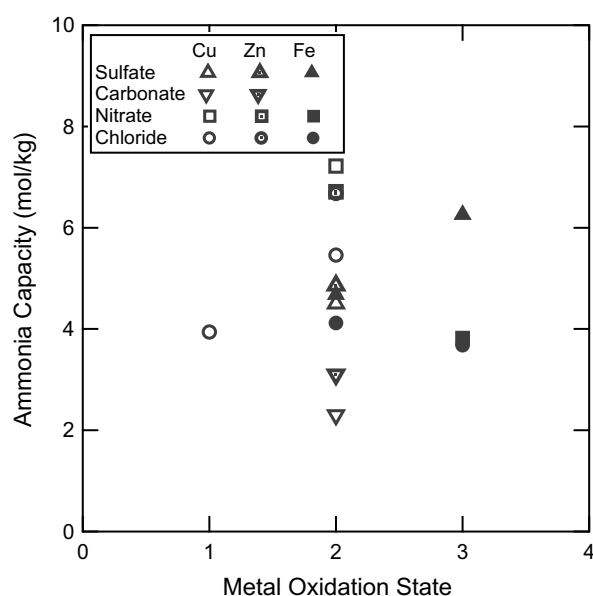
Sample	NH ₃ capacity (mol/kg) 120 °C			Avg. NH ₃ capacity (mol/kg) 120 °C	NH ₃ capacity (mol/kg) 250 °C			Avg. NH ₃ capacity (mol/kg) 250 °C
	batch 1	batch 2	batch 3		batch 1	batch 2	batch 3	
ZnSO ₄ -MCM-41	4.86	7.8	6.47	6.38 ± 1.47	3.02	5.69		4.36 ± 1.88
CuSO ₄ -MCM-41	4.5	6.8	4.71	5.65 ± 1.62	4.79	5.04		4.92 ± 0.17
FeSO ₄ -MCM-41	4.68	5.17		4.93 ± 0.34	3.5	4.84		4.17 ± 0.94
Fe ₂ (SO ₄) ₃ -MCM-41	6.26	6.24		6.25 ± 0.01	6.02	5.39		5.71 ± 0.44
Zn(NO ₃) ₂ -MCM-41	6.71	6.50		6.61 ± 0.15	5.0	4.44		4.72 ± 0.39
Cu(NO ₃) ₂ -MCM-41	7.22	6.47		6.85 ± 0.53	3.17	3.65		3.41 ± 0.34
Fe(NO ₃) ₃ -MCM-41	3.82	4.10		3.96 ± 0.19	3.57	5.10		4.34 ± 1.08
ZnCO ₃ -MCM-41	3.10	3.17		3.14 ± 0.05	2.95	2.90		2.93 ± 0.03
CuCO ₃ -MCM-41	2.30	2.64		2.47 ± 0.24	2.54	2.52		2.53 ± 0.01
ZnCl ₂ -MCM-41	6.68	6.15	5.85	6.23 ± 0.42	7.5	5.95	6.66	6.70 ± 0.77
CuCl-MCM-41	3.94	4.54		4.24 ± 0.42	4.21	4.43		4.32 ± 0.15
CuCl ₂ -MCM-41	5.46	4.82		5.14 ± 0.45	4.66	4.17		4.42 ± 0.35
FeCl ₂ -MCM-41	4.12	4.43		4.28 ± 0.22	3.01	3.14		3.08 ± 0.09
FeCl ₃ -MCM-41	3.68	4.40		4.04 ± 0.51	3.72	3.72		3.72 ± 0.00

**Fig. 8.** The effect of drying temperature on the ammonia capacity for the ZnSO₄-MCM-41 impregnated material.

cause each average capacity was calculated using samples that were impregnated using two synthesis batches of MCM-41. Consequently, the standard deviations reflected in the table are representative primarily of differences between samples rather than deviation in ammonia capacity measurement.

After varying the conditioning temperature, the ZnSO₄-MCM-41 samples were tested for their ammonia capacity. This information is summarized in Fig. 8. It is evident from this figure that the sample held at 540 °C resulted in the lowest ammonia capacity of all ZnSO₄ impregnated samples. From this information, coupled with the XPS data for these samples, it is evident that more zinc and zinc oxide forms in the higher temperature sample versus the sample conditioned at 120 °C because the zinc sulfate decomposes during the high temperature heating. The depletion of zinc sulfate in the sample decreases the effectiveness of ammonia chemisorption. Because industrial applications of these materials often require high temperatures for synthesis and regeneration, the conditioning steps at 120 °C and 250 °C were chosen for investigation in the remaining samples.

Fig. 9 depicts a lack of correlation between the ammonia capacity and the metal oxidation state of the impregnated samples conditioned at 120 °C. A similar trend was evident for the samples conditioned at 250 °C. For the metal salts tested, zinc always remains in the +2 oxidation state, copper varies from +1 to +2, and iron varies from +2 to +3. Based on this analysis, the metal type was determined to be more important in affecting the ammonia

**Fig. 9.** Ammonia capacity dependence on metal oxidation state for the impregnated materials.

capacity than the cation oxidation state at both conditioning temperatures. The lack of statistical significance can be expected because the chemisorption reactions occur based on the metal salt type rather than just on the oxidation state of the cation or anion [3]. As an example, the +2 oxidation states of copper, iron, and zinc compounds differ drastically in their reactivity towards ammonia, with average ammonia capacities ranging from 2.47 to 6.38 mol/kg. These can be compared to the ammonia capacity of the base, unimpregnated MCM-41, which is 2.0 mol/kg. Consequently, analyzing the impregnated materials based on their cationic oxidation states would combine the effects of the +2 oxidation states of zinc, copper, and iron, and negate the important differences in ammonia capacity that are inherent in the metal type used as the impregnant.

The pH was also expected to play an important role in ammonia capacity because ammonia is a basic gas that can participate in acid-base reactions. The intrinsic pH was measured during the aqueous impregnation step, when the same amount of water and MCM-41 was present in all samples. The pH measurement provides an indication of the acidity of the dry samples and may be used to predict the sample's affinity for participating in acid-base reactions [21]. The only difference affecting the pH of the samples

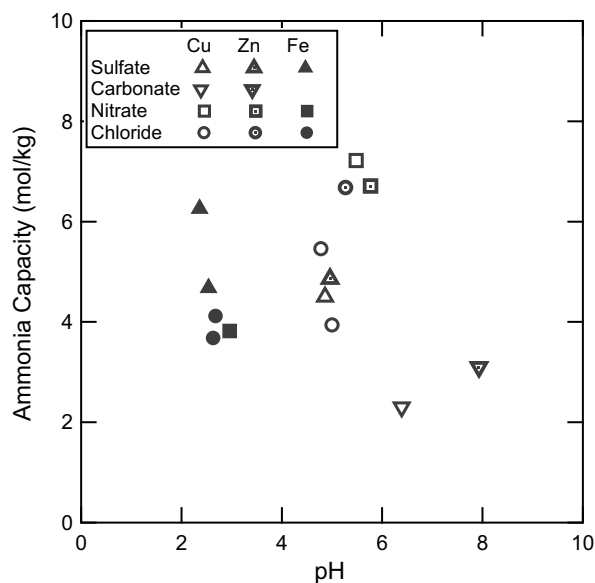


Fig. 10. Ammonia capacity dependence on pH for the impregnated materials.

is the presence of different metal salt impregnants. As shown in Fig. 10, a lack of statistical correlation was found between the ammonia capacity and the pH of the MCM-41 samples impregnated with different metals. This figure compares the ammonia capacity of metal salt impregnated samples with different intrinsic pH values based on the acidic properties of the metal salt impregnants.

An additional study was performed to determine the effect of varying pH on one of the metal salt impregnated samples. During synthesis of ZnSO_4 -MCM-41, the pH of the mixture of water, ZnSO_4 , and MCM-41 was adjusted using H_2SO_4 so as not to introduce new anions into the solution. The pH of these mixtures and the ammonia capacity of the final samples were compared. Based on the standard deviation associated with the ammonia capacity of the ZnSO_4 impregnated samples, this study showed no significant difference among the ammonia capacities of the pH-adjusted samples. As shown in Fig. 11, the ammonia capacity was highest

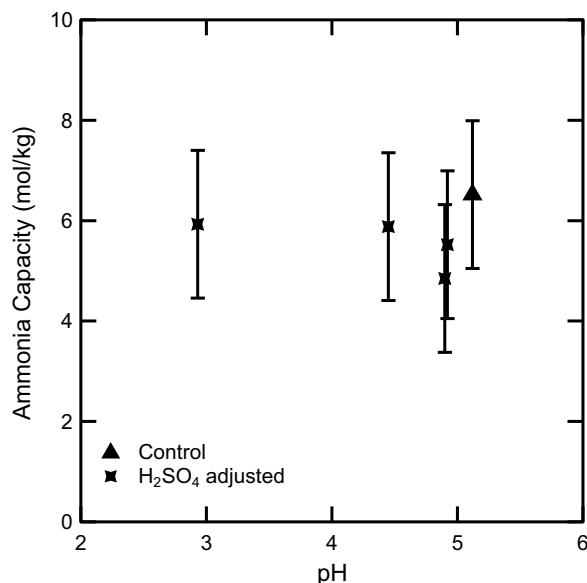


Fig. 11. Ammonia capacity compared to pH of ZnSO_4 -MCM-41 with pH adjusted by H_2SO_4 .

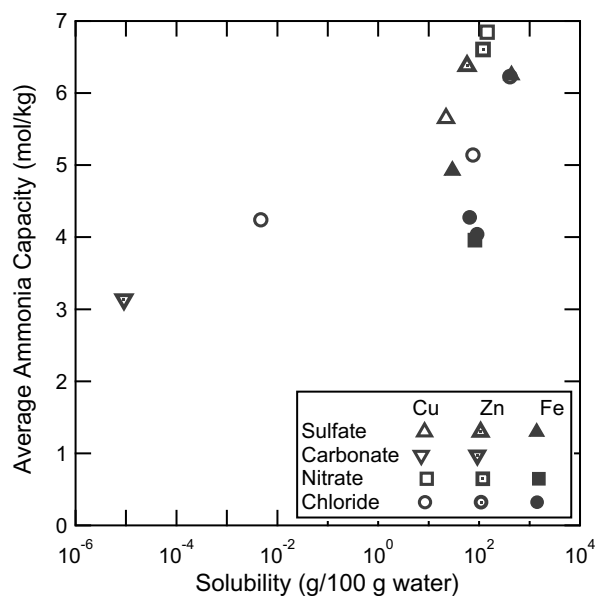


Fig. 12. Ammonia capacity for samples conditioned at 120 °C compared to metal salt solubility.

for the control sample due to it remaining the most ordered material, which was shown via XRD in Fig. 5. However, taking into account the standard deviation associated with each sample, a more acidic solution pH did not correspond to a statistically significant increase in ammonia capacity.

The next parameter investigated was the aqueous solubility of the metal salt. Because the impregnation of MCM-41 was performed in an aqueous solution, Fig. 12 shows that the most insoluble metal salts, CuCl , ZnCO_3 , and CuCO_3 , also correspond to the lowest ammonia capacities at the 120 °C conditioning temperature. Fig. 13 depicts a similar result for the samples conditioned at 250 °C. The decrease in ammonia capacity with respect to solubility is a result of low dispersion of the nearly insoluble metal salt within the MCM-41 matrix. Low solubility allows for aggregation of the metal salt and thereby decreases the surface area available for chemisorption with ammonia.

Statistical analysis of all samples conditioned at 120 °C shows that the metal type and anion type have the greatest effect on ammonia capacity. The analysis shows that both of these variables have low enough p -values, a common factor in statistical analysis, that they are statistically significant predictors of ammonia capacity.

$$\text{Ammonia capacity} = 4.43 + \begin{pmatrix} -0.58 & \text{Cu}^{+1} \\ 0.45 & \text{Cu}^{+2} \\ -0.55 & \text{Fe}^{+2} \\ -0.49 & \text{Fe}^{+3} \\ 1.17 & \text{Zn}^{+2} \end{pmatrix} + \begin{pmatrix} -2.43 & \text{CO}_3^{-2} \\ 0.39 & \text{Cl}^{-1} \\ 0.99 & \text{NO}_3^{-1} \\ 1.04 & \text{SO}_4^{-2} \end{pmatrix}$$

This model equation represents the statistics associated with the observed ammonia capacities and the metals and anions impregnated within the samples. The more positive or negative the coefficient, the larger the significance of that variable on the ammonia capacity. Consequently, zinc is the most effective metal at enhancing the ammonia capacity of the impregnated materials and Cu^{+1} is the least effective. At this temperature, the sulfates and nitrates show the most effectiveness at enhancing ammonia capacity, and carbonates are the least effective. From this analysis, it is evident that ZnSO_4 and $\text{Zn(NO}_3)_2$ impregnated into MCM-41 result in the highest ammonia capacities at the 120 °C conditioning temperature.

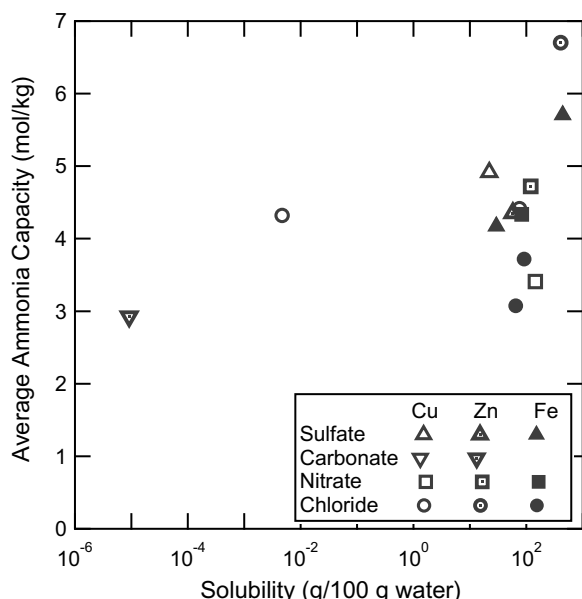


Fig. 13. Ammonia capacity for samples conditioned at 250 °C compared to metal salt solubility.

A similar analysis was carried out using the samples conditioned at 250 °C. As in the previous analysis, the metal and anion type were found to be the most statistically significant predictors of ammonia capacity. Analysis of these data produced the model equation

$$\text{Ammonia capacity} = 3.83 + \begin{pmatrix} -0.13 \text{ Cu}^{+1} \\ -0.02 \text{ Cu}^{+2} \\ -1.03 \text{ Fe}^{+2} \\ -0.23 \text{ Fe}^{+3} \\ 0.95 \text{ Zn}^{+2} \end{pmatrix} + \begin{pmatrix} -1.57 \text{ CO}_3^{-2} \\ 0.62 \text{ Cl}^{-1} \\ -0.06 \text{ NO}_3^{-1} \\ 1.02 \text{ SO}_4^{-2} \end{pmatrix}$$

At 250 °C zinc is the most effective metal at enhancing ammonia capacity and iron is the least effective. For the anions, the sulfates and chlorides provide the most ammonia capacity enhancement and the carbonates provide the least.

The sample in this group with the highest ammonia capacity was the ZnCl_2 impregnated MCM-41 sample, with an average experimental ammonia capacity of 6.70 mol/kg. Table 5 summarizes the ammonia capacities for the metal impregnated samples at both conditioning temperatures, their average values, and the standard deviations associated with the averages for the metal salt impregnated samples. Fig. 14 summarizes the data in a parity plot comparing the actual average ammonia capacities at both conditioning temperatures to the predicted capacities.

Analysis of variance using all data shows that the conditioning temperature plays a significant role in the ammonia capacity of the final samples. This is evident in the models derived for both conditioning temperatures, where the intercept in each equation represents the average ammonia capacity across all samples. The intercept at the 120 °C conditioning temperature is larger than that of the model constructed from the samples conditioned at 250 °C. Thus, the ammonia capacities tend to be higher for the samples conditioned at the lower temperature.

At both conditioning temperatures, the metal carbonate impregnants resulted in low ammonia capacities. One explanation for this is their minimal solubility in water, which inhibits a fine dispersion of these metal salts throughout the silica matrix, and decreases the surface area available for chemisorption when compared to more soluble metal salts. Another explanation can be

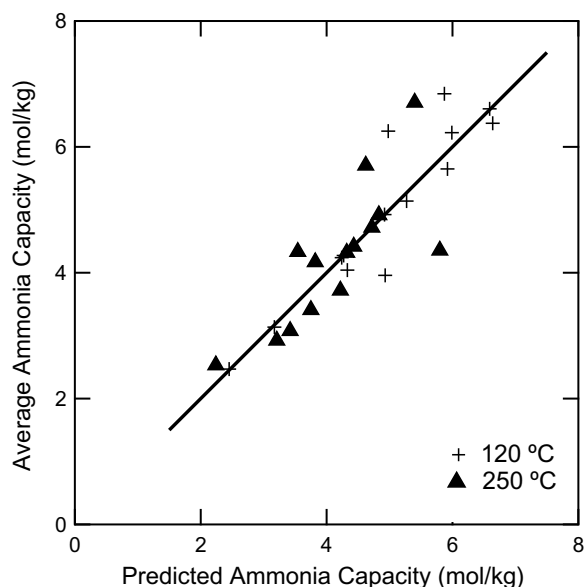
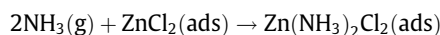


Fig. 14. Parity plot comparing the actual average and predicted values of the ammonia capacities at both conditioning temperatures.

gleaned from an analysis of the melting points of these materials. Carbonates generally have low melting points; ZnCO_3 has a melting point of 140 °C and CuCO_3 has a melting point of 200 °C, after which the carbonates decompose to their corresponding metals and metal oxides [39]. As shown in the temperature study of the ZnSO_4 impregnated samples, the decomposition of the metal salt decreases the ammonia capacity of the impregnated samples. Consequently, due to their low melting points and low solubilities, the metal carbonate impregnated samples exhibit the lowest ammonia capacities compared to all other materials.

The most effective impregnant at both conditioning temperatures was determined to be ZnCl_2 . When conditioned at 120 °C, this sample exhibited an average ammonia capacity of 6.2 mol/kg. After conditioning at 250 °C, the average capacity rose to 6.7 mol/kg. ZnCl_2 as an impregnant resulted in samples with high ammonia capacities at both conditioning temperatures, compared to other metal salts that promoted high ammonia capacities at 120 °C but resulted in lower ammonia capacities after conditioning at the higher temperature. Consequently, ZnCl_2 was identified as the most robust metal salt impregnant.

This research into different metal salts has shown that both the cation and anion play an important role in complexing with the adsorbate molecule. Two coordination compounds between ZnCl_2 and NH_3 are proposed in the literature. Fortier et al. [5] proposed the formation of $\text{ZnCl}_2(\text{NH}_3)_x$ after impregnating activated carbon with varying concentrations of the metal salt and monitoring the reaction with ammonia. They initially proposed 2 for the value of x , as seen in the reaction below.



This reaction has been reported by other sources as the reaction occurring when gaseous ammonia reacts with aqueous suspensions of ZnCl_2 [40,41]. Fortier et al. concluded that under adsorption conditions, the value of x depends on the partial pressure of ammonia above the coordination compound. In the presence of water, Petit et al. [20] confirmed the formation of $\text{ZnCl}_2(\text{NH}_4)\text{Cl}$ using XRD, XRF, and FTIR analytical techniques. Because the equilibrium capacities in this study were determined under dry conditions, it is evident that $\text{ZnCl}_2(\text{NH}_3)_x$ is formed during adsorption.

The ZnCl_2 -MCM-41 sample conditioned at the higher temperature was used as the basis for optimizing the amount of zinc chloride loaded within the MCM-41 support. Fig. 15 shows the dependence of the ammonia capacity on the weight percent of zinc chloride impregnated into MCM-41. The 0 wt% sample consists only of MCM-41 and the 100 wt% sample consists of only zinc chloride. Table 6 gives the weight percentage of zinc chloride as the silicon to zinc atomic ratio. It is evident from Fig. 15 that the ammonia capacity reaches a maximum at 50 wt% zinc, corresponding to a Si/Zn atomic ratio of 2.3. After this maximum, the zinc chloride can no longer effectively disperse throughout the silica matrix, which causes clumping of the zinc chloride and a decreased zinc chloride surface area for chemisorption. This corresponds to a decrease in ammonia capacity for the samples impregnated with

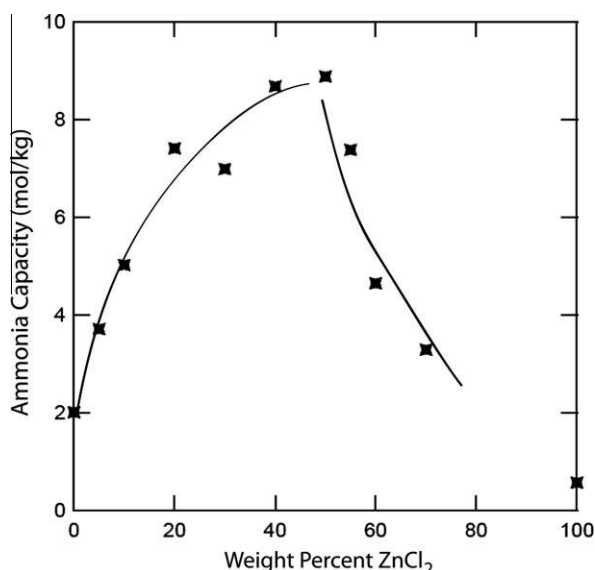


Fig. 15. Comparison of ammonia capacities for different amounts of ZnCl_2 impregnated into MCM-41 and conditioned at 250 °C.

Table 6

Ammonia capacities and Si/Zn molar ratios of the ZnCl_2 impregnated MCM-41 samples. Capacities measured using 1133 mg/m³ ammonia in helium.

wt% ZnCl_2	Si/Zn molar ratio	NH_3 capacity (mol/kg)
0		2.01
5	43.2	3.71
10	20.4	5.02
20	9.1	7.41
30	5.3	6.99
40	3.4	8.68
50	2.3	8.88
60	1.5	4.65
70	0.97	3.29
100		0.57

Table 7

BET surface areas and pore volumes for MCM-41 impregnated with increasing amounts of ZnCl_2 .

wt% ZnCl_2	S_{BET} (m ² /g)	V_{pore} (cm ³ /g)
0	930	1.3
10	816	1.0
30	582	0.7
50	396	0.4
70	170	0.2

higher concentrations of ZnCl_2 . Nitrogen isotherms for select samples, summarized in Table 7, confirm a decrease in surface area and pore volume after impregnation with ZnCl_2 . When considering industrial applications of these materials, impregnant amounts ranging from 20 to 50 wt% ZnCl_2 all yield high ammonia capacities.

4. Conclusions

MCM-41 samples impregnated with metal salts have been prepared via an aqueous impregnation method and conditioned at different temperatures. These samples were tested for material characteristics and ammonia capacity.

The initial ZnSO_4 impregnation study determined that the conditioning temperature has an effect on the ammonia capacity of the impregnated samples. A high temperature conditioning step resulted in the formation of Zn and ZnO from decomposition of ZnSO_4 . A corresponding decrease in ammonia capacity was observed for the high temperature sample compared to those conditioned at lower temperatures.

At both the 120 °C and 250 °C conditioning temperatures, the intrinsic metal salt pH and metal oxidation state were determined not to be statistically significant ammonia capacity predictors. Insoluble metal salts, specifically the metal carbonates, were found to have lower ammonia capacities at both conditioning temperatures due to the aqueous impregnation method used.

The metal type and anion type were found to be the most statistically significant predictors of ammonia capacity for the impregnated samples. For samples at both conditioning temperatures, zinc was identified as the metal yielding the highest ammonia capacity. At 120 °C, the anions yielding the highest ammonia capacities were the sulfates and nitrates, whereas at 250 °C, the sulfates and chlorides were the most effective. At both conditioning temperatures, impregnating with the carbonates resulted in the lowest ammonia capacities.

Across all samples and conditioning temperatures, the MCM-41 sample impregnated with ZnCl_2 and conditioned at 250 °C resulted in the highest average ammonia capacity. Consequently, the concentration of ZnCl_2 impregnated into MCM-41 was optimized for this condition. The ammonia capacity is the highest for MCM-41 impregnated with 50 wt% ZnCl_2 , which corresponds to a Si/Zn molar ratio of 2.3. The ammonia capacity remains high between 20 wt% ZnCl_2 and 50 wt% ZnCl_2 ; there is less than a 25% change between the ammonia capacities in this range of impregnated samples. After 50 wt% ZnCl_2 loading, the ammonia capacity decreases because the metal salt is present at too high a concentration to be well dispersed throughout the MCM-41 matrix.

Acknowledgment

We are grateful to the US Army Edgewood Chemical and Biological Center for the support of this research.

References

- [1] C.T. Kresge, M.E. Leonowicz, W.J. Roth, J.C. Vartuli, J.S. Beck, *Nature* 359 (1992) 710–712.
- [2] B. Marler, U. Oberhagemann, S. Vortmann, H. Gies, *Microporous Mater.* 6 (1996) 375–383.
- [3] W.A. Noyes, *Military Problems with Aerosols and Nonpersistent Gases*, Summary Technical Report of Division 10, National Defense Research Committee, Washington, DC, 1946.
- [4] Department of Health and Human Services, National Institutes of Occupational Safety and Health, 2003.
- [5] H. Fortier, P. Westreich, S. Selig, C. Zelenietz, J.R. Dahn, *J. Colloid Interface Sci.* 320 (2008) 423–435.
- [6] B.A. Morrow, I.A. Cody, L.S.M. Lee, *J. Phys. Chem.* 79 (1975) 2405–2408.
- [7] B.A. Morrow, I.A. Cody, *J. Phys. Chem.* 80 (1976) 1998–2004.
- [8] S. Kittaka, M. Morimura, S. Ishimaru, A. Morino, K. Ueda, *Langmuir* 25 (2009) 1718–1724.
- [9] N. Chino, T. Okubo, *Microporous Mesoporous Mater.* 87 (2005) 15–22.

- [10] V. Ravat, D.B. Mantri, P. Selvam, P. Aghalayam, J. Mol. Catal. A: Chem. 314 (2009) 49–54.
- [11] C. Chanquia, K. Sapag, E. Rodriguez-Castellon, E. Herrero, G. Eimer, J. Phys. Chem. C 114 (2010) 1481–1490.
- [12] D. Lensveld, J. Mesu, A. van Dillen, K. de Jong, Microporous Mesoporous Mater. 44–45 (2001) 401–407.
- [13] R. Savidha, A. Pandurangan, Appl. Catal. A 262 (2004) 1–11.
- [14] D.A. Sheppard, C.E. Buckley, Int. J. Hydrogen Energy 33 (2008) 1688–1692.
- [15] A. Vinu, K. Nandhini, V. Murugesan, W. Bohlmann, V. Umamaheswarl, A. Poppl, M. Hartmann, Appl. Catal. A 265 (2004) 1–10.
- [16] C. Wu, Q. Gao, J. Hu, Z. Chen, W. Shi, Microporous Mesoporous Mater. 117 (2009) 165–169.
- [17] A. Gervasini, C. Messi, P. Carniti, A. Ponti, N. Ravasio, F. Zaccheria, J. Catal. 262 (2009) 224–234.
- [18] L.M. LeLeuch, T.J. Bandoz, Carbon 45 (2007) 568–578.
- [19] C. Canals-Batile, A. Ros, M.A. Lillo-Rodenas, E. Fuente, M.A. Montes-Moran, M.J. Martin, A. Linares-Solano, Carbon 46 (2008) 176–178.
- [20] C. Petit, C. Karwacki, G. Peterson, T.J. Bandoz, J. Phys. Chem. C 111 (2007) 12705–12714.
- [21] M. Seredych, T.J. Bandoz, J. Phys. Chem. C 114 (2010) 14552–14560.
- [22] J.W.H. Smith, P. Westreich, L.M. Croll, J.H. Reynolds, J.R. Dahn, J. Colloid Interface Sci. 337 (2009) 313–321.
- [23] C. Petit, K. Kante, T.J. Bandoz, Carbon 48 (2010) 654–667.
- [24] C.J. Jones, d-and f-Block Chemistry, Royal Society of Chemistry, Cambridge, 2001.
- [25] M.R.A. Blomberg, P.E.M. Siegbahn, M. Svensson, Inorg. Chem. 32 (1993) 4218–4225.
- [26] S.K. Bhargava, D.B. Akolekar, J. Colloid Interface Sci. 281 (2005) 171–178.
- [27] The International Union of Pure and Applied Chemistry, Pure and Applied Chemistry 67 (1995) 1257–1306.
- [28] T.G. Glover, K.I. Dunne, R.J. Davis, M.D. LeVan, Microporous Mesoporous Mater. 111 (2008) 1–11.
- [29] J. Silvestre-Albero, A. Sepulveda-Escribano, F. Rodriguez Reinoso, Microporous Mesoporous Mater. 113 (2008) 362–369.
- [30] M. Naderi, J.L. Pickett, M.J. Chinn, D.R. Brown, J. Mater. Chem. 12 (2002) 1086–1089.
- [31] T. Hasegawa, Y. Shirotori, K. Ozawa, K. Edamoto, K. Takahashi, Appl. Surf. Sci. 237 (2004) 352–357.
- [32] C.-M. Hung, Aerosol. Air Qual. Res. 8 (2008) 447–458.
- [33] D. Trong On, S.M.J. Zaidi, S. Kaliaguine, Microporous Mesoporous Mater. 22 (1998) 211–224.
- [34] International Centre for Diffraction Data, Powder Diffraction File: Alphabetical Indexes: Sets 1–46, Newtown Square, PA, 1996.
- [35] T. Tsoncheva, J. Rosenholm, M. Linden, F. Kleitz, M. Tiemann, L. Ivanova, M. Dimitrov, D. Paneva, I. Mitov, C. Minchev, Microporous Mesoporous Mater. 112 (2008) 327–337.
- [36] R. Narayah, A. Tabatabaie-Raissi, M.J. Antal, Ind. Eng. Chem. Res. 27 (1988) 1050–1058.
- [37] W. Suchanek, J. Cryst. Growth 312 (2009) 100–108.
- [38] J.F. Moulder, W.F. Stickle, P.E. Sobol, K.D. Bomben, Handbook of X-ray Photoelectron Spectroscopy: A Reference of Standard Spectra for Identification and Interpretation of XPS Data, Chigasaki City, Japan, 2007.
- [39] D.R. Lide, W.M. Haynes, CRC Handbook of Chemistry and Physics, CRC Press, Boca Raton, 2009.
- [40] C. Perchard, A. Novak, Spectrochimica Acta 26A (1970) 871–881.
- [41] P.J. Gardner, P. Pang, S. Preston, Thermochemica Acta 138 (1989) 371–374.

Chemistry and reactivity of dinuclear iron oxamate complexes: alkane oxidation with hydrogen peroxide catalysed by an oxo-bridged diiron(III) complex with amide and carboxylate ligation [☆]

Emilio Pardo ^a, Francesc Lloret ^a, Rosa Carrasco ^a, M. Carmen Muñoz ^b,
Tomàs Temporal-Sánchez ^c, Rafael Ruiz-García ^{c,*}

^a Departament de Química Inorgànica, Universitat de València, Dr. Moliner 50, 46100 Burjassot, València, Spain

^b Departamento de Física Aplicada, Universidad Politécnica de Valencia, 46071 Valencia, Spain

^c Departament de Química Orgànica, Universitat de València, Dr. Moliner 50, 46100 Burjassot, València, Spain

Received 6 February 2004; accepted 14 February 2004

Available online 20 March 2004

Abstract

A new dinuclear iron(III) complex with the tetradentate ligand *N,N'*-*o*-phenylenebis(oxamate) (opba) has been synthesised, and structurally, magnetically and electrochemically characterised. It possesses an unprecedented triply bridged Fe₂(μ-O)(μ-RCO₂···H₂O···O₂CR)₂ core, whereby two *N*-amides from the opba ligand complete the square-pyramidal coordination sphere of the *O*-carboxylate rich iron site (Fe–N = 2.053 Å and Fe–O = 2.015 Å). The antiferromagnetic exchange interaction between the two high-spin Fe^{III} ions through the oxo bridge ($J = -190 \text{ cm}^{-1}$; $H = -JS_1 \cdot S_2$) is weaker than that found in related μ-oxo singly bridged diiron(III) complexes. The lessened antiferromagnetic coupling correlates to the remarkably long Fe–O distance ($R = 1.808 \text{ Å}$), which is associated to the relatively bent Fe–O–Fe angle ($\alpha = 131.8^\circ$) in the Fe₂O unit. It experiences an irreversible one-electron oxidation process in acetonitrile at 25 °C ($E = 0.63 \text{ V}$ versus SCE) to give the putative mixed-valent diiron(III,IV) species which is unstable under the experimental conditions. The reactivity of this unique oxo-bridged diiron(III) oxamate complex toward hydrogen peroxide activation and hydrocarbon oxidation in the presence of dioxygen has been examined. It catalyses the oxidation of alkanes like cyclohexane and adamantane to the corresponding alcohols and ketones by H₂O₂ and O₂ in acetonitrile at room temperature with limited catalytic activities (total yields of ca. 5% after 24 h) and modest selectivities ($A/K = 0.9$, KIE = 2.4, *tert*/*sec* = 3.0). Overall, these results are more in line with a mechanism involving alkyl radicals as transient intermediates, although they do not exclude the possibility that a metal-based active oxidant is also involved in this C–H bond oxidation chemistry.

© 2004 Elsevier B.V. All rights reserved.

Keywords: Alkanes; Amides; Carboxylates; Catalysis; Iron; Oxidations

1. Introduction

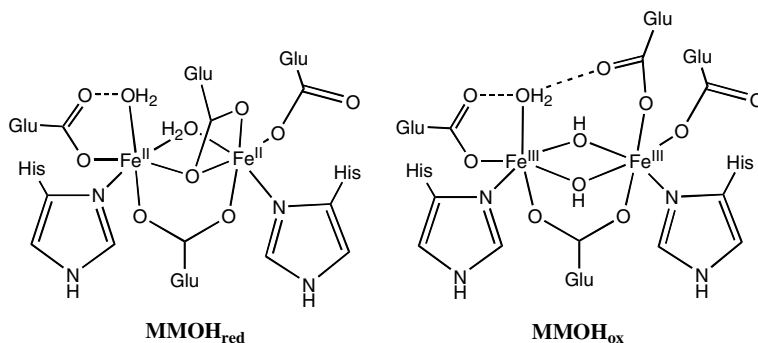
Dinuclear iron complexes have been long considered as synthetic models of the active site from a large class of non-heme diiron enzymes which exhibit diverse redox as well as non-redox (hydrolytic) biological functions [1]. Prominent among these is soluble methane monooxygenase (MMO), a three-component protein that cataly-

ses the selective oxidation of methane to methanol with dioxygen and NADH in methanotropic bacteria [2]. Dioxygen activation and subsequent methane oxidation occur at the hydroxylase component of soluble methane monooxygenase (MMOH), where the hydroxo- and/or carboxylate-bridged diiron active site in various oxidation states is embedded (Scheme 1) [3]. In addition to this oxygenase-type reactivity, which includes other substrates such as alkanes, alkenes and arenes [4], MMOH is also capable of undergoing oxidation reactions when hydrogen peroxide is used instead (peroxidase-type reactivity) [5]. Surprisingly, the vast majority of oxo- and hydroxo-bridged diiron model complexes

[☆] Supplementary data associated with this article can be found, in the online version, at doi: 10.1016/j.ica.2004.02.023.

* Corresponding author. Tel.: +34963544810; fax: +34-96354-4328.

E-mail address: rafael.ruiz@uv.es (R. Ruiz-García).

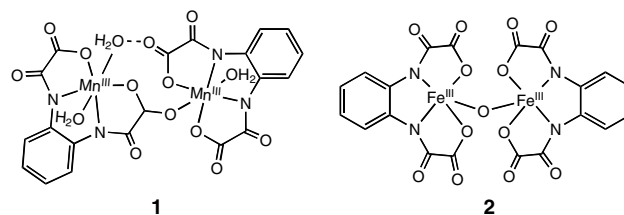


Scheme 1. Structural representation of different redox states of the diiron active site of the hydroxylase component of soluble methane monooxygenase from *Methylococcus capsulatus*.

that act as catalysts for the oxidation of hydrocarbons are those possessing an all-nitrogen ligation which does not reproduce the combination of histidine and glutamate residues actually found in MMOH (Scheme 1) [6,7]. The interest is then directed toward carboxylate-bridged diiron model complexes with terminal ligands that afford a more-oxygen rich metal environment similar to that of the enzyme active site, in order to understand how this structural feature relates to their distinct electronic and reactivity properties [8–10].

In this context, it has been recently shown that the acyclic polychelating ligand *N,N'*-*o*-phenylenebis(oxamate) (opba), containing two *N*-amide and two *O*-carboxylate donor groups, can furnish stable dinuclear manganese complexes with different bridges and metal oxidation states [11]. In particular, there exists a manganese synthetic analogue of the reduced diferrous form of MMOH (MMOH_{red}, Scheme 1), namely the carboxylate-bridged dimanganese(III) complex (Ph₄P)₂[Mn₂(opba)₂(H₂O)₃] · 3H₂O · MeCN (**1**) [11b]. For this complex, the nitrogen ligation is ensured by the amide groups instead of the imidazoles actually present in the native diiron enzyme. As a matter of fact, studies on the structure and reactivity of iron amide complexes are a subject of major interest in iron coordination chemistry owing to their biological significance as enzyme models and their potentially useful properties as catalytic oxidants [12]. Amide nitrogen coordination has been invoked in the natural iron-containing glycopeptide bleomycin with antibiotic and antitumour properties, as well as in the active site of the mononuclear non-heme iron enzyme nitrile hydratase [13,14]. Because of the large electron σ -donor character of the deprotonated amide group, this kind of ligands allows the access to high-valent iron species which are implicated as key intermediates in several synthetic and enzymatic catalytic cycles involved in dioxygen activation chemistry [15,16]. Hence, we have extended the research on the coordination chemistry of this amide-containing opba ligand with the tervalent iron metal ion [17]. Here, we report on the synthesis, structure, magnetic and redox

properties of the new oxo-bridged diiron(III) complex (Et₄N)₄[Fe₂O(opba)₂] · 3H₂O (**2**), together with its reactivity properties toward hydrocarbon oxidation with hydrogen peroxide.



2. Experimental

2.1. Materials

All chemicals were of reagent grade quality, and they were purchased from commercial sources and used as received. The diethylester derivative of *N,N'*-*o*-phenylenebis(oxamic acid) (H₂Et₂opba) was prepared as reported in the literature [18].

2.2. Preparation

2.2.1. Method A

A solution of H₂Et₂opba (1.54 g, 5.0 mmol) in methanol (50 cm³) was charged with a 25% methanol solution of Et₄NOH (16.5 cm³, 25.0 mmol) under aerobic conditions. A methanol solution (25 cm³) of iron(III) perchlorate hydrate (1.75 g, 5.0 mmol) was then added dropwise with stirring at room temperature. The resulting deep-red blood solution was filtered on paper and the solvent was removed in a rotatory evaporator. The solid was recuperated with a minimum amount of absolute ethanol (25 cm³) and filtered under vacuum to eliminate the white precipitate of Et₄NClO₄. The filtered solution was concentrated again in a rotatory evaporator to eliminate the solvent and the resulting red solid was recrystallised from acetonitrile (50 cm³). Small red

prisms of **2** suitable for X-ray diffraction were deposited after a few hours of standing at room temperature. They were filtered on paper and air-dried. Yield ca. 60%.

2.2.2. Method B

A solution of $\text{H}_2\text{Et}_2\text{opba}$ (1.54 g, 5.0 mmol) in deoxygenated methanol (50 cm^3) was charged with a 25% methanol solution of Et_4NOH (13.2 cm^3 , 20.0 mmol) under argon. A deoxygenated methanol solution (25 cm^3) of iron(II) perchlorate hydrate (1.27 g, 5.0 mmol) was then added dropwise via a dropping funnel with stirring at room temperature. An orange precipitate [presumably an iron(II)–opba complex] formed at the end of the addition. Further addition of a 33% aqueous solution of H_2O_2 (0.5 cm^3 , 5.0 mmol) with a syringe caused immediate darkening of the initial red-orange solution with concomitant disappearance of the orange precipitate. The resulting deep-red blood solution was filtered on paper under air and the solvent was removed in a rotatory evaporator. The solid was recuperated with a minimum amount of absolute ethanol (25 cm^3) and filtered under vacuum to eliminate the white precipitate of Et_4NClO_4 . The filtered solution was concentrated again in a rotatory evaporator to eliminate the solvent and the resulting red solid was recrystallised from acetonitrile (50 cm^3). Large red prisms of **2** suitable for X-ray diffraction were deposited after a few hours of standing at room temperature. They were filtered on paper and air-dried. Yield ca. 40%. *Anal. calc.* for $\text{C}_{52}\text{H}_{94}\text{Fe}_2\text{N}_8\text{O}_{16}$: C, 52.04; H, 7.84; N, 9.34. *Found*: C, 51.89; H, 8.09; N, 9.71%. IR (KBr): 3415 s (OH), 1660 (sh) and 1624 vs (CO), 777 m (FeO) cm^{-1} . UV–Vis in MeCN $\lambda_{\text{max}}/\text{nm}$ ($\epsilon/\text{dm}^3\text{ mol}^{-1}\text{ cm}^{-1}$): 260 (34 000), 310 (23 000) and 410 (sh) (3000).

2.3. Crystal structure determination

Crystal data and structure refinement: $\text{C}_{26}\text{H}_{47}\text{FeN}_4\text{O}_8$, $M = 599.5$, orthorhombic, $a = 13.1963(19)\text{ \AA}$, $b = 23.474(3)\text{ \AA}$, $c = 9.922(2)\text{ \AA}$, $U = 3073.5(8)\text{ \AA}^3$, $T = 293\text{ K}$, space group $Pmmn$, $Z = 4$, $\mu(\text{Mo K}\alpha) = 0.541\text{ mm}^{-1}$, 2135 reflections measured, 1352 assumed as observed with $I \geq 2\sigma(I)$. Refinement on F^2 of 195 variables with anisotropic thermal parameters for all non-hydrogen atoms gave $R = 0.111$ and $wR = 0.291$ with $S = 1.235$ (observed data).

2.4. Physical techniques

Elemental analyses (C, H, N) were performed by the Microanalytical Service of the Universidad Autónoma de Madrid (Spain). IR spectra were recorded on a Perkin–Elmer 882 spectrophotometer as KBr pellets. UV–Vis solution spectra were recorded at room temperature on a Perkin–Elmer Lambda 2 spectrophotometer. GLC

analyses were performed with a Trace GC 2000 (Thermo Quest) using a $30\text{ m} \times 0.25\text{ mm}$ high-resolution gas chromatography column coated with methylpolysiloxane (5% phenyl). Variable-temperature (20–300 K) magnetic measurements under an applied magnetic field of 1.0 T were carried out on powdered samples of **2** with a SQUID magnetometer. Diamagnetic corrections to the susceptibility data were calculated from Pascal's constants, and they were also corrected for temperature-independent paramagnetism and the presence of paramagnetic impurities.

Cyclic voltammetry was performed using an EGG M273 PAR scanning potentiostat operating at a scan rate of $10\text{--}1000\text{ mV s}^{-1}$. The electrochemical studies were carried out in acetonitrile using 0.1 mol dm^{-3} Et_4NClO_4 as supporting electrolyte and 1.0 mmol dm^{-3} of **2**. The working electrode was a glassy carbon disk (0.32 cm^2), which was polished with $1.0\text{ }\mu\text{m}$ polishing powder, sonicated, washed with absolute ethanol and acetone and air-dried. The reference electrode was AgClO_4/Ag separated from the test solution by a salt bridge containing the solvent/supporting electrolyte, with platinum as auxiliary electrode. All experiments were performed in standard electrochemical cells at $25\text{ }^\circ\text{C}$ under argon. The potential range investigated was between -1.8 and 2.0 V . The formal potentials were measured at a scan rate of 100 mV s^{-1} and were referred to the SCE, which was consistently measured as -0.26 V versus the AgClO_4/Ag electrode.

2.5. Reactivity studies

2.5.1. General procedure for the oxidation of hydrocarbon substrates

Reactions were carried out at room temperature by adding a 33% aqueous solution of H_2O_2 (0.1 cm^3 , 1.0 mmol) to a stirred mixture of the metal catalyst ($2.5 \times 10^{-3}\text{ mmol}$) and the substrate (0.10 mmol) in acetonitrile (2.5 cm^3) under O_2 atmosphere for a period of 24 h. Excess triphenylphosphine (2.0 mmol) was added at the end of the reaction to ensure reduction of any remaining H_2O_2 before GLC analysis. Products were identified by comparison of their retention times with those of authentic samples.

2.5.2. Typical procedure for the determination of the kinetic isotope effect

Solution mixtures containing equal amounts of cyclohexane and cyclohexane- d_{12} were used under the same procedure described above. The kinetic isotope effect ($\text{KIE} = k_{\text{H}}/k_{\text{D}}$) was determined by GLC analysis of the oxidised products and corresponded to the average of three independent experiments.

3. Results and discussion

3.1. Synthesis

The oxo-bridged dinuclear iron(III) oxamate complex **2** has been prepared by direct reaction of Fe^{3+} and the proligand $\text{H}_2\text{Et}_2\text{opba}$ in basic methanol solution with excess Et_4NOH (base/ligand ratio of 5:1) and isolated as the tetraethylammonium salt (method A). Alternatively, complex **2** can be obtained by oxidation with hydrogen peroxide of the corresponding iron(II) complex, prepared in situ from reaction between Fe^{2+} and the proligand $\text{H}_2\text{Et}_2\text{opba}$ in basic methanol solution with stoichiometric Et_4NOH (base/ligand ratio of 4:1) under anaerobic conditions (method B). The chemical identity of **2** obtained by either of the two methods has been confirmed by elemental analyses, IR and UV–Vis spectroscopies.

3.2. Structure

The structure of **2** consists of dinuclear iron complex anions with a C_{2v} symmetry, $[\text{Fe}_2(\mu\text{-O})(\text{opba})_2]^{4-}$ (Fig. 1), partially disordered tetraethylammonium cations and ordered crystallisation water molecules which connect the dinuclear units through intermolecular hy-

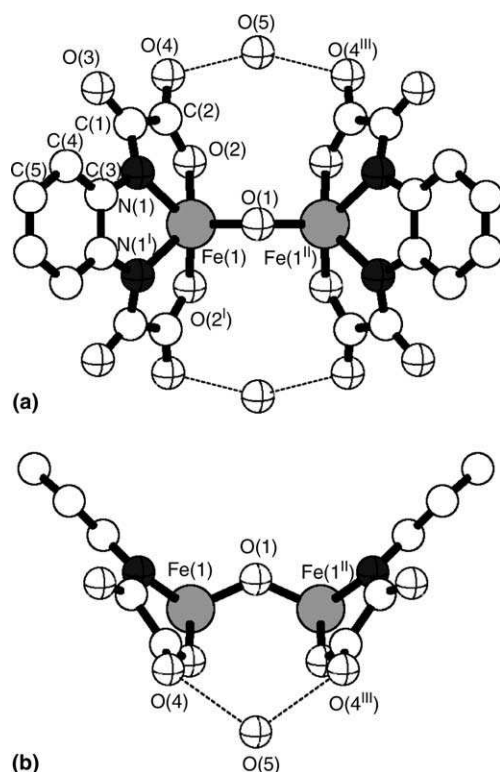


Fig. 1. Perspective views of the anionic dinuclear unit of **2** with the atom numbering scheme. Hydrogen bonds are represented by dashed lines (symmetry codes: (I) $-x + 1/2, y, z$; (II) $-x + 1/2, -y + 1/2, z$; (III) $x, -y + 1/2, z$).

drogen bonds leading to extended linear arrays along the a -axis (Fig. 2). Selected bond distances and angles are listed in Table 1.

The two crystallographically equivalent iron atoms exhibit a distorted five-coordinate square-pyramidal geometry, FeN_2O_3 : two amide nitrogen and two carboxylate oxygen atoms of the mononucleating tetradentate opba ligand define the equatorial plane, and one oxygen atom from the bridging oxo group occupies the axial position. The ligand adopts a unique ruffled conformation with two non-coplanar (folded) oxamato groups [dihedral angle of $39.3(7)^\circ$]. The Fe(1) atom is substantially protruded from the N_2O_2 basal plane

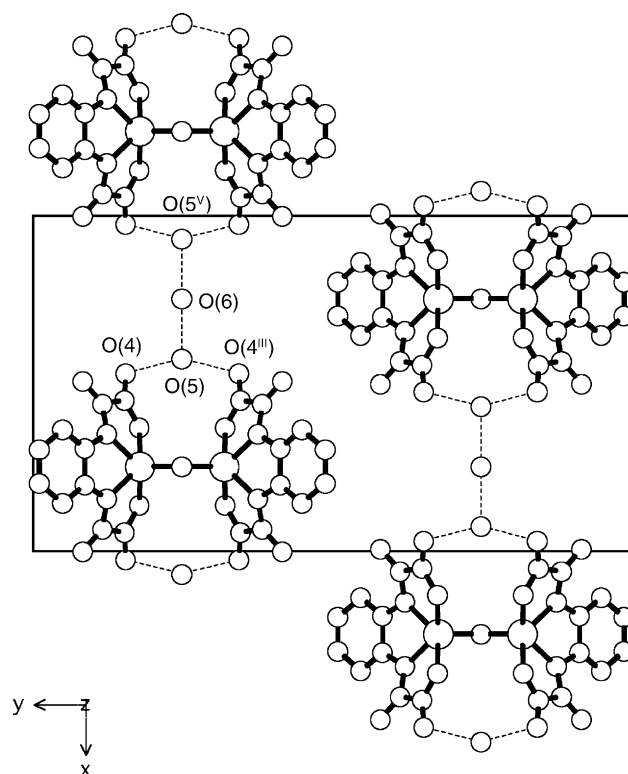


Fig. 2. Crystal packing of **2** down the c -axis. Hydrogen bonds are represented by dashed lines (symmetry codes: (III) $-x, -y + 1/2, z$; (V) $-x - 1/2, y, z$).

Table 1
Selected bond distances (\AA) and angles ($^\circ$) for **2**^{a,b}

Fe(1)–N(1)	2.053(7)	Fe(1)–O(1)	1.808(5)
Fe(1)–O(2)	2.015(7)	O(4)–O(5)	2.764(13)
O(5)–O(6)	2.765(15)		
N(1)–Fe(1)–O(1)	113.5(3)	N(1)–Fe(1)–O(2)	80.0(3)
N(1)–Fe(1)–N(1 ^I)	76.3(4)	N(1)–Fe(1)–O(2 ^I)	139.4(3)
O(1)–Fe(1)–O(2)	106.0(3)	O(2)–Fe(1)–O(2 ^I)	98.0(5)
Fe(1)–O(1)–Fe(1 ^{II})	131.9(7)	O(4)–O(5)–O(4 ^{III})	106.1(6)
O(4)–O(5)–O(6)	118.2(4)	O(5)–O(6)–O(5 ^V)	117.9(8)

^a Estimated standard deviations are given in parentheses.

^b Symmetry codes: (I) $-x + 1/2, y, z$; (II) $-x + 1/2, -y + 1/2, z$; (III) $x, -y + 1/2, z$; (V) $-x - 1/2, y, z$.

toward the apical site [mean plane deviation of 0.675(5) Å]. The Fe(1)–N(1) and Fe(1)–O(2) bond lengths of 2.053(7) and 2.015(7) Å, respectively, are close to those of the related mononuclear high-spin iron(III)–opba complex (average values of 2.05 and 2.01 Å, respectively) [17a]. In fact, the metal–nitrogen bond distance in **2** is characteristic of high-spin iron(III) amide complexes (average value of 2.05 Å), being significantly longer than those of analogous low- or intermediate-spin iron(III) amide complexes (1.88–1.97 Å) [12a]. Otherwise, the Fe(1)–O(1) (*R*) bond length of 1.808(5) Å is among the longest ones yet reported for a (μ -oxo)diiron(III) complex (*R* = 1.73–1.82 Å), but it is shorter than those of any (μ -hydroxo)diiron(III) complex (*R* = 1.92–2.06 Å) [1b]. Within the Fe₂O core, the bent Fe(1)–O(1)–Fe(1^{II}) (α) bond angle of 131.8(7)° results in a remarkably short Fe(1)–Fe(1^{II}) (*d*) intramolecular separation of 3.303(3) Å. To our knowledge, this is the shortest intermetallic distance among the previously reported μ -oxo singly bridged diiron(III) complexes (*d* = 3.35–3.55 Å) [1b]. For comparison, it is intermediate between those observed in triply bridged Fe₂^{III}(μ -O)(μ -RCO₂)₂ (*d* = 3.08–3.24 Å) and Fe₂^{III}(μ -OH)(μ -RCO₂)₂ species (*d* = 3.44 Å) [1b], which are closer structural models of the oxidised diferric form of MMOH (MMOH_{ox}, Scheme 1). In fact, although the structures of **2** and the μ -hydroxo triply bridged diiron(III) active site of MMOH_{ox} are basically different, some similarities are apparent in their first coordination spheres insofar as each contains two iron atoms ligated by four carboxylates, one of them being present as an additional bridge in MMOH_{ox} [3].

Within the dinuclear unit, two uncoordinated water molecules are hydrogen-bonded to the free carbonyl oxygen atoms from each of the two symmetry-related *syn* iron–opba moieties [O(4)···O(5) separation of 2.764(13) Å]. These second coordination sphere interactions lead to a μ -oxo triply bridged diiron(III) core, Fe₂^{III}(μ -O)(μ -RCO₂)₂·H₂O·O₂CR)₂, consisting of two fused 10-membered, hydrogen-bonded metallacyclic rings (Fig. 1a). More likely, the presence of these intramolecular hydrogen bridges between the coordinated carboxylate groups and the water molecules clamping the two iron atoms is responsible for the bent core structure (Fig. 1b), as previously shown in doubly bridged Fe₂^{III}(μ -O)(μ -OH···OH₂) species [19]. Notably, the structural role of water in **2** reminds the importance of related hydrogen-bonding interactions in the second coordination sphere of the active site of MMOH (Scheme 1) [3]. Overall, this situation delineates a butterfly-shaped bifunctional complex (Fig. 1b) possessing a highly hydrophilic, coordinatively unsaturated dimetallic “body” site able to interact with small polar molecules (not only water but also dioxygen or hydrogen peroxide), and a largely hydrophobic “wing-tip” site available to the access of exogenous hydrocarbon substrates.

3.3. Magnetic properties

The magnetic behaviour of **2** in the form of both χ_M and $\chi_M T$ versus *T* plots (χ_M being the molar magnetic susceptibility per dinuclear unit and *T* the temperature) is typical of an antiferromagnetically coupled high-spin Fe₂^{III} pair (Fig. 3). At room temperature, the product $\chi_M T$ is equal to 0.92 cm³ mol^{−1} K, a value which is much smaller than that expected for two magnetically isolated high-spin Fe^{III} ions. Upon cooling, both χ_M and $\chi_M T$ continuously decrease and vanish at 50 K, which unambiguously indicates a diamagnetic singlet (*S* = 0) spin ground state.

The least-squares fitting of the experimental magnetic susceptibility data by setting *g* = 2.0 gives *J* = −190 cm^{−1} (*H* = −*J**S*₁ · *S*₂; *S*₁ = *S*₂ = 5/2) (solid lines in Fig. 3). The absolute value of the exchange coupling parameter for **2** is among the smallest ones yet reported for strongly coupled μ -oxo monobridged diiron(III) complex (−*J* values in the range 160–390 cm^{−1}) [1b]. The moderately strong antiferromagnetic coupling in **2** presumably reflects the rather long Fe–O distance and/or the fairly bent Fe–O–Fe angle [20,21], which are associated with the presence of two additional (RCO)₂O₃H₂^{2−} bridges. For instance, the aforementioned μ -oxo dibridged diiron(III) complexes, with a H₃O₂[−] bridge and comparable structural dimensions for the bridging core (α = 136–139°, *R* = 1.81–1.82 Å), possess similar exchange coupling parameter values (−*J* = 184–196 cm^{−1}) [19]. This attenuation of the antiferromagnetic exchange interaction is common to a large class of bent μ -hydroxo and μ -oxo diiron(III) model complexes with biologically relevant oxygen supporting bridges, either aqua-derived and/or carboxylate (−*J* values in the range 11–280 cm^{−1}) (Scheme 2)

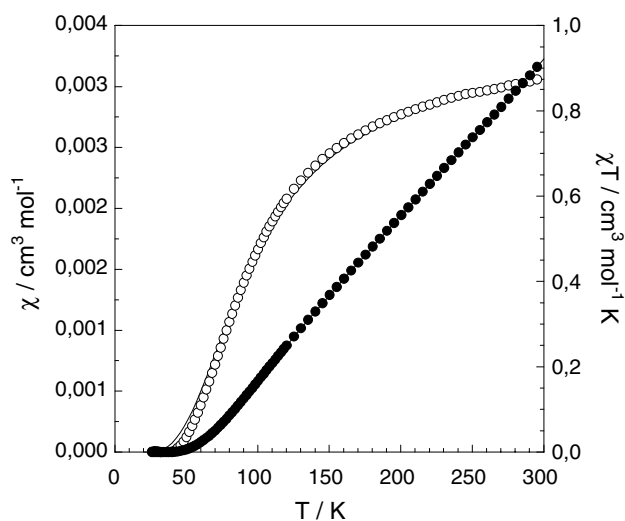
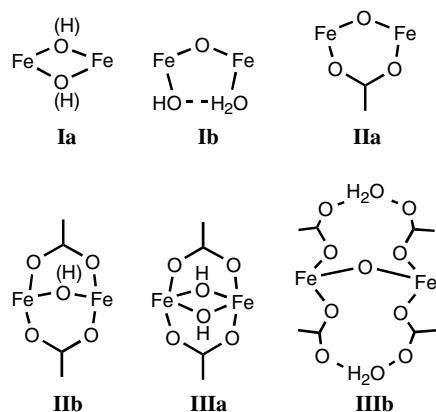


Fig. 3. Temperature dependence of χ_M (○) and $\chi_M T$ (●) of **2**. Solid lines correspond to the best fit.

(Table S1, Supplementary material). Magnetostructural data indicate that the magnitude of the antiferromagnetic coupling ($-J$) is mainly controlled by the Fe–O bond distance (R) and largely insensitive to the Fe–O–Fe bond angle (α) (Fig. 4). Gorun and Lippard reported a semiquantitative empirical correlation as $-J = 1.753 \times 10^{12} \exp(-12.663R)$ (solid line in Fig. 4) [21a], from which a $-J$ value of 200 cm^{-1} is estimated for **2**, in fairly good agreement with that determined experimentally.



Scheme 2. Structural representation of different bridging cores of μ -hydroxo- and μ -oxo-diiron(III) complexes with biologically relevant oxygen supporting bridges: aqua series (I), carboxylate series (II) and aqua/carboxylate series (III).

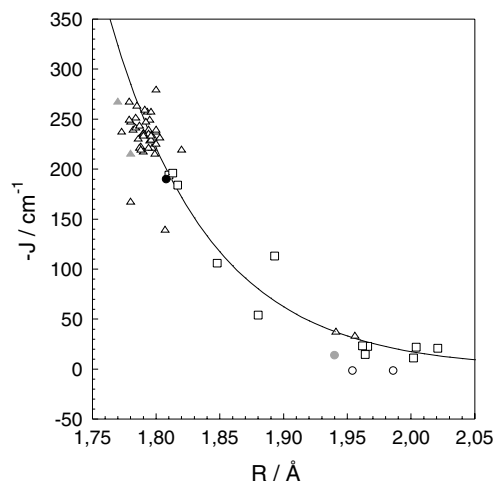


Fig. 4. Decay law for the magnetic coupling with metal–oxygen bond distance for μ -hydroxo- and μ -oxo-diiron(III) complexes with biologically relevant oxygen supporting bridges and for related active sites of dinuclear non-heme iron enzymes: aqua series (\square), carboxylate series (Δ) and aqua/carboxylate series (\circ) (data from Table S1, Supplementary material). Full coloured symbols correspond to diiron enzymes (gray) and compound **2** (black). The solid line corresponds to the Gorun–Lippard relation.

3.4. Redox properties

The cyclic voltammogram of **2** in acetonitrile at 25°C shows a completely irreversible oxidation wave at a moderately low formal potential of 0.63 V versus SCE; no reduction is observed in the potential range studied (up to -1.8 V versus SCE). This electrochemical behaviour indicates that high oxidation states are available for the iron–opba system, as reported earlier for other amido-containing ligands [15,16]. However, the putative (μ -oxo)diiron(III,IV) species obtained by one-electron oxidation of **2** is unstable on the voltammetric time-scale. At this regard, it is interesting to note that Lippard et al have identified a related metastable mixed-valent diiron(III,IV) species from the reaction between a diiron(II) complex with sterically hindered carboxylate ligands and O_2 [22]. More interestingly, Que et al have isolated stable bis(μ -oxo)diiron(III,IV) complexes with tetradentate tripodal aminopyridine ligands from the reaction of the corresponding (μ -oxo)diiron(III) precursors and H_2O_2 [23]. All these oxo-bridged high-valent diiron compounds obtained by electrochemical or chemical oxidation would be suitable models for the proposed active intermediate of MMOH (compound Q) [1e].

3.5. Reactivity properties

The catalytic activity of **2** toward the oxidation of aliphatic hydrocarbon substrates has been examined in acetonitrile and at room temperature using hydrogen peroxide as oxidant in the presence of dioxygen. The results for some representative alkanes are summarised in Table 2.

Complex **2** catalyses the oxidation of cyclohexane to the corresponding alcohol and ketone products, cyclohexanol and cyclohexanone, respectively, with a low but nonnegligible total yield of 5.2% after 24 h (Table 2, entry 1). The kinetic isotope effect ($\text{KIE} = k_{\text{H}}/k_{\text{D}}$) for the oxidation of cyclohexane has been determined to be

Table 2
Results for the oxidation of alkanes catalysed by **2**^{a,b}

Entry	Substrate	Product	Yield (%) ^c
1	Cyclohexane	Cyclohexanol	2.5
		Cyclohexanone	2.7
2	Cyclohexane ^d	Cyclohexanol	2.3
		Cyclohexanone	1.0
3	Cyclohexanol	Cyclohexanone	3.2
4	Adamantane	1-Adamantanol	2.8
		2-Adamantanol	1.6
		2-Adamantanone	1.2

^a Reactions conditions: see section 2.

^b In the absence of catalyst no oxidation was observed.

^c Yields refer to GLC determination based on the starting substrate.

^d Under Ar.

2.4 from the competitive reaction of cyclohexane and cyclohexane- d_{12} . This value indicates that C–H bond cleavage is the rate-determining step of the catalytic cycle, and moreover, it suggests the participation of a fairly selective species, other than the hydroxyl radical ($KIE = 1\text{--}2$) [24], as active oxidising agent. In addition, the formation of roughly equal amounts of cyclohexanol and cyclohexanone is indicative of a Russell-type bimolecular self-reaction of cyclohexylperoxyl radicals that would be formed as putative intermediates from the combination of cyclohexyl radicals and dioxygen under aerobic conditions. In fact, the alcohol:ketone ratio (A/K) raises from 0.9 to 2.3 under anaerobic conditions (Table 2, entry 2). This suggests that alcohols are primarily formed in the absence of dioxygen, and they are further converted into ketones during the oxidation reaction, as confirmed by control experiments (Table 2, entry 3). On the other hand, the tertiary to secondary C–H bond relative reactivities (*tert/sec* ratio; on a per bond basis) for the oxidation of adamantane is 3.0 (Table 2, entry 4), which is a somewhat higher value to that reported when the active oxidant is the hydroxyl radical (*tert/sec* = 2) [24]. This regioselectivity value for adamantane oxidation compares well with those reported for many other non-heme oxo-bridged diiron catalysts which oxidise alkanes with hydrogen peroxide (*tert/sec* = 2.2–4.5) [25], but also for MMOH (*tert/sec* = 3.0) [26].

In summary, a novel dinuclear non-heme oxoiron amide complex bearing a carboxylate rich environment reminiscent of that found in the active site of methane monooxygenase has been developed for the hydrogen peroxide-dependent hydroxylation of alkanes. On the whole, the present work shows that this diiron oxamate complex exhibits modest selectivities but limited catalytic activities, probably due to catalyst decomposition during the course of the oxidation reaction as demonstrated by Collins et al. [15e–15h] in a comprehensive work on H_2O_2 activation by related mononuclear non-heme iron amide complexes. We are currently searching for a new generation of iron complexes with highly donor oxamide ligands, especially resistant to oxidative degradation, and that might lead to improved homogeneous oxidation catalysts obtained through ligand design.

4. Supplementary material

Crystallographic data (excluding structure factors) for compound 2 have been deposited with the Cambridge Crystallographic Data Centre, CCDC No. 189437. Copies of the data may be obtained free of charge on application to The Director, CCDC, 12 Union Road, Cambridge CB2 1EZ, UK (fax: +44 1223 336 033; e-mail: deposit@ccdc.cam.ac.uk or [\[www.ccdc.cam.ac.uk\]\(http://www.ccdc.cam.ac.uk\)\). Selected magnetocrystallographic data for \$\mu\$ -hydroxo- and \$\mu\$ -oxo-diiron\(III\) complexes with biologically relevant oxygen supporting bridges and related active sites of dinuclear non-heme iron enzymes \(Table S1, Supplementary material\).](http://</p></div><div data-bbox=)

Acknowledgements

This work was supported by the Ministerio de Ciencia y Tecnología (MCYT) (Spain) through the Plan Nacional de Investigación Científica, Desarrollo e Innovación Tecnológica (I + D + I) (BQU2001–2928) and the Ramón y Cajal programme. Further support from the Oficina de Ciencia i Tecnologia de la Generalitat Valenciana (Spain) through the Plan Valenciano de Investigación Científica, Desarrollo Tecnológico e Innovación (PVIDI) (CTIDIA2002–131) is also acknowledged. E.P. thanks the Ministerio de Educación, Cultura y Deporte (Spain) for a FPU grant. We are specially thankful to Dr. E. Anxolabéhère-Mallart for the assistance with the electrochemical measurements and Dr. J. Cano for very stimulating talks and unselfish help during the realisation of this work.

References

- [1] (a) S.J. Lippard, *Angew. Chem. Int. Ed. Engl.* 27 (1988) 344; (b) D.M. Kurtz Jr., *Chem. Rev.* 90 (1990) 585; (c) L. Que Jr., Y. Dong, *Acc. Chem. Res.* 29 (1996) 190; (d) M. Fontecave, S. Ménage, C. Duboc-Toia, *Coord. Chem. Rev.* 178–180 (1998) 1555; (e) L. Que Jr., W.B. Tolman, *Angew. Chem. Int. Ed.* 41 (2002) 1115.
- [2] (a) B.J. Wallar, J.D. Lipscomb, *Chem. Rev.* 96 (1996) 2625; (b) M. Merckx, D.A. Kopp, M.H. Sazinsky, J.L. Blazyk, J. Müller, S.J. Lippard, *Angew. Chem. Int. Ed.* 40 (2001) 2783.
- [3] D.A. Whittington, S.J. Lippard, *J. Am. Chem. Soc.* 123 (2001) 827.
- [4] B.G. Fox, W.A. Froland, J.E. Dege, J.D. Lipscomb, *J. Biol. Chem.* 264 (1989) 10023.
- [5] K.K. Andersson, W.A. Froland, S.K. Lee, J.D. Lipscomb, *New J. Chem.* 15 (1991) 411.
- [6] Z. Hu, S.M. Gorun, in: B. Meunier (Ed.), *Biomimetic Oxidations Catalyzed by Transition Metal Complexes*, Imperial College Press, London, 2000, pp. 269–307, Chapter 6 and references therein.
- [7] (a) G.J.A. Ligtenbarg, P. Oosting, G. Roelfes, R.M. La Crois, M. Lutz, A.L. Spek, R. Hage, B.L. Feringa, *Chem. Commun.* (2001) 385; (b) M.C. White, A.G. Doyle, *J. Am. Chem. Soc.* 123 (2001) 7194; (c) Y. Mekmouche, H. Hummel, R.Y.N. Ho, L. Que Jr., V. Schünemann, F. Thomas, A.X. Trautwein, C. Lebrun, K. Gorgy, J.C. Leprete, M.N. Collomb, A. Deronzier, M. Fontecave, S. Ménage, *Chem. Eur. J.* 8 (2002) 1196; (d) N.R.P.Y. Moll, F. Banse, K. Miki, M. Nierlich, J.J. Girerd, *Eur. J. Inorg. Chem.* (2002) 1941; (e) X. Wang, S. Wang, L. Li, E.B. Sundberg, G.P. Gacho, *Inorg. Chem.* 42 (2003) 7799.
- [8] B. Graham, B. Moubaraki, K.S. Murray, L. Spiccia, J.D. Cashion, D.C.R. Hockless, *J. Chem. Soc. Dalton Trans.* (1997) 887.

- [9] (a) T.J. Mizoguchi, R.M. Davydov, S.J. Lippard, *Inorg. Chem.* 38 (1999) 4098;
(b) D. Lee, S.J. Lippard, *Inorg. Chem.* 41 (2002) 827.
- [10] W.B. Tolman, L. Que Jr., *J. Chem. Soc. Dalton Trans.* (2002) 653.
- [11] (a) R. Ruiz, A. Aukauloo, Y. Journaux, I. Fernández, J.R. Pedro, A.L. Roselló, B. Cervera, I. Castro, M.C. Muñoz, *Chem. Commun.* (1998) 989;
(b) G. Blay, I. Fernández, T. Giménez, J.R. Pedro, R. Ruiz, E. Pardo, F. Lloret, M.C. Muñoz, *Chem. Commun.* (2001) 2102.
- [12] (a) D.S. Marlin, P.K. Mascharak, *Chem. Soc. Rev.* 29 (2000) 69, and references therein;
(b) J.C. Noveron, M.M. Olmstead, P.K. Mascharak, *J. Am. Chem. Soc.* 123 (2001) 3247;
(c) J.M. Rowland, M.M. Olmstead, P.K. Mascharak, *Inorg. Chem.* 40 (2001) 2810;
(d) J.M. Rowland, M.M. Olmstead, P.K. Mascharak, *Inorg. Chem.* 41 (2002) 2754;
(e) A.K. Patra, R. Afshar, M.M. Olmstead, P.K. Mascharak, *Angew. Chem. Int. Ed.* 41 (2002) 2512.
- [13] R.M. Burger, *Struct. Bonding* 97 (2000) 287.
- [14] (a) M. Tsujimura, N. Sohmae, M. Odaka, M. Chijimatsu, K. Takio, M. Yohda, M. Hoshino, S. Nagashima, I. Endo, *J. Biol. Chem.* 272 (1997) 29454;
(b) W. Huang, J. Jia, J. Cummings, M. Nelson, G. Schneider, Y. Lindqvist, *Structure* 5 (1997) 691.
- [15] (a) T.J. Collins, K.L. Kostka, E. Münck, E.S. Uffelman, *J. Am. Chem. Soc.* 112 (1990) 5637;
(b) T.J. Collins, B.J. Fox, Z.G. Hu, K.L. Kostka, E. Münck, C.E.F. Rickard, L.J. Wright, *J. Am. Chem. Soc.* 114 (1992) 8724;
(c) K.L. Kostka, B.J. Fox, M.P. Hendrich, T.J. Collins, C.E.F. Rickard, L.J. Wright, E. Münck, *J. Am. Chem. Soc.* 115 (1993) 6746;
(d) M.J. Bartos, C. Kidwell, K.E. Kauffmann, S.W. Gordon-Wylie, T.J. Collins, G.C. Clark, E. Münck, S.T. Weintraub, *Angew. Chem. Int. Ed. Engl.* 34 (1995) 1216;
(e) C.P. Horwitz, D.R. Fooksman, L.D. Vuocolo, S.W. Gordon-Wylie, N.J. Cox, T.J. Collins, *J. Am. Chem. Soc.* 120 (1998) 4867;
(f) M.J. Bartos, S.W. Gordon-Wylie, B.G. Fox, L.J. Wright, S.T. Weintraub, K.E. Kauffmann, E. Münck, K.L. Kostka, E.S. Uffelman, C.E.F. Rickard, K.R. Noon, T.J. Collins, *Coord. Chem. Rev.* (1998) 361;
(g) S.S. Gupta, M. Stadler, C.A. Noser, A. Ghosh, B. Steinhoff, D. Lenoir, C.P. Horwitz, K.W. Schramm, T.J. Collins, *Science* 296 (2002) 326;
(h) A. Ghosh, A.D. Ryabov, S.M. Mayer, D.C. Horner, D.E. Prasuhn Jr., S.S. Gupta, L. Vuocolo, C. Culver, M.P. Hendrich, C.E.F. Rickard, R.E. Norman, C.P. Horwitz, T.J. Collins, *J. Am. Chem. Soc.* 125 (2003) 12378.
- [16] (a) C.E. MacBeth, A.P. Golombek, V.G. Young Jr., C. Yang, K. Kucera, M.P. Hendrich, A.S. Borovik, *Science* 289 (2000) 938;
(b) C.E. MacBeth, B.S. Hammes, V.G. Young Jr., A.S. Borovik, *Inorg. Chem.* 40 (2001) 4733;
(c) R. Gupta, A.S. Borovik, *J. Am. Chem. Soc.* 125 (2003) 13234;
(d) M.K. Zart, T.N. Sorrell, D. Powell, A.S. Borovik, *Dalton Trans.* (2003) 1986.
- [17] (a) R. Ruiz, M. Traianidis, A. Aukauloo, Y. Journaux, I. Fernández, J.R. Pedro, B. Cervera, I. Castro, M.C. Muñoz, *Chem. Commun.* (1997) 2283;
(b) M.C. Muñoz, R. Ruiz, M. Traianidis, A. Aukauloo, J. Cano, Y. Journaux, I. Fernández, J.R. Pedro, *Angew. Chem. Int. Ed.* 37 (1998) 1833.
- [18] (a) R. Ruiz, C. Surville-Barland, A. Aukauloo, E. Anxolabèhere-Mallart, Y. Journaux, J. Cano, M.C. Muñoz, *J. Chem. Soc. Dalton Trans.* (1997) 745;
(b) B. Cervera, J.L. Sanz, M.J. Ibáñez, G. Vila, F. Lloret, M. Julve, R. Ruiz, X. Ottenwaelde, A. Aukauloo, S. Poussereau, Y. Journaux, M.C. Muñoz, *J. Chem. Soc. Dalton Trans.* (1998) 781.
- [19] (a) R. Hazell, K.B. Jensen, C.J. McKenzie, H. Toftlund, *Inorg. Chem.* 33 (1994) 3127;
(b) Y. Dong, H. Fujii, M.P. Hendrich, R.A. Leising, G. Pan, C.R. Randall, E.C. Wilkinson, Y. Zang, L. Que Jr., B.G. Fox, K. Kauffman, E. Münck, *J. Am. Chem. Soc.* (1995) 2778;
(c) S. Poussereau, G. Blondin, M. Cesario, J. Guilhem, G. Chottard, F. Gonnet, J.J. Girerd, *Inorg. Chem.* 37 (1998) 1057.
- [20] (a) R.N. Mukherjee, T.D.P. Stack, R.H. Holm, *J. Am. Chem. Soc.* 110 (1988) 1850;
(b) R.E. Norman, R.C. Holz, S. Ménage, C.J. O'Connor, J.H. Zhang, L. Que Jr., *Inorg. Chem.* 29 (1990) 4629;
(c) R. Hotzelmann, K. Wieghardt, U. Flörke, H.J. Haupt, D.C. Weatherburn, J. Bonvoisin, G. Blondin, J.J. Girerd, *J. Am. Chem. Soc.* 114 (1992) 1681.
- [21] (a) S.M. Gorun, S.J. Lippard, *Inorg. Chem.* 30 (1991) 1625;
(b) J.R. Hart, A.K. Rappé, S.M. Gorun, T.H. Upton, *Inorg. Chem.* 31 (1992) 5254.
- [22] (a) D. Lee, J. Du Bois, D. Petasis, M.P. Hendrich, C. Krebs, B.H. Huynh, S.J. Lippard, *J. Am. Chem. Soc.* 121 (1999) 9893;
(b) D. Lee, B. Pierce, C. Krebs, M.P. Hendrich, B.H. Huynh, S.J. Lippard, *J. Am. Chem. Soc.* 124 (2002) 3993.
- [23] (a) Y. Dong, H. Fujii, M.P. Hendrich, R.A. Leising, G. Pan, C.R. Randall, E.C. Wilkinson, Y. Zang, L. Que Jr., B.C. Fox, K. Kauffmann, E. Münck, *J. Am. Chem. Soc.* 117 (1995) 2778;
(b) H.F. Hsu, Y. Dong, L.J. Shu, L. Que Jr., *J. Am. Chem. Soc.* 121 (1999) 5230.
- [24] (a) A.F. Trotman-Dickenson, *Adv. Free Radical Chem.* 1 (1965) 32;
(b) S. Miyajima, O. Simamura, *Bull. Chem. Soc. Jpn.* 48 (1975) 526;
(c) G.V. Buxton, C.L. Greenstock, W.P. Helman, A.B. Ross, *J. Phys. Chem. Ref. Data* 17 (1988) 513.
- [25] (a) R.H. Fish, M.S. Konings, K.J. Oberhausen, R.H. Fong, W.M. Yu, G. Christou, J.B. Vincent, D.K. Coggin, R.M. Buchanan, *Inorg. Chem.* 30 (1991) 3002;
(b) A.E. Tapper, J.R. Long, R.J. Staples, P. Stavropoulos, *Angew. Chem. Int. Ed.* 39 (2000) 2343;
(c) S. Kiani, A. Tapper, R.J. Staples, P. Stavropoulos, *J. Am. Chem. Soc.* 122 (2000) 7503;
(d) E. Balogh-Hergovich, G. Speier, M. Réglér, M. Giorgi, E. Kuzmann, A. Vértes, *Eur. J. Inorg. Chem.* (2003) 1735.
- [26] M. Kodera, K. Kano, T. Funabiki, in: T. Funabiki (Ed.), *Oxygenases and Model Systems*, vol. 19, Academic Publishers, Dordrecht, 1997, pp. 283–343.